In-Cylinder Species Imaging in Internal Combustion Engines using Absorption Spectroscopy

A thesis submitted to The University of Manchester for the degree of Doctor of Philosophy in the Faculty of Engineering and Physical Sciences

2013

Solon Karagiannopoulos

School of Electrical and Electronic Engineering

TABLE OF CONTENTS

Abbreviations

2f	Second Harmonic
AFR	Air-Fuel-Ratio
AR	Anti-Reflection
ATDC	After Top Dead Centre
BNC	Bayonet Neill–Concelman
BTDC	Before Top Dead Centre
°CA	Crank Angle degrees
CAI	Controlled Auto-Ignition
CARS	Coherent anti-Stokes Raman Spectroscopy
CCD	Charge-Coupled Device
CPLD	Complex Programmable Logic Device
CST	Chemical Species Tomography
DAS	Direct Absorption Apectroscopy
DDS	Direct Digital Synthesis
DFB	Distributed Feedback
DFWM	Degenerate Four-Wave Mixing
DWR	Dual-Wavelength Ratio
EDFA	Erbium-Doped Fibre Amplifiers
EGR	Exhaust Gas Recirculation
FDM	Frequency Division Multiplexing
FFT	Fast Fourier Transform
FSR	Free Spectral Range
FWHM	Full Width at Half Maximum
GDI	Gasoline-Direct Injection
GRIN	Gradient Index

HC	Hydrocarbon
HCCI	Homogeneous Charge Compression Ignition
HITRAN	High Resolution Transmission
HWHM	Half Width Half Maximum
IC	Internal Combustion
IVC	Inlet Valve Closing
IVO	Inlet Valve Opening
LII	Laser Induced Incandescence
MAP	Manifold Pressure
MM	Multimode
Near-IR	Near-Infrared
OSA	Optical Spectrum Analyser
PCB	Printed Circuit Board
PFI	Port Fuel Injection
PIV	Particle Imaging Velocimetry
PCI	Path-Concentration Integral
PLIF	Planar Laser Induced Florescence
PPM	Parts per Million by volume
QCL	Quantum Cascade Lasers
RAM	Residual Amplitude Modulation
RH	Relative Humidity
SM	Single Mode
SNR	Signal to Noise Ratio
SOA	Semiconductor Optical Amplifiers
TDLAS	Tunable Diode Laser Absorption Spectroscopy
TDM	Time-Division-Multiplexing
TTL	Transistor–transistor logic

UV	Ultraviolet
VHDL	VHSIC Hardware Description Language
VOA	Variable Optical Attenuator
WD	Wavelet Denoising
WDM	Wavelength Division Multiplexing
WMS	Wavelength Modulation Spectroscopy

List of Figures

Abstract

Combustion diagnostics based on Diode Lasers have been in focus of research in recent years, due to the advances in optical technologies. Tunable Diode Laser Absorption Spectroscopy (TDLAS) has been employed for in-cylinder, non-intrusive, crank-angle resolved measurements in Internal Combustion (IC) engines. This thesis addresses a novel opto-electronic, multi-wavelength scheme for line-of-sight gas absorption measurements and tomographic imaging in IC engines. High temporal resolution measurements of H_2O vapour using direct absorption spectroscopy (DAS), with external intensity modulation for phase sensitive detection, is implemented with Semiconductor Optical Amplifiers (SOAs). Using spectroscopic databases, two Near-IR overtone water transitions have been appropriately selected for ratiometric temperature compensation to enable concentration measurements, and an additional wavelength to account for non-absorbing attenuation. A scanned-wavelength approach was used for laboratory evaluation of the new technique at 250 KS/s, and comparison with simulated absorption lines showed excellent accuracy and precision. Fixed-wavelength, Time-Division-Multiplexing (TDM) operation with SOAs as optical switching elements has also been demonstrated in the laboratory. A preliminary demonstration of the scheme on an optical engine has been presented with three projections continuously monitored at 150 KS/s during motored and fired engine operation. Valuable data for the system characterisation and future modifications and improvement have been obtained. Finally, tomographic imaging results of liquid and vapour phase fuel distribution in a motored IC engine are also presented.

Declaration

No portion of the work referred to in the thesis has been submitted in support of an application for another degree or qualification of this or any other university or other institute of learning.

Copyright Statement

Acknowledgements

First and foremost, I would like to thank my supervisor Prof Hugh McCann for giving me this opportunity and for his incredible insight, support, guidance and commitment throughout this project. His genuine character, positive attitude and creative ideas were an excellent inspiration and kept me motivated until the end of this project. Special thanks to my advisor Prof Krikor Ozanyan for his encouragement and valuable advices.

I would like to thank all my colleagues in the SISP group in the University of Manchester for their support and for making life in the university more enjoyable. Namely, I would like to thank Dr Paul Wright for assisting me with his outstanding knowledge in electronics, Dr Edward Cheadle for introducing me into the world of spectroscopy, and Dr Natasha Terzija for her help with signal processing and image reconstruction. Special thanks to my colleague Alex Tsekenis for helping me in many ways throughout the project especially with his intuition in electronics.

For their help in terms of technical support and equipment I would also like to acknowledge Dr Phillip Martin, his research staff and TDL Sensors, as well as the staff of the mechanical workshop in the University of Manchester. For their collaboration and for providing access to optical engine I would like to thank Prof Hua Zhao and Mohammandreza Anbari Attar from Brunel University. Special thanks to Dr Steve Begg and Dr Daniel Coren from the University of Brighton and the staff in Sir Ricardo Laboratories for supporting our project by providing access to an optical engine and their expertise on operating it.

This project was funded by EPSRC and Innospec Inc., to whom I am very grateful. Especially, I would like to express my heartfelt gratitude to Paul Richards, Jim

Barker and Ian McRobbie from Innospec Inc. for their support and expertise throughout this project.

Finally, I would like to thank all my friends around the world and my family back home for their support and encouragement. I would be forever indebted to my parents for having faith in me and for all the sacrifices they made, to provide me with the best possible education.

List of Publications

1. Karagiannopoulos S, Cheadle EM, Wright P, Tsekenis SA, and McCann H, "*Multi-wavelength diode-laser absorption spectroscopy using external intensity modulation by semiconductor optical amplifiers*," Appl. Opt., Vol. 51, Iss 34, p. 8057 (2012)
2. S. Karagiannopoulos, E. Cheadle, P. Wright and Hugh McCann, *'Diode Laser Wavelength Control for High-Speed Chemical Species Tomography,'* WCIPT 6, Beijing, China (2010)
3. Karagiannopoulos S, Cheadle EM, Wright P, Ozanyan KB and McCann H, *Towards water imaging in a single-cylinder research engine*, Proc. 6th Int. Symp. on Process Tomography (ISPT-6), PO17, Cape Town, South Africa, (2012).
4. Cheadle E, Karagiannopoulos S, Wright P, Terzija N, Ozanyan K and McCann H, *Measurement Strategies for In-Cylinder Water Imaging in a Homogeneous Charge Compression Ignition Engine*, Proc. 6th World Congr. Industrial Process Tomography, 1368-1375, Beijing, China, Sept. (2010).
5. Cheadle EM, Karagiannopoulos S, Terzija N, Wright P, Ozanyan KB and McCann H, *Fuel spray and vapour imaging in a single-cylinder research engine*, Proc. 6th Int. Symp. on Process Tomography (ISPT-6), OR18, Cape Town, South Africa, (2012).

Chapter 1

Introduction

1.1 Motivation

Despite the significant efforts and advances towards the development of environmental friendly renewable energy sources, internal combustion (IC) systems are anticipated to dominate in the automotive industry at least in the foreseeable future [1]. It is well known that IC engine operation comes with a cost as it relies on burning of natural resources such as fossil fuels, which are generally limited and have a significant environmental impact in terms of pollution and emissions. Over recent decades strict emission regulations have been imposed on automotive manufacturers with regards to fuel efficiency and the emissions of pollutant gases such as carbon monoxide and dioxide (CO - CO_2) and nitric and sulphuric oxides (NO_x - SO_x) [2]. Emission regulations are anticipated to become even more demanding in the future and this has triggered a lot of research towards combustion process optimisation. Improved combustion efficiency can be achieved by enhancing our understanding of the underlying chemical reactions, as well as by optimizing the engine design. In this direction, a number of quantitative measurement techniques for critical gas parameters have been developed, such as chemical species concentration distribution, pressure, velocity and temperature, especially for new modes of engine operation such as homogeneous charge compression ignition (HCCI) (sometimes called controlled autoignition), partially premixed compression ignition and exhaust gas recirculation [3].

Diode Laser-based sensors have been dominant in gas sensing applications over the last 20 years [4,5,6,7]. Major advances in semiconductor technology have made available high power, fast response, small footprint, low cost, coherent light sources which are ideal for low-concentration gas spectroscopic measurements. The principle behind most of these sensors' operation is probing a sample gas with a laser beam and measurement of the transmitted optical power with relation to wavelength. Spectral coherence or monochromaticity of diode lasers facilitates high-resolution spectroscopic monitoring of gas molecules which are usually blended with other species in harsh environments. A great advantage of such optical sensors is that, in contrast to traditional sensing methods like sampling with physical probes and thermocouples, optical sensors do not disturb the process itself and therefore they yield more accurate results, and thus are called "non-intrusive". Nowadays diode laser gas sensors have numerous applications in combustion diagnostics [4], industrial processes [8], agricultural emissions [9], atmospheric/pollution monitoring [10] and medical diagnostics [11].

Different molecular species are characterised by the amount of electromagnetic energy they absorb at specific wavelengths, which constitute the absorption spectrum of each molecule. Diode lasers are now available in a very large portion of the electromagnetic spectrum, from visible (400 nm) to mid-infrared (30,000 nm), which facilitates measurements of numerous chemical species. Especially in the near-Infrared (IR) wavelength region used by telecoms (1300 – 1700 nm) compact, low-power consumption, room temperature laser sources, and the associated optoelectronic equipment (i.e. detectors, couplers, multiplexers) are readily available. Even though the molecular rotation-vibration related absorption features in the near-IR are only overtones, and much weaker than the fundamental mid-IR

transitions, high resolution measurements can be achieved [7]. Tunable Diode Laser Absorption Spectroscopy (TDLAS) is a widely adopted sensing method, where a spectrally narrow output diode laser is used to interrogate absorption lines of species under investigation. A detailed description of the theory and the basic principles of this method are given in Chapter 2.

In combustion diagnostics several TDLAS gas sensors have been developed for various chemical species such as CO, CO_2, O_2, H_2O, NO_x and larger Hydrocarbon (HC) molecules. H_2O vapour measurements in particular, have attracted a lot of attention since water is one of the primary combustion products and there are numerous absorption features both in mid and near-IR regions which are convenient to probe. More interestingly, water absorption lines are highly sensitive to pressure and temperature variations and TDLAS is today a well established method for ratiometric thermometry in combustion systems. This approach is based on measuring the relative absorption of two different transitions and using spectral parameters of the selected wavelengths usually found in Spectral databases such as HITRAN [12]. Using multiple, planar line-of-sight projections and appropriate mathematical image reconstruction algorithms, 2-dimensional images of the concentration and temperature distribution can be created. In-cylinder imaging techniques in combustion systems are commonly used for imaging of liquid spray, fuel vaporisation, combustion, as well as soot and NO formation. The following section expands upon combustion diagnostics and related technology.

1.2 Combustion Diagnostics

The most commonly used optical combustion diagnostics include linear techniques, where the measured signal intensities are directly and linearly proportional to the

input signals, such as Absorption Spectroscopy, Laser Induced Florescence (LIF), Laser Induced Incandescence (LII), soot particles Chemiluminescence (CL), and Particle Imaging Velocimetry (PIV) as well as non-linear techniques, where the measured signals are proportional to higher powers of the incident laser signal (and thus "non-linear"), such as Coherent anti-Stokes Raman spectroscopy (CARS), Degenerate Four-Wave Mixing (DFWM), Laser Induced Grating Spectroscopy (LIGS) and Polarization Spectroscopy (PS). Each of these diagnostic approaches has its own merits and shortcomings but the general aim is to achieve in situ, non intrusive, in-cylinder measurements with high spatial and temporal resolution, which are directly sensitive to the target species, but also robust against the hostile thermodynamic combustion environment and non-species-specific optical effects. It is also highly desirable that the sensor's sensitivity can cover a wide dynamic range of species concentration, from 100 parts per million by volume (ppm) to tens of thousands of ppm. Applicability to multi-cylinder engines as well as single-cylinder research engines is also highly desirable. This thesis focuses mostly on linear diagnostics and specifically on Absorption Spectroscopy.

1.1.1 *Planar Laser Induced Fluorescence*

Planar Laser Induced Fluorescent (PLIF) imaging is a widely used method for visualisation of flow-field parameters such as concentration, temperature, velocity, pressure and density [13,14]. An arrangement of lenses produces a laser sheet, typically at Visible and Ultraviolet (UV) wavelengths, which is pitched across an IC engine through optical windows. The laser sheet excites the chemical species of interest some of which, when de-excited, generate a fluorescent light signal at longer wavelengths. In optically accessible IC engines, an arrangement of mirrors and charge-coupled device (CCD) or CMOS cameras are used to capture the

fluorescence signal emitted by the species under investigation. The most commonly used laser sources for PLIF applications are pulsed, diode-pumped, frequency-doubled, Nd:YAG or dye lasers with high pulse-rate. Numerous in-cylinder applications have been reported for NO [15], OH [16] and intermediate combustion products such as formaldehyde (CH_2O) [16,17] which is formed in the early stages of the ignition process and subsequently consumed [18]. PLIF offers great spatial resolution but the temporal resolution or frame rate is limited by the laser pulse repetition rate and the camera frame rate. Recently high-speed PLIF imaging with frame rates higher than 1 kHz have been reported [19] but with a cost of limited measurement duration due to memory limitations and lower pixel resolution. The main disadvantages of PLIF in engine applications are that, for quantitative fuel imaging, only model fuels can be used with fluorescent tracers added, and that, otherwise it is restricted to the reaction zones. LIF imaging with commercial diesel and gasoline fuels has been also reported [15,20] but it suffers from strong fluorescence interference by unburned aromatic components, and it is therefore not quantitative.

1.1.2 *Absorption Spectroscopy in IC engines*

TDLAS gas sensors have been extensively studied and demonstrated in laboratory devices such as shock tubes and flame burners [21,22], and combustion plants such as SCRAMJET combustors [23,24], coal-fired power plants [25], and pulse detonation engines [26,27]. There are a limited number of implementations on actual IC engines. Most of the above works are focused on small molecular-weight species such as O_2, H_2O, CO, CO_2, NO_x, OH and HC molecules with typical linestrengths between 10^21 and 10^23 cm/molecule [28]. In typical applications multiple

narrow-linewidth tunable Distributed Feedback (DFB) lasers are tuned and multiplexed in order to probe predetermined absorption features in a continuous, fixed-wavelength mode [26]. A direct TDLAS, wavelength-multiplexed technique for temperature and water vapour concentration measurements, has been demonstrated by Mattison et al. (2007) [29]. In that work a fixed-wavelength, multiplexed technique has been applied for crank-angle resolved, line-of-sight H_2O absorption measurements on an optically accessible gasoline-based HCCI engine. Two appropriately chosen H_2O spectral absorption features were probed simultaneously with two DFB lasers and a third non-resonant laser used to track non-absorption-related noise. This is a particularly attractive technique as it provides quantitative measurements by completely non-intrusive means (a fused silica ring attached to the top of the cylinder). Moreover the wavelength multiplexing approach can be further expanded by incorporating additional wavelengths and probing more spectral features or species of interest.

Scanned-wavelength TDLAS techniques where the laser source is wavelength-tuned to interrogate entire absorption features are generally limited by the slow scanning time and by spectral broadening effects at high temperatures and pressures. Spectral lines of gas phase molecules are not infinitely narrow due to their constant motion relative to the observer. Their kinetic energy is proportional to the temperature, due to the thermal effect, and to pressure due to molecular collisions. The various line broadening mechanisms are described in detail in paragraph 2.2. Kranendonk et al. [30] demonstrated a high-speed scanning wavelength absorption spectroscopy technique for temperature and H_2O mole fraction measurements in a controlled HCCI engine. An external cavity diode laser was being used for a wavelength-agile sensor with about 50 nm scanning range (1130 – 1380 nm) at 200 kHz, so that it can

potentially be used for tracing of multiple combustion gases. In order to achieve higher scanning speed and broader spectrum, a laser active medium (tunable etalon) is used, thus overcoming the limitations of spontaneous emission time constants. The main problem with this approach is that the proposed complex laser source is susceptible to intensity noise and mode-beating noise. This limits the ability accurately to probe specific narrow spectral features, with consequent poor performance for low species concentration in low pressures and high noise environments. Finally, due to the excessively large acquired data files the requirements of the data acquisition system and reduction system are very high.

Wavelength Modulation Spectroscopy (WMS) with second harmonic (2f) detection is a well known absorption spectroscopy method which offers improved sensitivity and Signal to Noise Ratio (SNR) compare to the direct TDLAS [22,31,32]. Large modulation depth WMS-2f has been applied to water vapour concentration and temperature measurements in an internal combustion engine by Rieker et al. 2007 [33]. An optical sensor probe has been attached to a spark plug of a test IC engine. Near-IR DFB lasers employed to probe two selected absorption features, were modulated and multiplexed before being pitched through a sapphire window into the combustion chamber. The transmitted beam was then reflected back through a mirror on the piston surface, to a multimode fibre attached to the probe. By estimating the pressure based on the crank angle position and by taking the ratio of the optical absorption for the two measured transitions, the temperature and subsequently the water concentration are determined. An innovative calibration strategy for non-absorption attenuation has been employed in that work, where the magnitude of the 2f harmonic was normalised with the first harmonic (1f) signal in order to account for non-species related intensity variations [32].

Recent advances in Quantum Cascade Lasers (QCL) gave momentum to mid-IR absorption measurements for combustion systems [34,35,36,37,38]. QCLs can deliver hundreds of milliwatts of optical power in a narrow linewidth beam (<0.001nm) which can be used to monitor fundamental absorption features in order to extract continuous quantitative temperature and chemical species concentration information. Vanderover and Oehlschlaeger reported CO mole fraction and temperature measurements at 4.6 μm in a shock-heated tube for a wide set of temperatures (950-3500 K) at atmospheric pressure with a direct scanned-wavelength approach in [34], and improved sensitivity measurements with a 50 kHz WMS-2f in [35]. Ren et al [37] performed similar CO measurements in a shock tube over 1100-2000 K temperatures with both scanned-wavelength at 2.5 kHz and fixed-wavelength direct absorption. Chao et al [36] performed NO measurements at 5.2 μm in a pulverized-coal-fired power plant boiler at atmospheric temperatures with 1f normalised WMS-2f. H_2O concentration and temperature in rapid compression machine at 11.5 bar and about 1000 K, near 7.6 μm with a scanned wavelength approach, have been reported in [38].

1.3 **Previous work and scope**

In-cylinder chemical species tomography (CST) with near-IR absorption, has been implemented both in single and multi-cylinder IC engines by the University of Manchester group, as part of a research program known as IMAGER [39,40,41,42]. High-speed Hydrocarbon spray and gas distribution imaging was performed using a dual-wavelength scheme with high-frequency intensity modulation for phase-sensitive, lock-in detection. The multiplexed signal was split to multiple beams before being pitched across the IC engine through an optical window. Sophisticated

optical access methods have been developed as well as powerful image reconstruction algorithms designed to deal with limited data situations [43]. This system offers quantitative capability and great temporal resolution of about 120 frames per engine revolution, but lacks in terms of spatial resolution when compared with alternative optical imaging techniques such as PLIF. Thus we consider these two methods highly complementary for studying in-cylinder phenomena. Major challenges of the tomography technique include limited optical access in an engine environment, beam displacement due to mechanical vibrations, modal noise and back-reflections, beamsteering effects from rapid temperature and pressure variations, and signal attenuation from window fouling and oiling. Also the method's accuracy is highly dependent on precise knowledge of spectroscopic parameters from spectral databases such as HITRAN, which have been shown [44] to be not always reliable especially at elevated temperatures and pressures; this problem applies to TDLAS in general.

The main objective of the work described this thesis is the optoelectronic design of a CST system for in-cylinder H_2O vapour concentration distribution measurements during Intake and Compression strokes in a running IC engine. This water sensing system was built in order to take full advantage of the robust, low-noise electronics designed and built by our group for the HC measurements. A number of potential TDLAS approaches such as direct and wavelength modulation absorption spectroscopy are extensively discussed here. The near-IR spectroscopic line selection process, which is very critical for accurate ratiometric measurements, is also described. A novel approach using Semiconductor Optical Amplifiers (SOAs) for amplification, optical switching and external intensity modulation for phase-sensitive lock-in detection has been developed. Limitations and challenges for the engine

measurement case have been addressed. The new scheme has been demonstrated both in laboratory experiments and on an optical IC engine.

1.4 Structure of this thesis

In Chapter 2 the basic theory and principles of absorption feature formation and TDLAS are addressed, as well as the various different approaches such as direct and WMS spectroscopy. Dual-wavelength ratiometric thermometry used in this work is also addressed.

In Chapter 3 the H_2O absorption line selection process is outlined and a number of possible configurations for a multi-wavelength, multi-channel tomographic system are presented. The advantages and disadvantages of these schemes are discussed under the scope of the requirements of our system. The architecture of a newly proposed scheme based on optical switching and external intensity-modulation with Semiconductor Optical Amplifiers (SOAs) is presented. A flexible signal adjustment circuit for generating the appropriate driving electronic signals is also designed, built and tested.

In Chapter 4 a brief introduction to SOAs is given and a device is tested based on the system's requirements such as wavelength stability, broadband amplification, switching and amplitude modulation. Simultaneous intensity-modulation and switching with the SOA are also performed and the signal quality is assessed.

In Chapter 5 the proposed scheme is tested in a controlled laboratory environment by measuring the atmospheric air humidity content. Using a scanned wavelength approach and two DFB probe lasers, the entire selected absorption spectra of the related features are recovered with great accuracy and precision. Various signal

capture approaches have been compared. A real-time wavelength tracking scheme has been also developed and utilised.

A three-colour, Time-Division-Multiplexed, fixed-wavelength scheme for water absorption measurements is presented in Chapter 6. The system is tested in controlled laboratory conditions and shows better than 3% temperature measurement accuracy, based on rationing of the absolute absorption of the selected wavelengths. A set of preliminary tests on an optically accessible IC engine is presented as well. Three beams are monitored continuously at 150 KS/sec throughout consecutive cycles during motored, fuelled and fired engine operation. A qualitative analysis of the results is performed and presented.

Finally, Chapter 7 presents a set of species tomography tests and reconstructed images of HC concentration distribution in an optical engine for motored and fuelled operation. Optical access is achieved with a new scheme based on a horizontal planar array with 32 collimated beams, mounted on a plate with accurately machined V-grooves. Post-processing for robust assessment of the recorded data is applied using sophisticated tools such as Wavelet Denoising. Image reconstruction of liquid fuel spray distribution during injection, and fuel vapour during the compression stroke are presented.

Chapter 2

Tunable Diode Laser Absorption Spectroscopy

2.1 Introduction

Tunable Diode Laser Absorption Spectroscopy (TDLAS), as a non-intrusive method for measuring dynamic gas properties such as species concentration, temperature, pressure, and flow velocity has been extensively studied and demonstrated over the last two decades. High temporal resolution measurements for both one- and two-dimensional measurements have been reported (29,42,45,46,47). The fundamental theory behind Diode Laser Absorption Spectroscopy is well documented in the literature (21,28,48,49) and will be briefly described here.

2.1.1 *Absorption Features Formation*

The internal energy states of atoms and molecules are described by quantized energy levels [50,51,52]. A certain atom or molecule can possess a number of different forms of quantised energy levels such as electronic, rotational and vibrational levels. For example, the rotational and vibrational energy state of a molecule is one of a discrete set of energy states. Figure 2.1 illustrates two discrete energy states (electronic, rotational or vibrational) of a particle (atom or molecule) and the possible transitions that can occur between level E_1 and E_2. The transition of a particle between different energy states can be achieved by either emission or absorption of electromagnetic energy. Absorption of electromagnetic energy will occur when electromagnetic energy matching the energy gap collides with a particle

and force it to 'jump' to a higher energy state. The amount of electromagnetic energy that is required for such a transition to take place is given by Eq. 2.1.

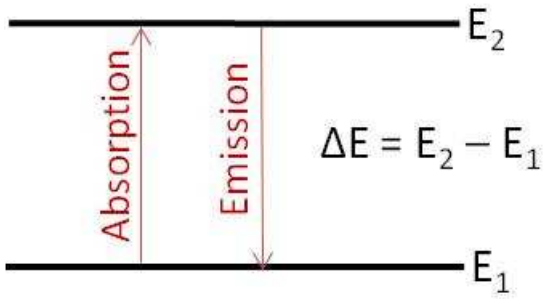

Figure 2.1 Absorption and emission between two energy levels

$$\Delta E = h\nu = \frac{hc}{\lambda} \tag{2.1}$$

where h is Plank's constant ($6.33*10^{-34}$ J.s), ν is frequency and λ is the wavelength. From the Eq. 2.1 it is obvious that the electromagnetic energy that is necessary for the transition ΔE to take place is related with the frequency or the wavelength of the incident radiation. Thus, if a coherent monochromatic light beam with appropriate wavelength is incident upon a particular molecule, then a portion of that light will be absorbed. This absorption will appear as attenuation of the incident intensity on a receiving photo-detector. If the incident light is of different wavelength, then it will travel through the molecule unaffected. When a tunable laser source is used to scan the wavelength across the absorption peak then the transmitted intensity will have a 'dip' at the resonant wavelength. This 'dip' is usually called absorption spectral feature or transition. Ideally, absorption features would be infinitely narrow but in reality they have finite width, which is mainly due to the fact that energy levels are not absolutely sharp and to the constant motion of the particles relative to the observing point [50]. The spectral width of an absorption line depends on a number of broadening mechanisms which are discussed in Section 2.2.2.

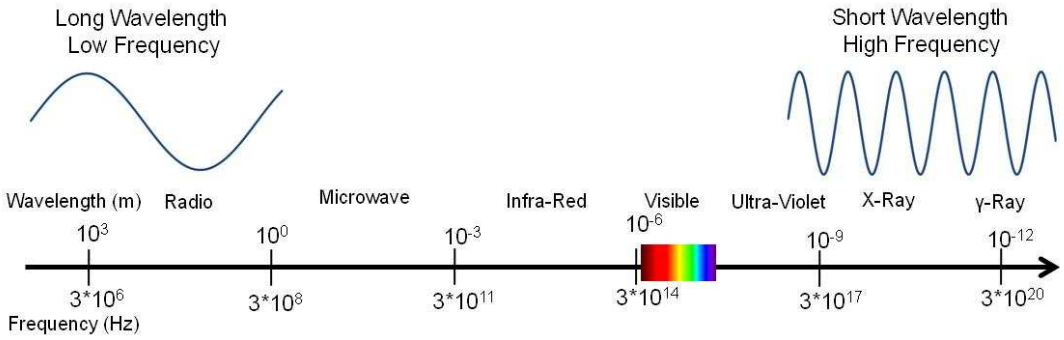

Figure 2.2 Electromagnetic Spectrum

Electromagnetic radiation has been divided in a number of different regions (Figure 2.2) based upon the atomic or molecular processes associated with each one of them. In the radio-wavelength region between 10^3 – 1 m, the energy difference between energy levels is related to the electron or nucleus spin and it is in the order of 0.001-10 J/mole [50]. Energy changes changes related to the rotation of the molecules are prevalent in the microwave region with wavelengths between 1 m and 1 mm. Rotation of molecules gives rise to a periodic change in their internal energy or dipole moment. Electromagnetic interaction with this rotational molecule's dipole moment causes energy changes in the order of hundreds of Joules per mole for each transition. In the Infra-red region (1 mm – 1 μm) energy transitions are related to the interaction of electromagnetic energy with the dipole moment vibrations and they are in the order of 10^4 Joules per mole. In the visible and ultra-violet region (1 μm – 10 nm) electronic transitions of the valence electrons have energy content of about a few hundred kilojoules per mole. The X-ray transitions take place between 10 nm – 100 pm and are related to inner electrons with energy changes up to tens of thousands of kilojoules per mole. Finally, in γ-ray region (100 pm – 1 pm) transitions are related to the rearrangement of nuclear particles with associated energies of 10^9 - 10^{11} joules per mole.

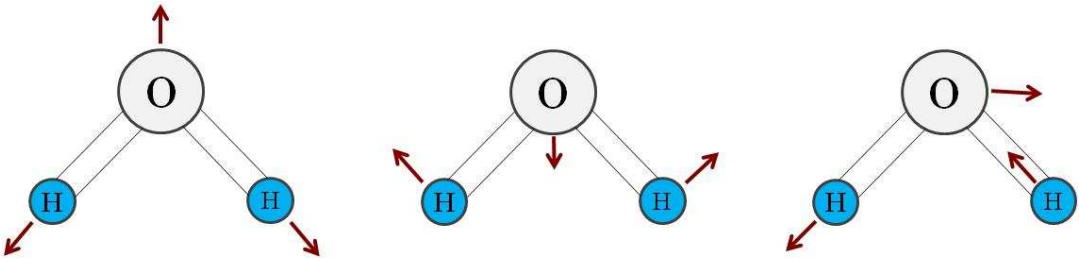

Figure 2.3 Water vapour molecule fundamental vibrations: a) Symmetric stretch (ν_1 = 2738.45 nm), b) Symmetric bend (ν_2 = 6269.59 nm), and c) Antisymmetric stretch (ν_3 = 2662.55 nm)

In this work we focus on the water vapour absorption spectroscopy in the IR region. H_2O is a tri-atomic, non-linear (atoms are not in a straight line) molecule and the total vibration in the gas phase includes three fundamental vibrations as shown in Figure 2.3. The first two vibrations are a symmetric stretch (ν_1) and a symmetric bend (ν_2) and the third is an asymmetric stretch (ν_3) [53]. These vibrations are combined with the molecular rotations [54] which are also quite complex to create the total rotational-vibrational absorption spectrum. Also the very small moment of inertia of the water molecule further complicates the IR absorption spectrum and gives rise to thousands of transitions [50]. More interestingly since the fundamental vibrations are not simple harmonic oscillations, and this gives rise to higher order harmonic vibrations at multiples of the fundamental frequencies (i.e. $2\nu_1$, $3\nu_1$, etc) which called overtones. Overtones are generally weaker compare to the fundamental vibrations and can also overlap creating combination bands [51]. As shown in Figure 2.4 the overtone and combination bands $2\nu_3$, $\nu_1+\nu_3$ and $2\nu_1$ conveniently appear in the Near-IR region, where absorption spectroscopy is facilitated by the recent advances in semiconductor lasers.

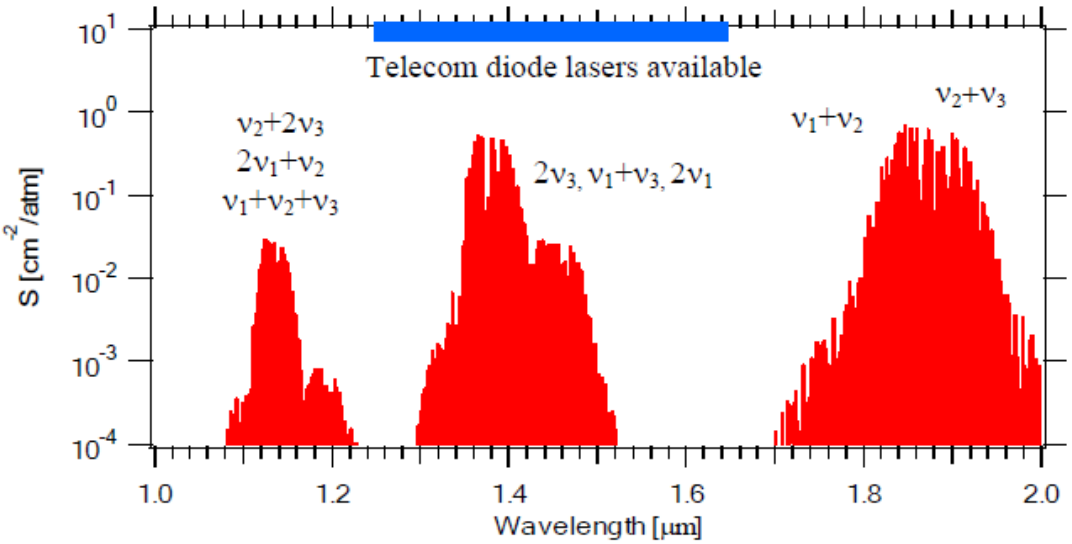

Figure 2.4 Water vapour transition overtones and combinations in the Near-IR.[55]

2.2 Direct Absorption Spectroscopy

2.2.1 *Beer-Lambert Law*

The loss of electromagnetic energy (i.e. absorption) of a collimated light beam when it propagates through a uniform gas medium, as illustrated in Figure 2.5, follows the Beer-Lambert relation:

$$I(\nu) = I_0(\nu)\exp(-\alpha_\nu) \tag{2.2}$$

Where, $I_0(\nu)$ is the intensity of the incident light beam, $I(\nu)$ is the received intensity at frequency ν (cm^{-1}), and α_ν is the spectral absorbance for this gas path at frequency ν.

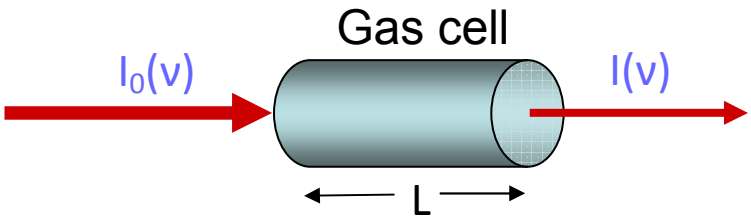

Figure 2.5 Absorption measurement schematic

The spectral absorbance is given by:

$$\alpha_{\nu} = Px_{abs}S(T)\varphi(\nu)L \tag{2.3}$$

Where, P is the pressure in Atmospheres, x_{abs} is the mole fraction of the species, L is the path length in centimeters, T is the temperature in Kelvin, $S(T)$ (cm^{-2}/atm) is the line strength and $\varphi(\nu)$ (cm) the lineshape function of the absorption feature. Therefore, by measuring the intensity loss along the beam path we can make quantitative calculations for concentration, temperature and pressure. The linestrength function $S(T)$ is a function of temperature and is given by [45]:

$$S(T) = S(T_0)\frac{Q(T_0)}{Q(T)}\left(\frac{T_0}{T}\right)\exp\left[-\frac{hcE''}{k}\left(\frac{1}{T}-\frac{1}{T_0}\right)\right]\frac{\left[1-\exp\left(\frac{-hc\nu_0}{kT}\right)\right]}{\left[1-\exp\left(\frac{-hc\nu_0}{kT_0}\right)\right]} \tag{2.4}$$

Where $Q(T)$ is the partition function of the absorbing molecule, T_0 is the reference temperature (296 K), h (Js) is Planck's constant, c (cm/s) is the speed of light, E'' (cm^{-1}) is the lower state energy of the transition, k (J/K) is Boltzmann's constant and ν_0 is the transition linecentre frequency. The temperature dependency of the linestrength of a transition is controlled by the lower state energy E'', which determines the equilibrium molecular population.

2.2.2 *Lineshape function*

From equations 2.2 – 2.4 it is clear the linestrength of the absorption depends on the temperature and the lineshape on frequency. The lineshape function $\varphi_c(v)$ is very important as it describes how spectral absorbance varies with frequency. The spectral lineshape depends on the broadening mechanisms that influence the transitions between the energy levels of the feature, and the type of interaction between the species under test and the light beam. From these physical mechanisms, pressure (or collisional) broadening, velocity (or Doppler) broadening and line shifting are the most important for our experiments and will be summarised here.

Pressure broadening and spectral line shifting are the result of inter-molecular collisions which cause perturbations of the energy levels. In absorption spectroscopy these collisions are usually assumed to be binary and the collision duration negligibly short. The collisional lineshape function has a Lorentzian profile [55]:

$$\varphi_c(v) = \frac{1}{\pi} \frac{\frac{\Delta \nu_c}{2}}{(\nu - \nu_0)^2 + (\frac{\Delta \nu_c}{2})^2} \tag{2.5}$$

$\Delta \nu_c$ is the collisional Full Width at Half Maximum (FWHM) and ν_0 is the central frequency of the line. The collisions can take place between molecules of the same species (self-broadening) or between molecules of different species (foreign-gas broadening). Assuming that all the collisions are binary, the spectral collision width and shift are directly proportional to the pressure when temperature is constant. Hence as the pressure increases the absorption lines are broadening.

Doppler broadening originates from the random thermal motion of the absorbing molecules. The theory of statistical mechanics states that the velocity distribution of

molecules is Maxwellian. Thus the Doppler lineshape function has a Gaussian profile [48]:

$$\varphi_D(\nu) = \frac{2}{\Delta\nu_D}\sqrt{\frac{\ln 2}{\pi}}\exp\left[-4\ln 2\left(\frac{\nu-\nu_0}{\Delta\nu_D}\right)^2\right] \qquad (2.6)$$

where $\Delta\nu_D$ is the Doppler FWHM and ν_0 is the linecentre frequency. $\Delta\nu_D$ is given by:

$$\Delta\nu_D = \nu_0\sqrt{\frac{8kT\ln 2}{mc^2}} \qquad (2.7)$$

Where, m is the atomic mass of the absorbing species. Doppler broadening increases with temperature and thus, the higher the temperature is the wider the absorption feature is.

The overall lineshape of a transition is usually a combination of these two broadening mechanisms (plus 'natural' broadening which is usually neglected). When the pressure is high the collisional broadening is predominant, whereas at low pressures the Doppler broadening becomes more significant. In the general case these two mechanisms are considered to be statistically independent and the overall broadening is calculated by the convolution of the Lorentzian and Gaussian lineshapes. The lineshape product of this convolution is given by a Voigt lineshape function [48]:

$$\varphi_V(\nu) = \int_{-\infty}^{+\infty}\varphi_D(v)\varphi_C(v-u)du = \frac{2}{\Delta\nu_D}\sqrt{\frac{\ln 2}{\pi}}V(\alpha_V, w) \qquad (2.8)$$

Where $V(\alpha_V,w)$ is the normalised Voigt function, with:

$$\alpha_V = \sqrt{\ln 2}\,\frac{\Delta v_c}{\Delta v_D} \tag{2.9}$$

and

$$w = 2\sqrt{\ln 2}\,\frac{v - v_0}{\Delta v_D} \tag{2.10}$$

The first of these parameters α_V, represents the relative influence of the two broadening mechanisms and the second w, is an indication of how far is the feature from the line centre. The Voigt profile is the most commonly used function for absorption spectroscopy quantitative measurements, and in most cases is calculated numerically.

2.3 **Wavelength Modulation Spectroscopy**

In Wavelength Modulation Spectroscopy (WMS) a high frequency sinusoid signal is used to modulate the diode-laser wavelength through the applied injection current. Then a lock-in amplifier in the detection circuit is used to employ phase-sensitive detection on the modulated signal. Shifting the detection bandwidth to higher frequencies is a very efficient way to remove unwanted low frequency components such as laser excess noise (1/f noise) and improve the signal-to-noise ratio (SNR). Laser wavelength modulation also induces intensity modulation of the light beam which is out of phase with the former. In addition to that, the interaction between the modulated signal and the non-linear absorption peak gives rise to higher order harmonic components which can also be locked-in by the detection circuit. WMS with second harmonic (2f) detection is the most commonly used method as the 2f signal is highly dependent upon the spectral characteristics of the measured gas absorption lines. WMS has been extensively studied and documented by many

researchers [31,56,57] in the past. Here a brief summary of the fundamental theory is given.

As described above, in order to shift the measurement bandwidth to higher frequencies a sinusoid modulating signal with angular frequency $\omega = 2\pi f$ is superimposed on the diode laser injection current. In this case the values of the instantaneous transmitted laser frequency $\nu(t)$ and intensity $I_0(t)$ are given by:

$$\nu(t) = \bar{\nu} + a\cos(\omega t) \tag{2.11}$$

$$I_0(t) = \overline{I_0} + i_0\cos(\omega t + \psi) \tag{2.12}$$

where $\bar{\nu}$ is the centre laser frequency, a is the modulation amplitude, $\overline{I_0}$ is the average laser intensity, i_0 is the total intensity modulation amplitude and ψ the phase shift between the wavelength and the intensity modulation, assuming a linear relationship between the two. A non-linear phase shift appears for large modulation amplitude in which case it cannot be neglected. The light intensity on the photo-receiver is now given by the Beer-Lambert relation (Eq.2.2) as follows:

$$I(t) = I_0(t)\exp(-\alpha(\bar{\nu} + a\cos(\omega t))) \tag{2.13}$$

Assuming the spectral absorbance is less than 0.1, then Eq. 2.13 becomes:

$$I(t) = I_0(t)(1 - \alpha(\bar{\nu} + a\cos(\omega t))) \tag{2.14}$$

Expanding the even periodic function of the spectral absorbance in Fourier cosine series [56] gives:

$$\alpha(\bar{\nu} + a\cos(\omega t)) = -\sum_{k=0}^{\infty} H_k(\bar{\nu}, a)\cos(k\omega t) \tag{2.15}$$

From Eq. 2.15 the Fourier coefficients $H_k(\bar{\nu}, a)$ are given by [58]:

$$H_0(\bar{\nu}, a) = -\frac{1}{2\pi}\int_{-\pi}^{\pi} \alpha(\bar{\nu} + a\cos\theta)d\theta \tag{2.16}$$

and

$$H_k(\bar{\nu}, a) = -\frac{1}{\pi}\int_{-\pi}^{\pi} \alpha(\bar{\nu} + a\cos\theta)\cos k\theta d\theta \tag{2.17}$$

where $\theta = \omega t$. Substituting from Eq. 2.3:

$$H_0(\bar{\nu}, a) = -\frac{Px_{abs}L}{2\pi}\int_{-\pi}^{\pi} \sum_i S_i(T)\varphi_i(\bar{\nu} + a\cos\theta)d\theta \tag{2.18}$$

and

$$H_k(\bar{\nu}, a) = -\frac{Px_{abs}L}{\pi}\int_{-\pi}^{\pi} \sum_i S_i(T)\varphi_i(\bar{\nu} + a\cos\theta)\cos k\theta d\theta \tag{2.19}$$

where i runs over all transitions within the range covered by Eq. 2.11. The received signal is then passed through a high pass filter to remove any DC offsets before it is fed to a lock-in amplifier which is either locked-in to the fundamental modulation frequency f or the 2f harmonic. This is done by multiplying the detected signal with a sinusoidal reference signal with the desired frequency (1f or 2f) and in a fixed-phase relationship with the modulation signal. The result of this multiplication contains a DC component which relates directly to the amplitude of the high-frequency signal and all the unwanted signals of different frequency are rejected with a Low Pass filter. The magnitude of the resulting 1f and 2f signals [55] for zero phase shift between the signal at the detector and the reference signal, is calculated as:

$$R_{1f} = \frac{G\overline{I_0}}{2}\left\{\left[H_1 + i_0\left(1 + H_0 + \frac{H_2}{2}\right)\cos\psi_1 + \frac{i_2}{2}\left(H_1 + H_3\right)\cos\psi_2\right]^2 + \right.$$

$$\left. + \left[i_0\left(H_0 - \frac{H_2}{2}\right)\sin\psi_1 + \frac{i_2}{2}\left(H_1 - H_3\right)\sin\psi_2\right]^2\right\}^{1/2} \qquad (2.20)$$

and

$$R_{2f} = \frac{G\overline{I_0}}{2}\left\{\left[H_2 + \frac{i_0}{2}\left(H_1 + H_3\right)\cos\psi_1 + i_2\left(1 + H_0 + \frac{H_4}{2}\right)\cos\psi_2\right]^2 + \right.$$

$$\left. + \left[\frac{i_0}{2}\left(H_1 - H_3\right)\sin\psi_1 + i_2\left(1 + H_0 - \frac{H_4}{2}\right)\sin\psi_2\right]^2\right\}^{1/2} \qquad (2.21)$$

where G is the gain of the of the detection system, i_2 is the amplitude of the first term of the non-linear laser intensity modulation and ψ_1 and ψ_2 correspond to the phase shifts between the laser intensity modulation and the wavelength modulation for linear and non-linear intensity modulation, respectively. The last two equations can be further simplified [55] depending on the operating conditions (small or large absorption) and the various parameters, such as the modulation index, m defined as the ratio of the frequency deviation $\delta\nu$ of the modulation signal to the Half Width Half Maximum (HWHM) of the absorption feature. It has been shown in [31] that for Lorentzian, Doppler and Voight absorption lineshapes the magnitude of the 2f component is maximised when m = 2.2. For elevated pressures where the absorption lines are significantly broadened a larger modulation depth is required. However from equation 2.21 and R_{2f} have a non-zero value when the absorption becomes zero, H_k =0,

$$R_{2f}{}^0 = \frac{G\overline{I_0}}{2} i_2 \qquad (2.22)$$

which in the literature is referred to as the Residual Amplitude Modulation (RAM) [59,60,61]. The actual RAM value is negligible for small modulation depth, but becomes significant as the latter increases since the i_2 term has quadratic dependence on the modulation amplitude [62]. This RAM signal arises from the non-linear modulation response of diode-lasers and it can be cancelled out by adding an appropriate second harmonic component to the laser modulation signal. Alternatively, it can be directly measured by purging the transmission path, and subsequently subtracted from the total 2f signal in order to calculate the pure 2f absorption related signal. In order to account for the detection gain and non-species-related attenuation effects such as laser noise, beam steering and window fouling, the 2f signal is normalised to the measured 1f signal [32]. The resulting 1f normalised 2f WMS signal can be expressed as [48]:

$$R_{2f/1f} = \frac{R_{2f}}{R_{1f}} \simeq \frac{1}{i_0}\left\{\left[H_2 + \frac{i_0}{2}(H_1 + H_3)\cos\psi_1 + i_2\left(H_0 + \frac{H_4}{2}\right)\cos\psi_2\right]^2 + \right.$$

$$\left. + \left[\frac{i_0}{2}(H_1 - H_3)\sin\psi_1 + i_2\left(H_0 - \frac{H_4}{2}\right)\sin\psi_2\right]^2\right\}^{1/2} \qquad (2.23)$$

which can be simplified depending on the modulation amplitude and the measurement conditions (absorber concentration and pressure). WMS can be implemented in either scanned or fixed-wavelength configuration. One of the major benefits of the 2f-WMS technique is that it is not necessary to scan across the full absorption line especially in high pressure applications where broadening and blending effects render this impossible [58].

2.4 **Multi-line Temperature Ratiometric Measurements**

Two-line absorption spectroscopy has been previously described theoretically [45,63] and implemented in IC engines and other combustor types [26,29,30,64]. It has been proven that by taking the ratio of two different absorbing transitions and for known pressure, the temperature can be deduced as shown below and the mole fraction of the target species can be inferred. This so-called 2-line thermometry can be implemented both in scanned and fixed wavelength mode. In the first case by taking the ratio of the integrated absorbance of two simultaneously measured transitions of the same sample, the temperature can be inferred.

$$A = Px_{abs}S(T)L \tag{2.24}$$

$$R_T = \frac{A_1}{A_2} = \frac{S_1(T)}{S_2(T)} \tag{2.25}$$

where A is the integrated spectral absorbance for any line, i.e A_1, and A_2 that is used. As shown in Eq. 2.25 the ratio of the integrated absorbance of two different lines is only a function of temperature as long as the pressure, the mole fraction and the path length are the same. From Eq. 2.4 and 2.25 and by neglecting the (1-exp(x)) terms assuming the two lines are relatively close in the frequency domain [48,49], the temperature can be obtained by Eq. (2.26):

$$T = \frac{\frac{hc}{k}(E_2^{"} - E_1^{"})}{\ln\left(\frac{A_1}{A_2}\right) + \ln\left(\frac{S_2(T_0)}{S_1(T_0)}\right) + \frac{hc}{k}\left(\frac{E_2^{"} - E_1^{"}}{T_0}\right)} \tag{2.26}$$

where $E_1^{"}$ and $E_2^{"}$ are the lower state energies of transitions 1 and 2, respectively. Subsequently, with the temperature now known, the mole fraction of the species can be simply inferred by the integrated spectral absorbance of any of the two lines from the equation:

$$x_{abs} = \frac{A_i}{PS_i(T)L} \tag{2.27}$$

The scanned-wavelength approach has the advantage of being able to resolve the full absorption feature. Then, by taking the ratio of the integrated areas the dependence on pressure and mole fraction is eliminated since the line strength is only a function of temperature. Also, when the entire transition is resolved the baseline can also be recovered by polynomial fitting from the sections around the probed absorption feature, and thus a third reference wavelength is no longer necessary. However, for high pressure applications such as IC engines, transition broadening and blending with neighbouring lines makes full transition recovery and curve fitting very difficult, if not impossible. Moreover, the temporal resolution of the system is limited since the scanning range is inversely proportional to the scanning rate.

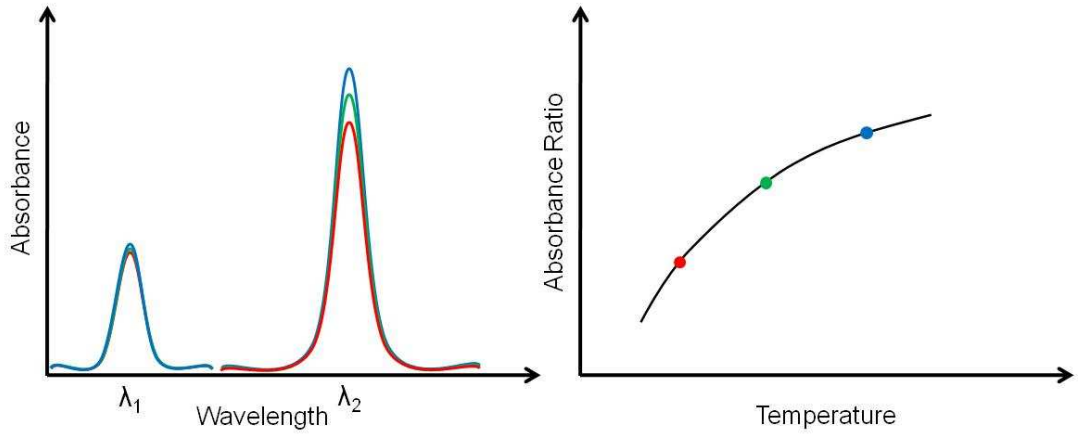

Figure 2.6 2-line thermometry illustration, where colour indicates different temperature

In the fixed-wavelength approach, usually the peak absorbances of two appropriately selected features are continuously probed [21,65]. The transitions are selected to have different temperature dependence and the absorbance ratio based on Eq. 2.3 can be expressed as:

$$R_T = \frac{\alpha_{v1}}{\alpha_{v2}} = \frac{S_1(T)\varphi_1(\nu_1)}{S_2(T)\varphi_2(\nu_2)} = \frac{\sum_{i=1}^{n} S_i(T)\varphi_i(\nu_1)}{\sum_{j=1}^{n} S_j(T)\varphi_j(\nu_2)} \tag{2.28}$$

The species mole fraction along the absorption path can then given by Eq. 2.29.

$$x_{abs} = \frac{\alpha_{v-fixed}}{PL\sum_{i=1}^{n} S_i(T)\varphi_i(\nu_1)} \tag{2.29}$$

Eq. 2.28 shows that the fixed-wavelength absorbance ratio is a function of temperature through the linestrength ratio, and function of pressure through the effects of the lineshape function [65]. The effects of these dependencies on water

absorption features are shown in Chapter 3, by simulating these lines with spectral parameters taken from HITRAN database (Figure 3.4-5). Assuming uniform temperature distribution with appropriate line-pair selection the mole fraction dependence can be eliminated [66] while pressure inside the engine can be easily measured with a pressure transducer. Also, for elevated pressures, the contributions of nearby lines at the selected wavelengths should be taken into account for system modelling. The location of the peak absorption is also shifted at high pressures and thus the simulated absorption values should be taken at a fixed-wavelength position and not at the peak of the transition. Non-uniformities in the temperature distribution can be addressed with multiple light projections and appropriate data manipulation [48,63,67].

2.5 **Summary**

The fundamental theory of Absorption Spectroscopy for gaseous chemical species is given in this Chapter. The absorption feature formation mechanism has been described with emphasis given on the rotational-vibrational IR transitions and their overtones in Near-IR. The two main absorption spectroscopy methods, namely DAS and WMS, are addressed and the physical linestrength and lineshape broadening functions are detailed. Finally the two-colour, ratiometric method for gas temperature and mole fraction measurements is also addressed.

Chapter 3
Water Vapour TDLAS System Modelling

From the discussion in Chapter 2 it is evident that for Near-IR absorption spectroscopic measurement of water vapour concentration in an IC engine at least two transitions need to be probed. This can be accomplished either with a broadband scanning source [30,68] or by using multiple fixed wavelengths resonant with appropriately selected transitions [33]. The first approach however requires a complex laser source and it is limited in terms of wavelength and temporal resolution which are both essential requirements for our application. For two-line thermometry with multiple wavelengths a multiplexing/demultiplexing scheme is required in order to combine the laser beams, interrogate the sample under test and separate them at the detection side. A number of multiplexing schemes are available such as Wavelength Division Multiplexing (WDM), Frequency Division Multiplexing (FDM) and Time Division Multiplexing (TDM). The decision upon the most suitable scheme for our measurement system will be based upon optimising performance in terms of temporal resolution, high accuracy and precision. We also aim to take full advantage of our existing low-noise HydroCarbon (HC) opto-electronic measurement system [41]. The first step before choosing the most appropriate multiplexing scheme is the selection of the water vapour transitions that will be probed.

3.1 **Line Selection Process**

Line selection is a very crucial part of the 2-line sensor design as it can significantly improve its accuracy and performance [21,66]. A number of spectral databases are available amongst which the High Resolution Transmission (HITRAN) molecular absorption database is the most commonly used. HITRAN [69] contains a large number of IR spectroscopic parameters for many small molecular species. These parameters can be used for computer simulations of the spectroscopic features of interest under various environmental conditions. The first version was compiled by the U.S. Air Force Cambridge Research Laboratories in the 1960's for atmospheric transmission simulations and since then it has been regularly updated and it is available online. HITRAN database is an extremely useful tool for IR spectroscopic absorption sensor modelling, but unfortunately it also contains errors, especially for high temperature and pressure conditions [44]. Therefore one needs to perform experimental validation of the spectroscopic properties of lines of interest before using the HITRAN database for comparative simulations. For the water vapour absorption spectrum simulations presented in this work, we used HITRAN 2004 data validated by the Stanford group and also compare the results with the 'SpectralCalc' high-resolution spectral modelling online simulator using the latest HITRAN 2008 database.

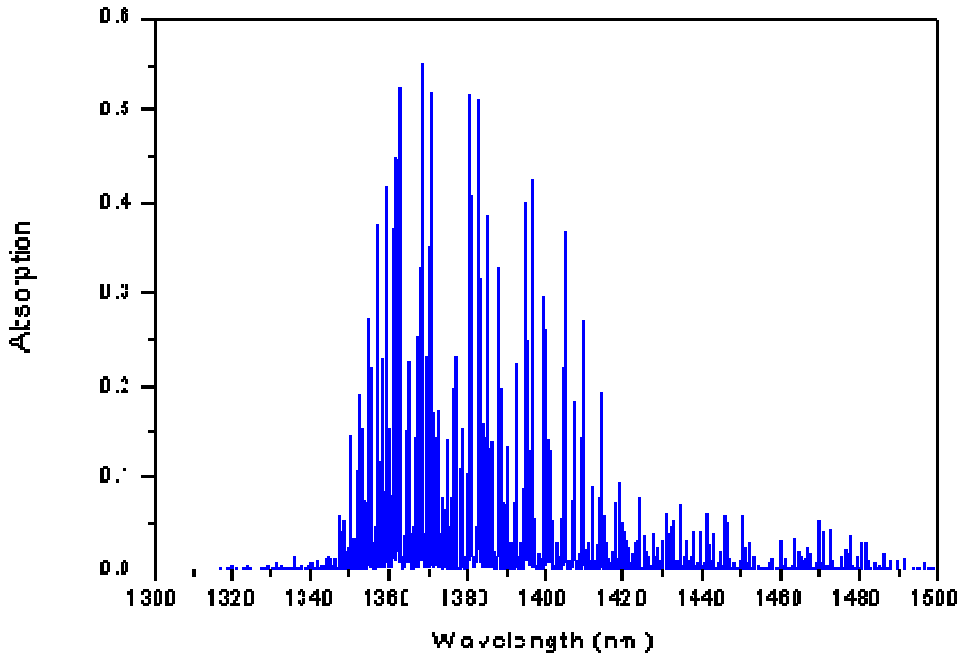

Figure 3.1 Near-IR absorption spectrum of water (10% mole fraction, path length 8 cm, 1atm, 296K)

A very large number of overtones of water vapour fundamental transitions conveniently appear in the Near-IR region (Figure 3.1). More interestingly, a few thousand rotational-vibrational overtones exist between 1350-1400 nm, many of which have been studied in the past by other research groups. Moreover, due to advances in telecommunications in the Near-IR, well developed diode lasers and fibre-optic components for this region are readily available. HITRAN contains a number of parameters the most important of which are

- vacuum wavenumber of the transition (cm-1);
- absorption line strength, Si,j (cm-1/(molecule.cm-2)) between states i and j;
- energy of the lower-energy state, E'' (cm-1);
- variation of S with temperature, T (K);
- line-shifts due to pressure;

- coefficients to characterise broadening effects due to various mechanisms, such as Doppler effects, and collisional (i.e. pressure) effects in the pure gas and in various bath gases.

By selecting suitable data from the HITRAN 2004 version we compiled a MATLAB code [Appendix A] in order to create a model of Near-IR H2O vapour spectral lines for various thermodynamic conditions that occur during intake and compression strokes of the engine cycle. The selection process for the most appropriate pair of lines for water thermometry and mole fraction measurements has to be done carefully, based on a number of criteria for optimum results [21,66] and an outline of our selection process is presented in [70]. In order to determine the most suitable line pair for water thermometry it is essential to define the likely operational conditions. The product of perfect combustion contains 14% of H2O by volume and the path length is defined by the internal diameter of the engine cylinder typically, 8cm. Based on a model for in-cylinder thermodynamic conditions of the HCCI engine, the temperature and pressure range has been calculated for the compression stroke and given in Table 1.

Pressure (atm)	T_{min} (K)	T_{max} (K)
1	296	400
5	450	650
10	500	900

Table 1 Pressure and temperature ranges relevant to water measurements in the HCCI engine cycle.

The first selection criterion addresses the minimum and maximum peak absorption levels of each line in order to ensure sufficient SNR. Thus, the selected lines in each candidate pair were required to exhibit peak absorption between 8% and 50% at any temperature and pressure within a cycle in order to give strong absorption but not attenuate the signal excessively. Minimum and maximum absorbance levels can be calculated by Eq. 2.3. The second selection criterion is that peaks should remain well resolved at high pressures where broadening effects are dominant, which eliminates lines with strong adjacent transitions. Selected transitions should also have minimum lower state energies E'' at least 350cm^{-1} [49] and their absorption ratio should be monotonic with temperature variation. Based on these criteria, 12 lines have been initially selected and are shown in Table 2. These lines have been identified previously as potentially suitable lines for TDLAS absorption studies of H_2O vapour in combustion systems [49,66] and lines 5 and 6 have been utilised previously for in-cylinder single-channel TDLAS measurements on IC engines [29,33].

Line	Nominal Wavelength (nm)	Contributing Transitions (cm^{-1})	Lower State Energies E'' (cm^{-1})
1	1350.42	7405.11	920
		7405.15	920
		7405.19	603
2	1352.48	7393.85	744
		7393.79	744
3	1355.83	7375.54	399
		7375.73	509
4	1357.15	7368.41	447
5	1388.14	7203.89	742

6	1385.12	7219.61	488
		7219.5	488
7	1404.94	7117.75	399
		7117.42	447
8	1409.51	7094.68	586
		7094.73	586
9	1414.10	7071.48	744
		7071.50	744
10	1389.02	7199.33	889
		7199.38	889
11	1391.67	7185.6	1045
12	1418.9	7047.68	920
		7047.32	885

Table 2 Properties of potential H_2O absorption lines for use in a H_2O CST system.

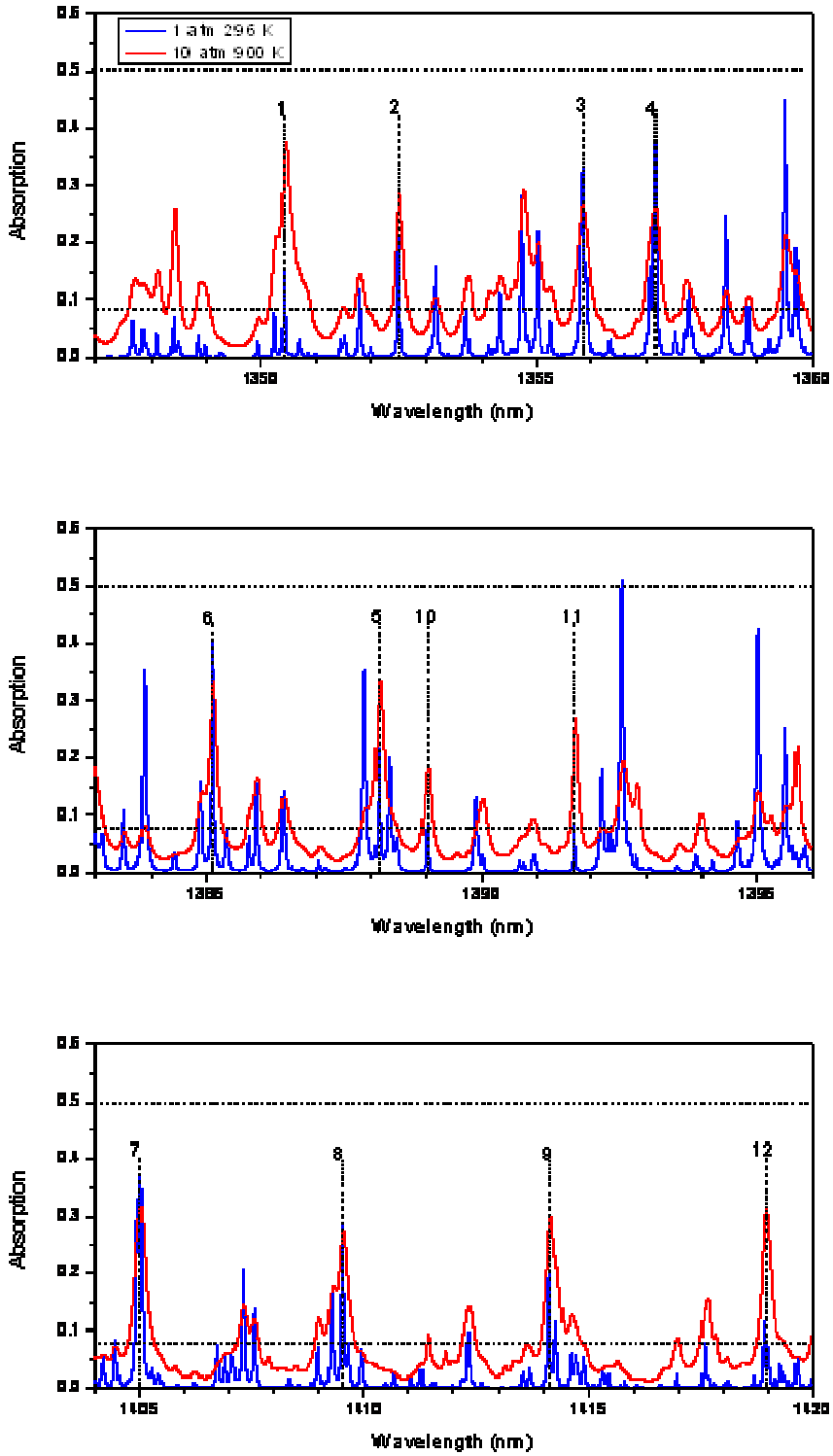

Figure 3.2 Simulated H_2O absorption spectra showing potential lines for H_2O CST in an HCCI engine. The absorption peaks are numbered according to Table 2.

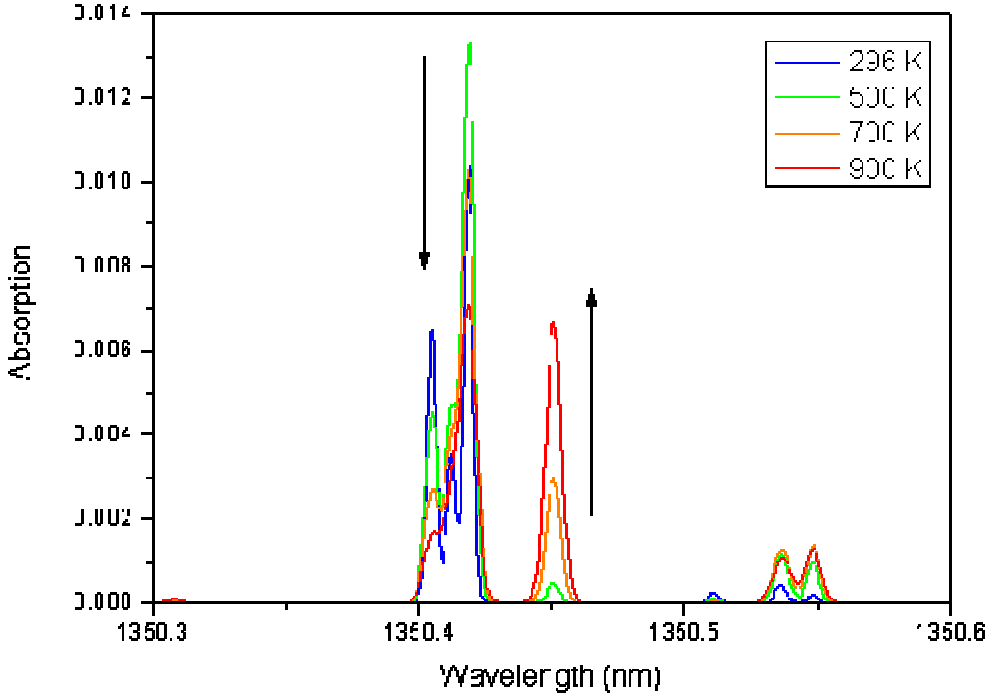

Figure 3.3 Simulation of Line 1 at 1 mbar to show contributions of underlying transitions. Arrows indicate direction of change as temperature increases in the range 500 – 900K.

Of the twelve lines selected here, the transition parameters in the HITRAN database have been experimentally verified under appropriate thermodynamic conditions for lines 1, 5 and 11 [44]. However, measurements by the Stanford group [44] in the region of line 1 have shown that the high-E'' component listed in the HITRAN 2004 database at 7404.93 cm^{-1} does not exist in reality. The non-existent transition has therefore been omitted from Table 2. This observation highlights the importance of experimental verification of any spectroscopic database for design of an accurate measurement system. In order to achieve maximum temperature sensitivity the difference between the lower state energies $\Delta E'' = E''_{high} - E''_{low}$ of the line-pair should be maximised as well [29]. High lower state lines (E''_{high}) are defined as lines with $E'' > 800$ cm^{-1}, and low lower state lines (E''_{low}) are defined as lines with $E'' < 500$ cm^{-}

[1]. So the minimum $\Delta E''$ would be 300 cm^{-1}. This yields four high E''_{high} lines (1, 10, 11 and 12) and four low E''_{low} lines (3, 4, 6 and 7). Lines 10 and 11 were later rejected since they appear to have strong interference from adjacent lines at pressures above 5 bar. From the remaining transitions, the pairs 12-4 and 1-6 appeared to have the greatest temperature sensitivity but line 12 was also rejected since it has been reported [71] that strong hydrogen peroxide interference appears during combustion at that wavelength. Thus, the most suitable line-pair for this work are lines 1 and 6 at 1350.42 nm and 1385.12 nm respectively.

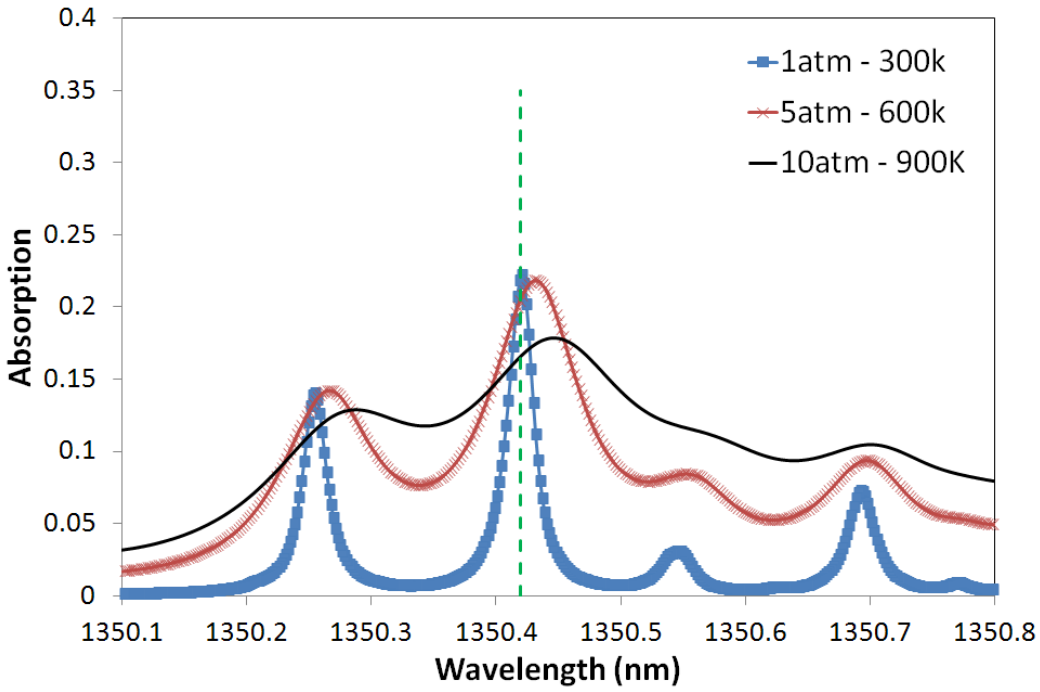

(a)

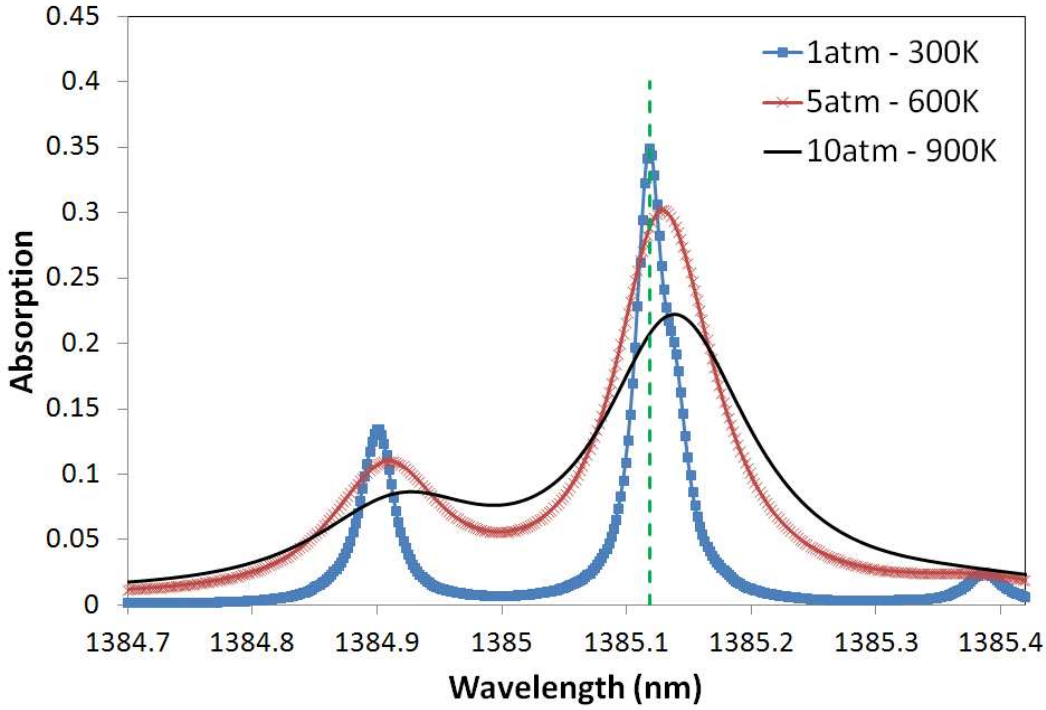

(b)

Figure 3.4 Simulated absorption spectra in the regions around the two chosen laser wavelengths (indicated by green dashed lines) at (a) 1350.42 nm and (b) 1385.12 nm, for 10% mole fraction water vapour and 8 cm path length, at a series of temperatures and pressures.

Figure 3.4 shows the simulated spectra of the selected transitions (1350.42 nm and 1385.12 nm) for fixed water vapour mole fraction and a range of temperatures and pressures as indicated in Table 1. Even though these transitions have been chosen to have minimum pressure dependence it is evident from the simulations that their peaks are shifted as pressure increases. This is a very important property when it comes to a fixed-wavelength approach for ratiometric thermometry since it can cause errors in the calculated absorption ratios. Therefore, when such an approach is being adopted one needs to be careful to calculate the ratio at a preselected fixed wavelength which does not necessarily coincide with the peak absorption of each line. Also the instantaneous in-cylinder pressure should be continuously monitored along with the recorded signal intensities.

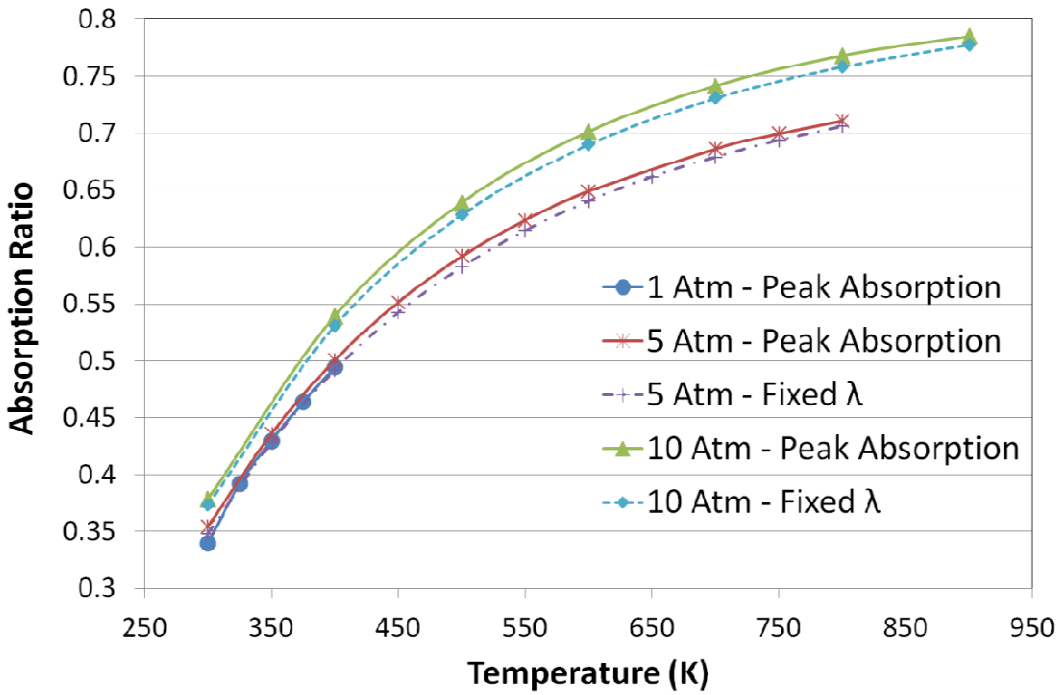

Figure 3.5 Simulated peak absorption ratio and fixed-wavelength absorption ratio of the selected lines as a function of Temperature and Pressure (1350.42 and 1385.12 nm).

Figure 3.5 shows the simulated peak absorption and fixed wavelength absorption ratios for various thermodynamic conditions for the selected line-pair. This figure indicates how the ratio of the fixed wavelength absorption only depends on temperature and pressure, and it is independent of the mole fraction variation. Thus, in an IC engine application, by monitoring the in-cylinder pressure and measuring the ratio of these two wavelengths, the chamber temperature can be estimated and subsequently the average path concentration can be calculated based on Beer-Lambert relation, as explained in Chapter 2. Also, the difference between the peak and fixed wavelength ratios at high pressures indicates the importance of keeping track of the wavelength throughout the measurement.

3.2 **Multiplexing Scheme Selection**

3.2.1 *Fixed versus Scanned Wavelength*

The first decision to be made for our system is whether a fixed or scanned wavelength measurement approach will be adopted. As has been described in Chapter 2, for narrow spectral features the scanned wavelength approach has the advantage of interrogating the entire transition and thus providing more spectral information [26]. Also the fact that the calculated integrated absorbance is directly proportional to mole fraction and linestrength further facilitates the data analysis. For an IC engine measurement, however, the wide pressure variation causes line broadening as shown in Figure 3.4 which complicates the scanning approach as well as the baseline recovery. Moreover, the essential requirement of high temporal resolution is also limited by the scanning rate of the diode-laser which is also inversely proportional to the scanning range. A fixed wavelength approach is simpler to implement and has the advantage of continuous monitoring of the selected wavelength, and the temporal resolution is only limited by the detector's response and the rate of the data acquisition system. For these reasons we decided to proceed with a fixed wavelength system for our measurements. In Chapter 2 we described how, for accurate fixed-wavelength H_2O vapour absorption ratiometric measurements, an extra non-absorbing wavelength is needed to account for the background baseline recovery. Thus the multiplexing scheme we need to implement should incorporate three beams in total, two absorption-resonant and one non-resonant. Ideally, the monitoring of all three wavelengths will be simultaneous.

3.2.2 *Wavelength Division Multiplexing (WDM)*

WDM is a commonly used scheme in telecoms and it is implemented by combining different laser beams into a single fibre with standard fibre couplers. The multiplexed colours are travelling simultaneously through the single-mode fibre before they are collimated and pitched across the sample under test. On the detection side the multiplexed beams are collected by a relatively wide core multimode fibre before they are de-multiplexed to feed in to the detectors. Typical wavelength demultiplexing approaches include free space arrayed waveguides, thin-film filters and diffraction gratings. All these methods are relatively straightforward to implement with free space optics but they require careful alignment and suffer from polarisation-dependent noise. Additionally for H_2O vapour absorption measurements the optics should also be contained in a humidity-free environment (usually by dry gas purging), which further complicates the experimental setup, especially when it comes to in-situ IC engine measurement.

3.2.3 *Time Division Multiplexing (TDM)*

An alternative scheme for combining multiple wavelengths is TDM, where the laser beams are emitted in succession for fixed time intervals. The beams are transported and pitched through the absorbing medium on the same single-mode fibre as in the WDM approach, but in this case the bulk demultiplexing optics are no longer necessary. TDM is commonly used in digital systems and it is limited by the detection bandwidth. The main drawback of TDM is that the different wavelengths are not measured simultaneously which reduces system accuracy for rapidly changing environments.

3.2.4 *Frequency Division Multiplexing (FDM)*

In modulated spectroscopy applications with multiple wavelengths, FDM is usually implemented. FDM is similar to the WDM scheme with the difference that the combined wavelengths are also intensity-modulated at different high frequencies. Then at the detection side the signals are fed to lock-in amplifiers which have been set to detect the respective frequencies. Thus no free space bulk optics are required for demultiplexing prior to the detector which is a benefit for in-situ water vapour measurements. Also, compared to TDM, the different signals are measured at the exact same time. FDM requires careful selection of the modulation frequencies for each laser in order to avoid interference of the harmonic signals of the different frequencies. To date, FDM has been strictly limited to WMS applications (see Chapter 2) since the high frequency modulation also caused wavelength modulation of the transmitted signal.

3.2.5 *Fixed-Wavelength DAS with Phase-Sensitive Detection*

As mentioned earlier, we are trying to take full advantage of the low-noise hardware system that has been developed by the Manchester group over recent years for HC fuel tomographic imaging in IC engines [42]. In that system, one laser beam was used to monitor the HC absorption at 1700 nm and a reference non-absorbing beam at 1650 nm was used to account for non-HC specific effects. An FDM was scheme implemented, where the two wavelengths were modulated at 300 kHz and 500 kHz respectively, and a dual-frequency lock-in amplifier was used to separate the two signals on the detection side. The 1700 nm HC absorption overtone facilitated these measurements since this broad transition [39,72] allows direct detection of the modulated signal. In the case of water spectroscopy however, the widely varying

nature of the selected narrow transitions dictates an alternative modulation scheme in order to ensure fixed wavelength operation. Additionally, as has been described above, an extra reference beam should be incorporated in to the system. Thus both the modulation and the multiplexing schemes have to be changed, relative to the system of Wright et al. 2010 [42].

In order to address the multiplexing issue we decided to implement TDM between the two resonant wavelengths which will be modulated successively for small time intervals with the same modulation frequency. In this way both absorbed wavelength signals are recovered by the same lock-in amplifier and they can be easily distinguished with a TTL clock signal. The reference signal will be modulated by the second frequency and continuously monitored by the lock-in detector along with the TDM signal. In this way, it is possible to fully utilise low noise detection system of Wright et al. 2010 and perform the necessary water measurements. However, fixed wavelength operation is awkward to implement, since by using the traditional method of directly driving the DFB lasers with a modulating signal unavoidably introduces wavelength modulation too. Ideally, we need an optical intensity modulation scheme which does not alter the wavelength of the transmitted signal. In this work we developed a novel scheme where we use Semiconductor Optical Amplifiers (SOAs) in order to perform both TDM optical switching and wavelength insensitive modulation of the optical signals.

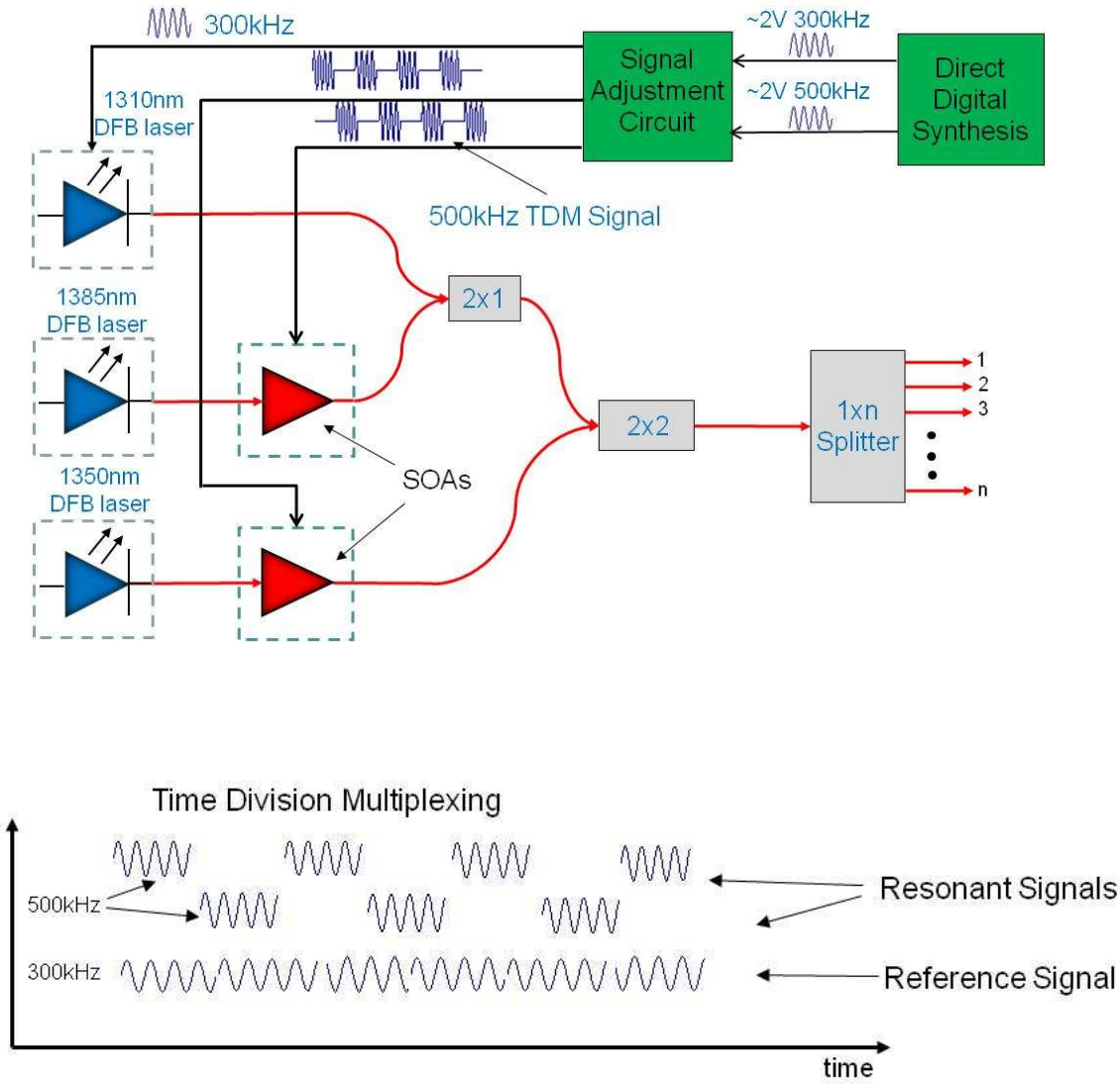

Figure 3.6 Fixed-Wavelength Time Division Multiplexing with SOAs

Figure 3.6 shows the proposed multiplexing/modulation scheme designed for this work. The selected absorption transitions at 1350.42 nm and 1385.12 nm are multiplexed with a reference non-absorbing wavelength at 1310 nm region which has been selected to monitor the non-absorption specific attenuation such as beam steering, back reflections and soot particles attenuation. Three ultra narrow beam (~0.01 nm FWHM) Distributed Feedback Lasers (DFB) designed to emit at the selected wavelengths will be used in this experiment. The 1310 nm reference laser can be directly modulated with a continuous 500 kHz signal since broadening effects

are not an issue for the reference beam. The resonant DFB lasers are driven with a constant dc current and temperature which are chosen to tune the emitted beam on the selected wavelengths. The optical outputs of the DFB lasers are then coupled to the inputs of the SOAs which are driven with a TDM modulating signal. In contrast to DFB lasers SOAs can modulate the intensity optical beam without changing the wavelength. Also they can operate as optical switches with appropriate TDM driving and provide amplification to improve the total power budget of the system. An analytical description and characterisation of the SOAs is given in Chapter 4. A PCB circuit (Signal Adjustment Circuit) has been designed and built to generate the appropriate modulating signal by regulating the outputs of the DDS circuit as it is shown in Figure 3.6. An analytical description of this circuit is given in the following section. The three modulated signals are then combined with an optical coupler on a single-mode fibre before split and pitched across the absorbing medium.

3.3 Signal Adjustment Circuit

Optimum high-frequency modulation conditions for the combination of the DFB laser and the two SOAs prior to any measurement are unknown. It is highly desirable to have some flexibility in terms of modulation amplitude and dc offset of the driving currents. The two sinusoid modulation (300 and 500 kHz) signals generated by the IMAGER DDS system have very low noise and harmonic content [41] but they have fixed amplitude and dc offset. Thus, a signal adjustment circuit is required to manipulate appropriately the driving signals for the LD controllers in order to achieve the best possible TDM operation. The two SOAs are then controlled by alternating 500 kHz sinusoidal pulses. The resulting post lock-in detection signal appears as a square-wave pulse with the two levels corresponding to each

wavelength. An infinite number of harmonics are contained in this square-wave signal which subsequently passes through a 50 kHz cut-off, low-pass filter present on the detection circuit board after the lock-in amplifier. Therefore the switching frequency between the two SOAs can be up to 2.5 kHz in order to allow an adequate number of higher order harmonics to pass through the low-pass filter. The reference 1310 nm laser diode can be directly modulated with the 300 kHz sinusoid from the IMAGER DDS system since the wavelength stability is not critical in this case, and it is continuously monitored through the second channel of the lock-in circuit. A Signal Adjustment Circuit printed circuit board (PCB) has been designed and built in order to implement the optical switching functionality as well as some signal modulation amplitude and dc offset gain adjustment for optimum signal reception.

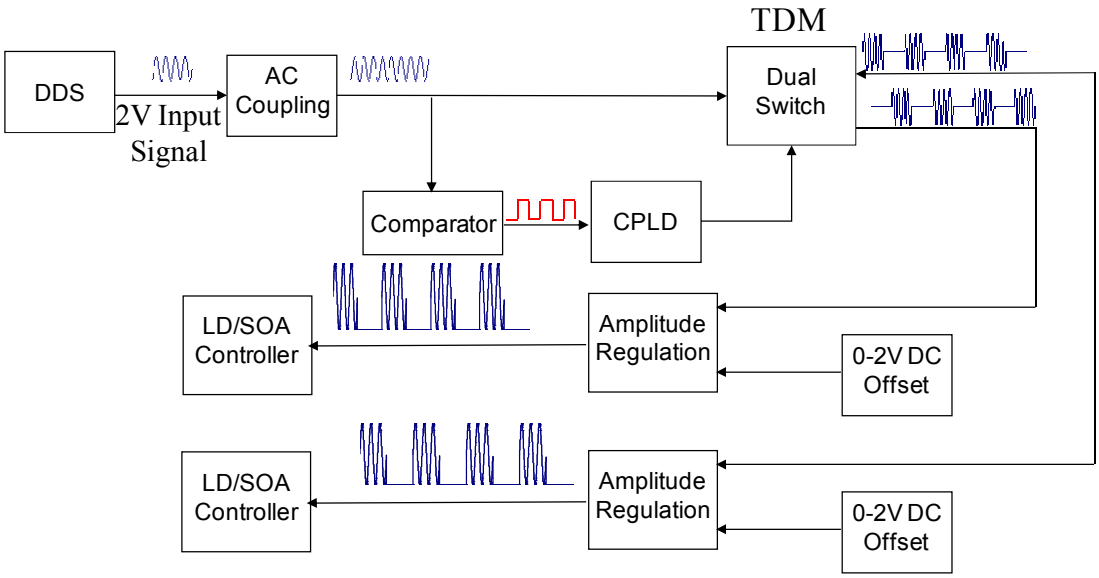

Figure 3.7 Signal Adjustment Circuit Block Diagram

A block diagram of the Signal Adjustment Circuit for the TDM functionality is shown in Figure 3.7. The ~2V, 500 kHz sinusoid signal from the DDS is filtered by a high-pass filter to remove any residual dc components and then enters a zero

crossing comparator. A ±5V LT1016 ultra-fast 10 ns comparator is used to generate the necessary clock signal for the switching operation. The comparator produces a digital signal which alternates between 0 and 1 every time the input signal crosses the zero level. Thus it produces a square pulse output signal with has the same frequency as the sinusoid input and it can be used as a clock signal in the circuit. However if the input signal is noisy and fluctuates around the reference voltage (0 Volts), this causes the output of the comparator to change state rapidly. In order to make the comparator less susceptible to noise a technique called hysteresis [73] is implemented. This technique incorporates positive feedback and it is basically changing the switching reference levels for the output to change state. This means that the reference level for switching to high output level is above zero, and for the output to change to the low level the reference level is below zero. In our case the hysteresis levels are adjusted to +0.1 and -0.1 Volts for transition to high and low levels respectively.

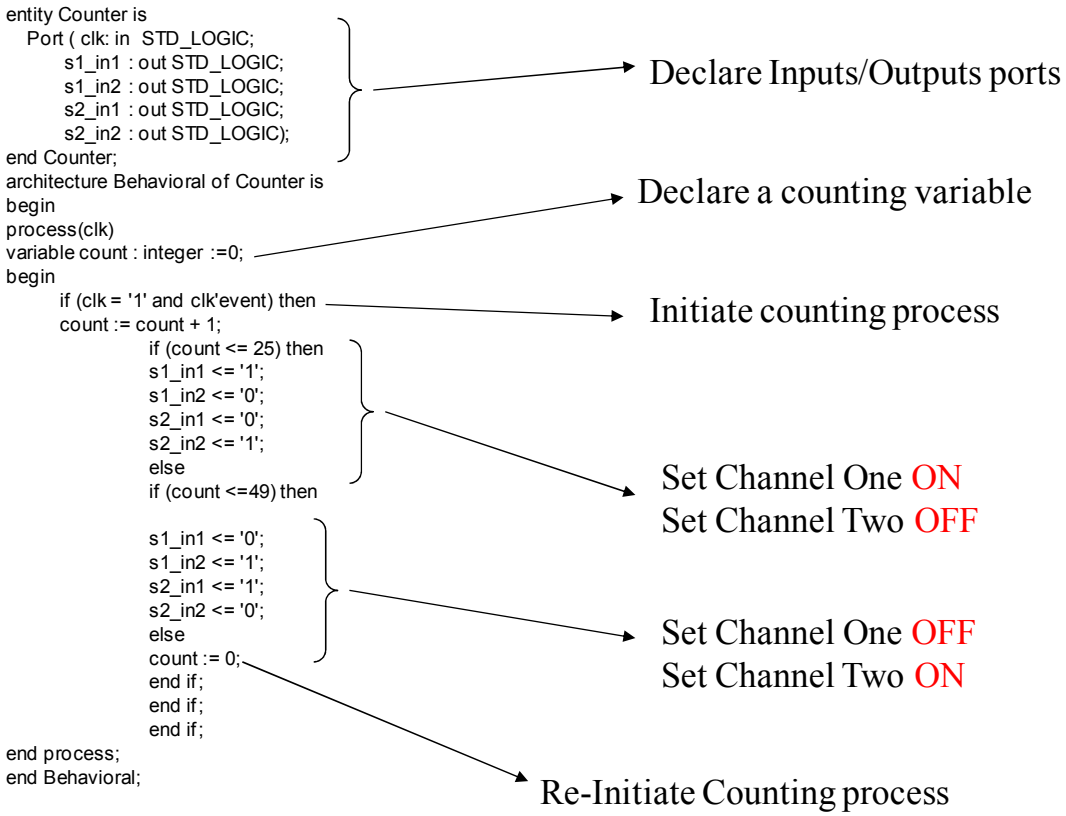

Figure 3.8 CPLD Code for switching Operation

The 500 kHz square pulse comparator output is used as a clock signal for a Complex Programmable Logic Device (CPLD). The CPLD (Xilinx XC9572) is incorporated into the PCB and it is programmed to operate as a simple counter logic device. The code is written in VHDL programming language and is given in Figure 3.8. The counter is counting the pulses from the square pulse input signal and then the CPLD produces two digital outputs which alternate between 0 and 1 for time intervals defined in the code. For example for 2.5 kHz switching frequency, each output should be ON for 200 μsec. Given that the duration of each pulse of the 500 kHz clock signal is 1 μsec, the two outputs must change their state every 100 counts (each count is 2 μsec). The two outputs of the CPLD are used to control two switches which are fed with the IMAGER DDS 500 kHz sinusoid. Therefore, the two outputs

of the two switches will give the alternating high frequency signal which is required for the TDM functionality of the SOAs. Furthermore, the PCB incorporates a number of Operational Amplifiers (Op Amp) stages for buffering the electric signals and regulating the amplitude and dc levels with mechanical potentiometers.

In order to accurately select the passive components (resistors, capacitors, inductors) and active components (transistors, Op Amps, ICs, voltage regulators) for the circuit, a simulation platform has been used (Multisim v11). A number of different components have been tested to optimise the behaviour of the circuit and to achieve the minimum noise levels and electromagnetic interference. A part of the simulation diagram is shown in Figure 3.9. The comparator operation has been simulated separately and in this diagram it has been replaced by a simple square pulse source. The low-capacitance dual switch (Analogue Devices ADG1221) outputs are filtered to remove any dc components and they enter a two stage Op Amp circuit. The first stage consists of a precision, rail-to-rail, wide signal bandwidth Op Amp (AD8606) with very low offset voltage and current noise, in negative feedback configuration. A voltage divider circuit with a precision rotating potentiometer is used to control the gain of the Op Amp. The second stage consists of a high speed Op Amp (LT1364) with very high slew rate, which is also in negative feedback configuration. This high speed Op Amp was chosen in order to assure rapid switching functionality and minimum transition noise. Another trimming potentiometer is used to control the amount of gain and therefore the amplitude of the ac signal at the output. An identical two stage Op Amp circuit is used to adjust the signal level of the continuous 300kHz sinusoid waveform used to modulate the reference wavelength.

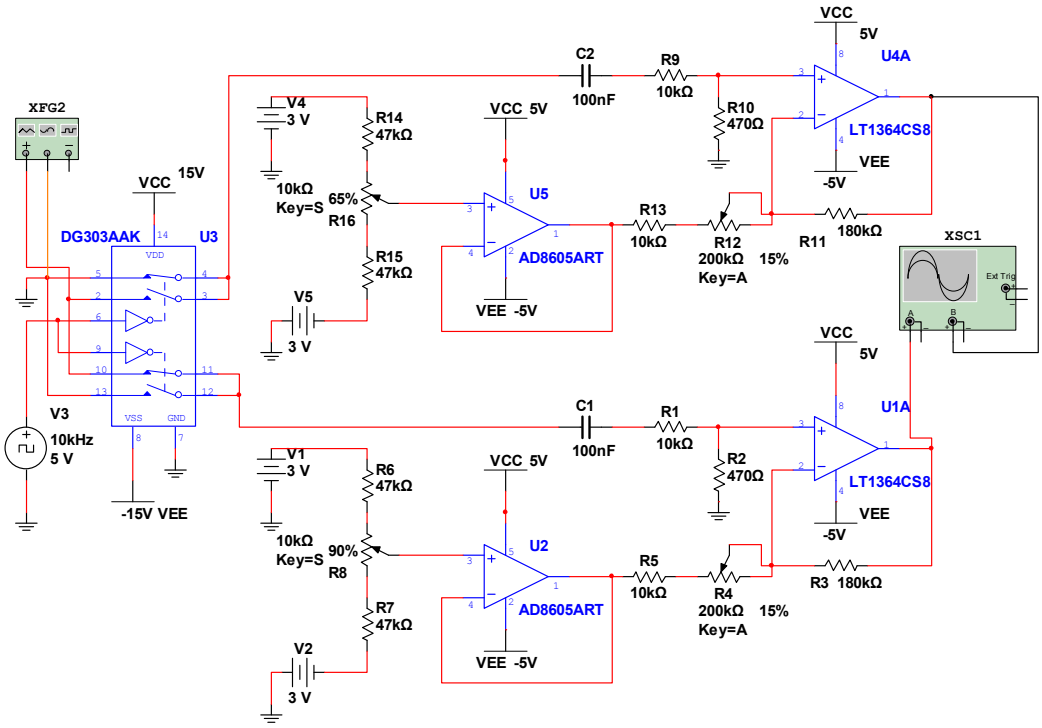

Figure 3.9 Signal Adjustment Circuit Simulation

The simulation results for the two TDM channels are shown in Figure 3.10. The Laser Diode Driver (Wavelength Electronics LDTC 2/2E) requires a 0-2V signal which determines the amount of current that is delivered to the amplifier. The adjustable control circuit described here has been designed such that the total output always resides between 0 and 2 Volts. This flexibility is necessary since the exact optimum setpoints for the control signals are unknown and will depend upon optical input power and the saturation power/gain characteristics of the SOAs. The simulation results indicate excellent switching operation with very low transition noise.

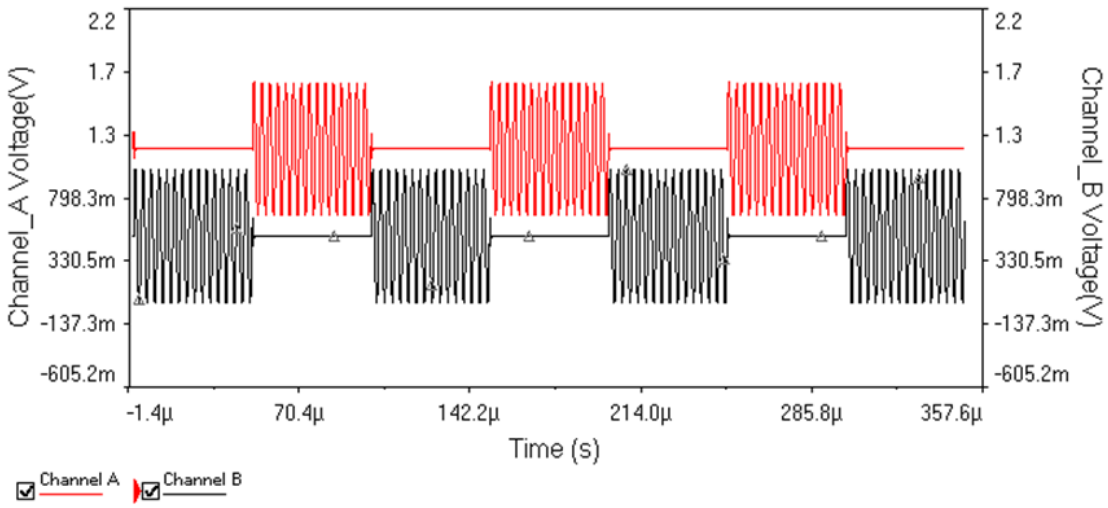

Figure 3.10 Simulated TDM Signals

Figure 3.11 shows the final PCB layout as it has been built and populated. This is a four-layer PCB with the digital components placed on a separate section on the bottom right side of the board in order to minimise electromagnetic interference from the analogue parts. BNC connectors have been placed for high frequency signals inputs from the DDS and Double-Pin connectors as outputs to the Laser Diode controllers. Three voltage regulators have been included; two for the analogue parts with ±5 and ±3 Volts constant supply and one ±5 Volts for the digital components supply.

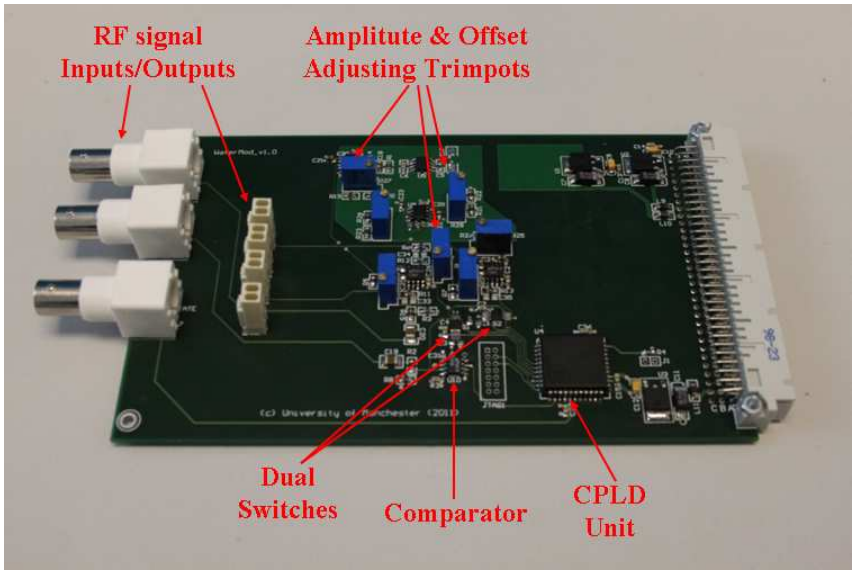

Figure 3.11 Signal Adjustment Circuit PCB Layout

The circuit switching and signal level adjustment functionality has been initially tested with a GW Instek SFG-2100 function generator and a Tektronix DPO2000 Digital Oscilloscope. A 2V 500 kHz signal has been applied to the input and the two TDM outputs were probed on the oscilloscope. The results for 10 kHz (100 μsec pulse duration) switching are shown in Figure 3.12. There is a very good matching between the test and the simulation results. Signal level adjustment was excellent with a high degree of precision. The trimmer pots have been intentionally chosen to have a large number of turns for optimum precision. However, it appears that the switching between the TDM signals does not coincide ideally with the zero crossing. This is probably because of the time delay in the switches since the CPLD propagation constant is in the order of picoseconds, but it does not have any significant effects for the proposed application.

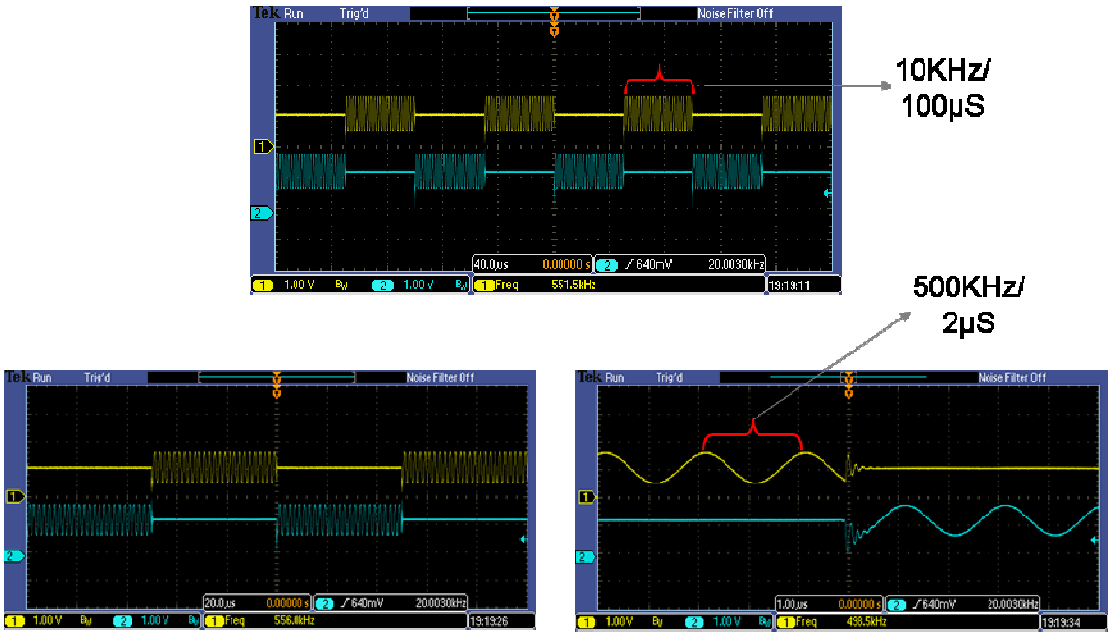

Figure 3.12 PCB Signal Adjustment and Switching Tests

3.4 **Summary**

In this chapter the architecture of the dual-wavelength ratiometric water vapour measurement system is being addressed. The line selection process of suitable Near-IR absorption features from spectral databases is detailed, and the selected lines are simulated for the predicted in-cylinder thermodynamic conditions. Various multiplexing options are described, and a fixed-wavelength TDM scheme with high-frequency intensity modulation for phase-sensitive detection is adopted. The general structural design and the various optoelectronic components of the measurement scheme are given, and signal adjustment circuit for appropriate signal manipulation has been developed and tested.

Chapter 4
External Intensity Modulation With Semiconductor Optical Amplifiers

A key element in the newly proposed scheme detailed in Chapter 3 is the SOAs which have been chosen as wavelength-insensitive intensity modulators and optical switches. By tuning the wavelength of each diode-laser to the selected spectral transition and modulating the intensity of the beam with a SOA we can achieve sensitive lock-in detection and avoid complicated wavelength scanning. In this chapter, a brief theoretical description of the SOAs is presented along with a thorough characterisation concerning the properties of interest of the SOAs for the proposed application. These include broadband gain profile, wavelength stability, insertion loss, optical switching, intensity modulation and how this affects the fixed-wavelength operation.

4.1 Semiconductor Optical Amplifiers theory

Semiconductor Optical Amplifiers (SOAs) have been widely used in the Near-IR by the telecommunications industry as an alternative to doped-fibre amplifiers such as Erbium-Doped Fibre Amplifiers (EDFAs) [74,75,76]. SOAs have one optical input and one output and can potentially provide amplification to the power of an incident optical signal. They have the same gain mechanism as common diode lasers and they can generate optical amplification via stimulated emission. Their main difference with respect to diode lasers is that in the front and rear end, SOAs have anti-

reflection coatings instead of the optical feedback mechanism (mirrors). Thus they cannot generate coherent light themselves. An electrical pump (or drive) current typically 20-300 mA, is used to create the necessary population inversion for the amplification to take place. SOAs are widely used in telecoms and for signal processing applications and are commercially available in 14 pin-butterfly, sealed, fibre-coupled packages with a temperature controller and a thermistor for temperature monitoring.

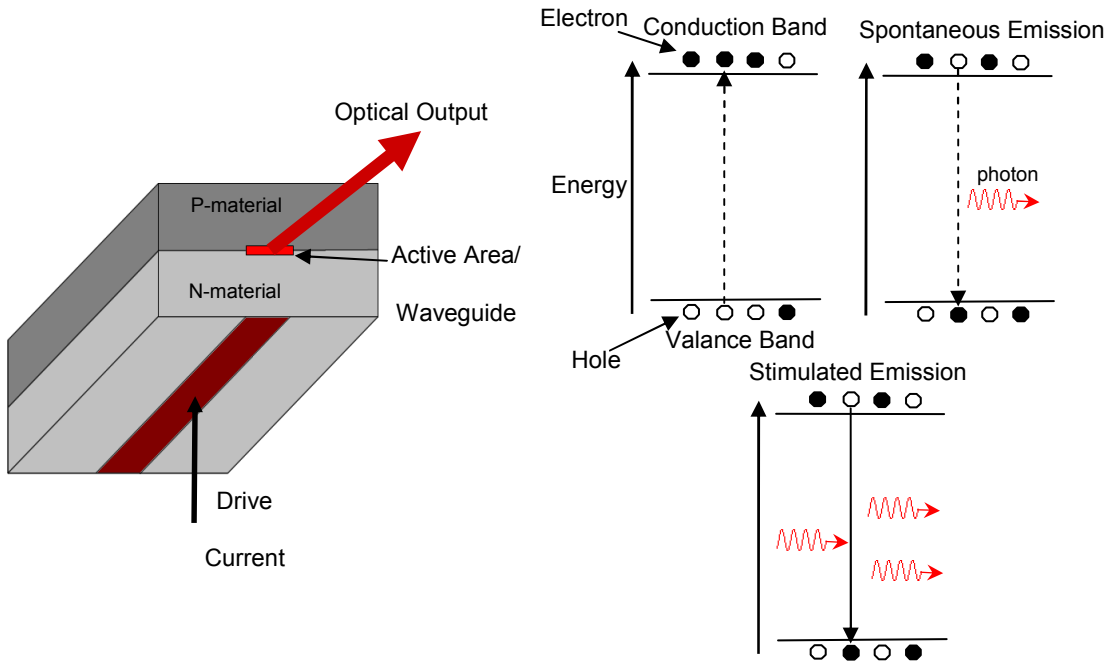

Figure 4.1 Basic structure and fundamental principles of a Semiconductor Optical Amplifier

Figure 4.1 shows the basic structure of a SOA and the fundamental principle of laser diodes [74]. The incoming optical signal is confined and transmitted with a waveguide through the gain medium which is called the active area (approx 1 mm length). Electrons (or carriers) in the active area are excited by the injection current to a high energy level (conduction band). When a carrier drops spontaneously to a lower energy state (valence band) a photon is released. This is called spontaneous

emission and it is generally an unwanted effect. In order to achieve stimulated recombination (emission) an incoming photon with suitable energy is required. This photon causes a carrier to drop to a lower energy state and a photon of the same phase and frequency as the incident one to be released. In this way, the process induces coherent amplification of the incident light and it is called stimulated emission. The degree of amplification is highly dependent on the input power level (<30 dB). For high input powers, gain saturation occurs and the SOA exhibits non-linear behaviour.

The main advantages of SOAs compared to other optical amplifiers is their compact size, low cost, low power consumption (<1W), high gain (up to 30 dB) and, with 50 – 60 nm 3 dB gain bandwidth, they can be designed to cover the entire 1300 nm and 1550 nm transmission windows used in telecoms. Also, they can be easily integrated with state-of-the-art fibre optics and opto-electronic equipment. Most of their applications are in optical communications where SOAs are commonly used in the NIR as power boosters, preamplifiers or in-line amplifiers. Their broadband optical spectrum makes them appropriate for simultaneous amplification of many multiplexed optical channels of different wavelengths (ie DWDM systems). Apart from amplification, SOAs are also used for optical signal processing applications such as wavelength conversion and optical switching, due to their strong non-linear properties under heavy saturation conditions, such as cross-gain/phase modulation and four-wave mixing [77,78]. Finally, another important property of SOAs is their very low carrier lifetime, in the order of nanoseconds, which means the carrier density changes rapidly, and thus ultra fast (tens of GHz) optical switching and modulation can be achieved.

4.2 SOA Characterisation

The properties of a commercially available SOA and its suitability for the intended application have been tested with a series of experimental tests. Functionality in terms of amplification, optical switching, intensity modulation, insertion loss and wavelength broadening/shift has been thoroughly examined. For the following experiments we have used a S-band SOA supplied by Amphotonix Ltd (SOA-08-26-N-13R-FA) and the three tunable DFB InGaAsP diode-lasers (NEL NLK15BE) which were custom made for the two selected absorbed wavelengths at 1350 and 1385nm and the non-absorbing reference wavelength at 1310 nm.

4.2.1 *Broadband Amplification*

In the first part of these tests we investigate efficiency of the SOA in terms of optical gain/output for the specific wavelengths of our interest (1310, 1350 and 1385 nm). The configuration shown in Figure 4.2 was used to examine the output power of an SOA compared to the input power. The optical input power level was adjusted by a Thorlabs VOA50-APC - SM broadband variable optical attenuator (VOA) and the optical peak output power measured with an Ando AQ-6315A Optical Spectrum Analyser (OSA). The DFB lasers were driven with a 110 mA constant dc current and the SOA was driven with a 200 mA dc current. It is important to note here that the SOAs used in these experiments have been designed for optimum performance around 1310 nm. The wavelength gain profile of the amplifier can be obtained with a constant (i.e. 200 mA) driving current and without optical input. As it shown in Figure 4.3, the SOA under test has about 50 nm 3 dB gain from 1285-1335 nm.

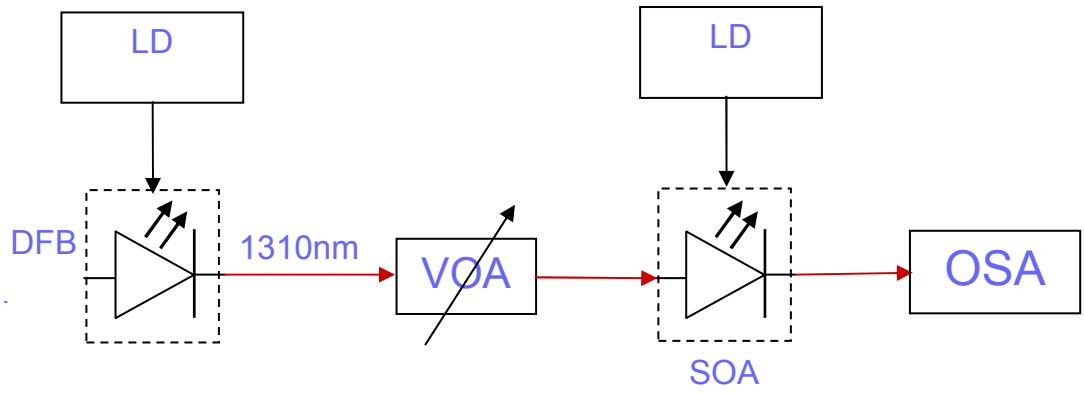

Figure 4.2 Optical Power Measurement Configuration

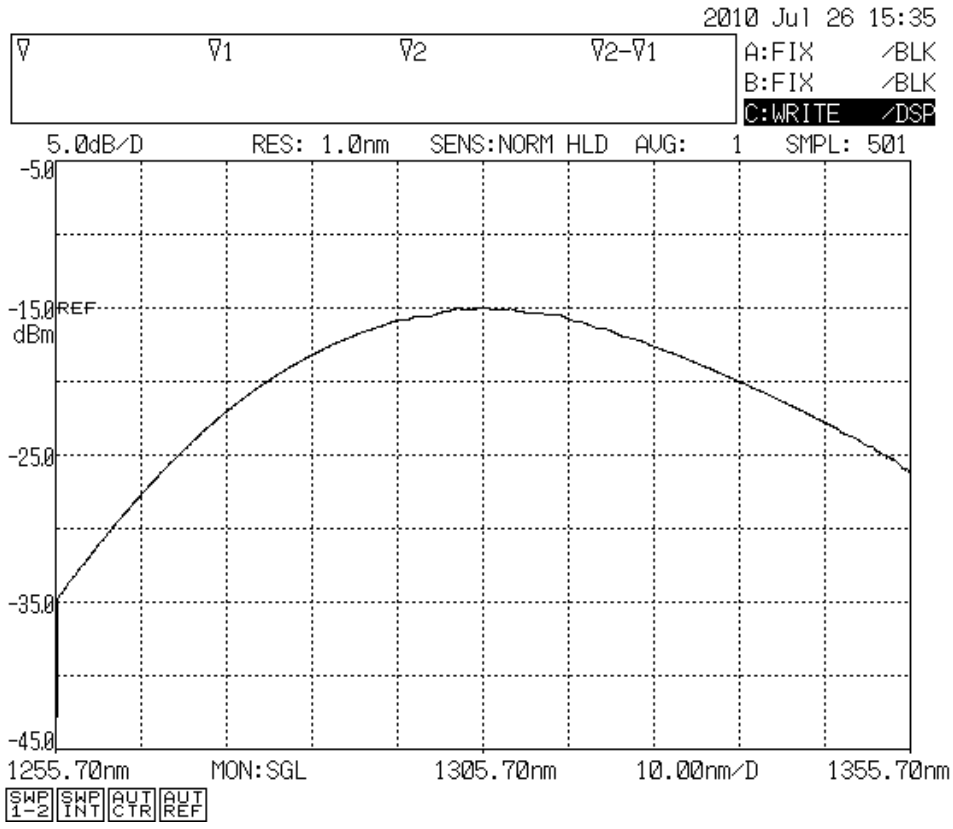

Figure 4.3 Wavelength spectrum of the SOA gain.

Figure 4.4 shows how the output power of the amplifier varies with the input for the three tested wavelengths, and Figure 4.5 shows the corresponding gain. It is clear from these charts that the input signal is being amplified for all the three wavelengths throughout the 1310-1385 nm wavelength range. However it is also noticeable that the gain characteristics of the same SOA are not the same as the wavelength

changes. At 1310 nm we have the typical SOA response where the gain is very high for low powers and gradually decreases as the input power increases above 2 mW. This is due to an inherent property of the SOAs which is called gain saturation [74,79] and it refers to the depletion of the carriers in the active region when input power increases. At 1350nm, with low incident power, the gain is about 7 dB lower than the 1310 nm case, as expected, but the difference is reduced dramatically as the input power increases above 2 mW. This is mainly due to the saturation power of the SOA (i.e. amplifier output power at which the gain is 3 dB bellow the small-signal gain), which tends to decrease at longer wavelengths. The gain response becomes irregular and more linear in the 1385 nm case, which is well outside the 3 dB gain region.

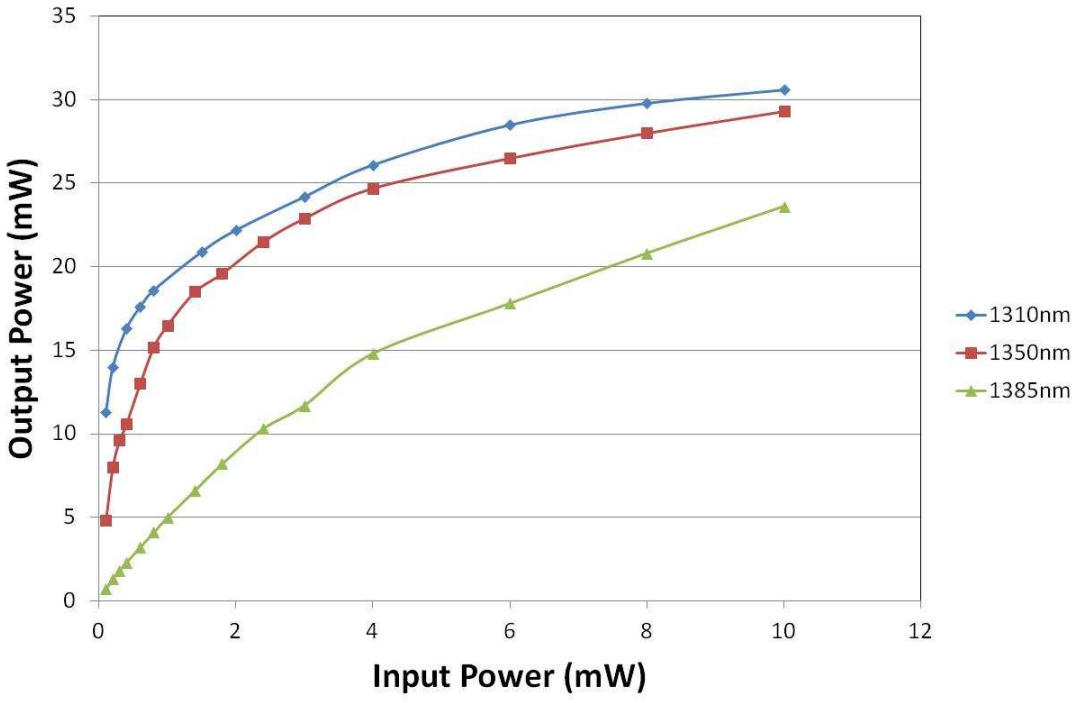

Figure 4.4 Optical output power of the SOA versus optical input at the three selected wavelengths

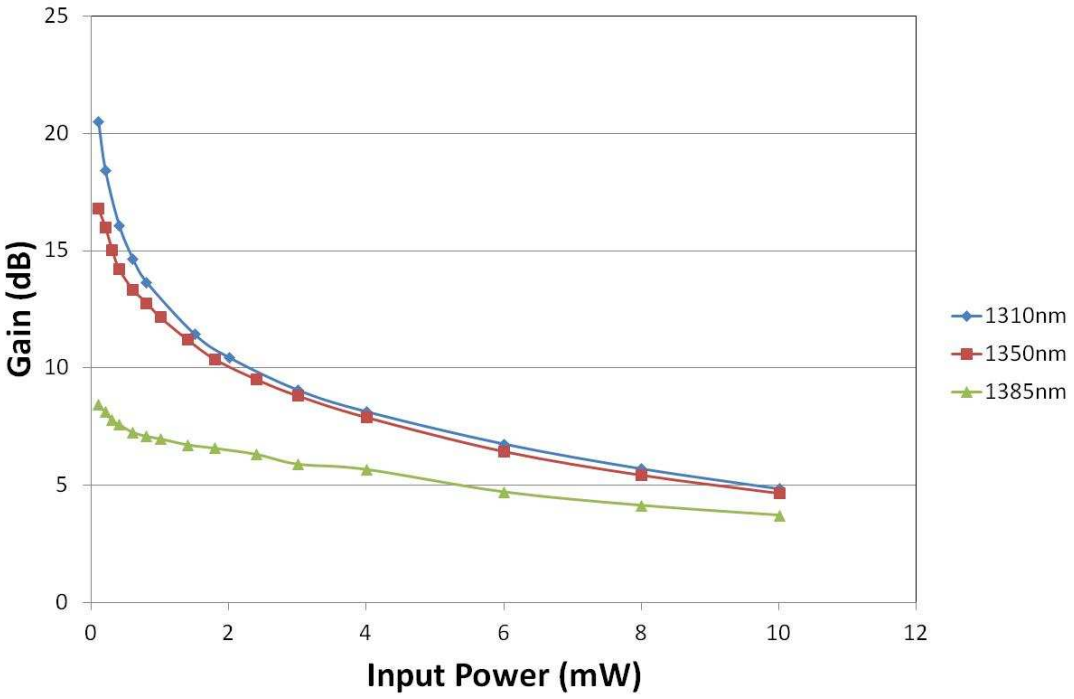

Figure 4.5 Optical Gain of the SOA at the three wavelengths as derived from Figure 4.4

Figure 4.6 shows the wavelength spectrum of the 1310 nm DFB laser and the amplified signal as it is captured by the Ando OSA. The first caption shows the DFB laser beam spectrum which is very narrow (~0.1 nm at FWHM), and in c) the spectrum of the amplified DFB output. As we can see, although the SOA has a very broad spectrum (Figure 4.3), when the ultra narrow DFB output (~0.01 nm) is used as an input, the SOA produces an amplified replica of the input at the exact same wavelength and with the same width. The above gain test results indicate that even though the commercial SOA used here is not designed for the selected wavelengths, it still can provide amplification even in the extreme case of 1385 nm, and thus it can potentially improve the power budget of our multi-wavelength system.

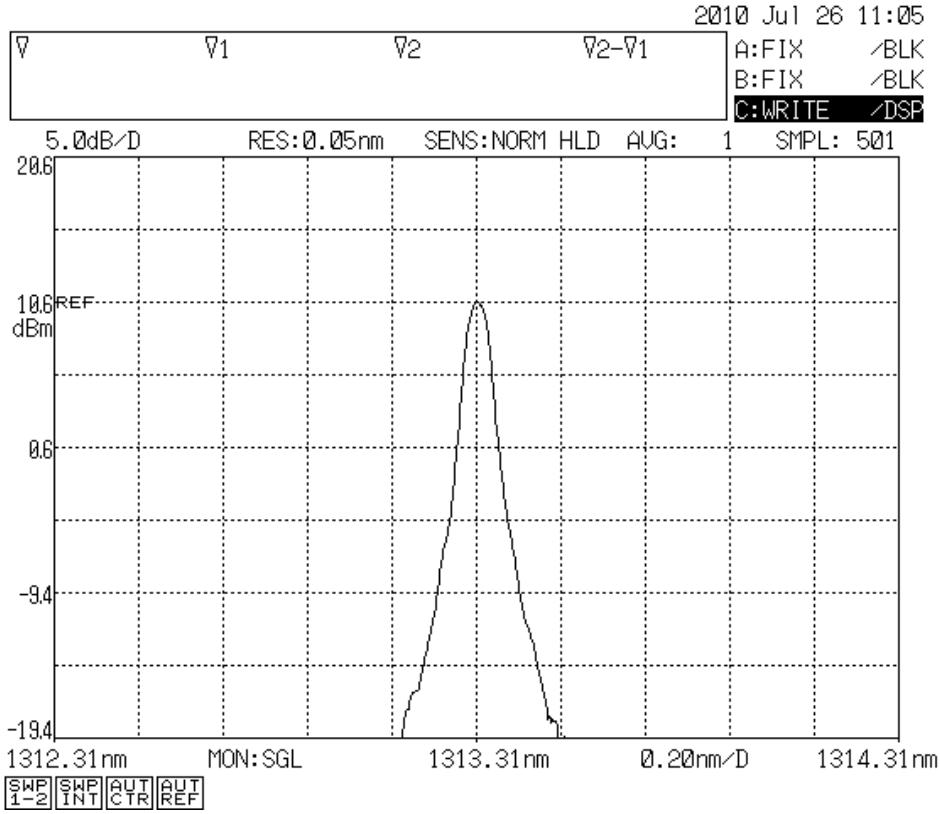

(a)

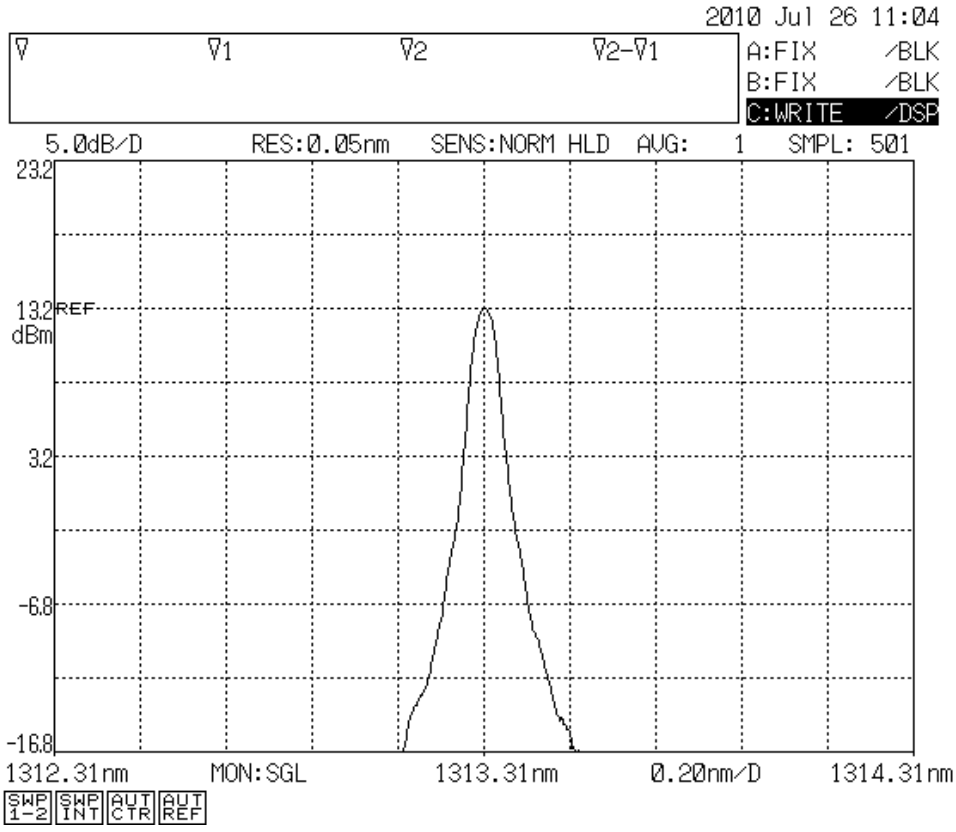

Figure 4.6 Optical Spectra of (a) DFB laser, and (b) amplified DFB laser output

4.2.2 *Wavelength Stability*

As highlighted previously, the Near-IR water absorption overtones are quite narrow at low pressure and temperature conditions, about 0.1 nm FWHM at 1 atm and 300 K for 10% mole fraction (Figure 4.7) and also very sensitive to environmental variations. Any wavelength fluctuations of the interrogating light beam can have significant effects on the measured transmitted signal power. Thus, the wavelength stability of the light beam projected into the sample is very critical especially for the fixed-wavelength scheme proposed here. For the purposes of validating our experimental apparatus a number of tests were performed to investigate the wavelength stability of the lasers and amplifiers. For these tests we used a Bristol 521 Wavelength Meter (Bristol Instruments Inc. 585-924-2620) was used, which has 0.01 nm wavelength accuracy at 1000 nm and 10 Hz measurement rate.

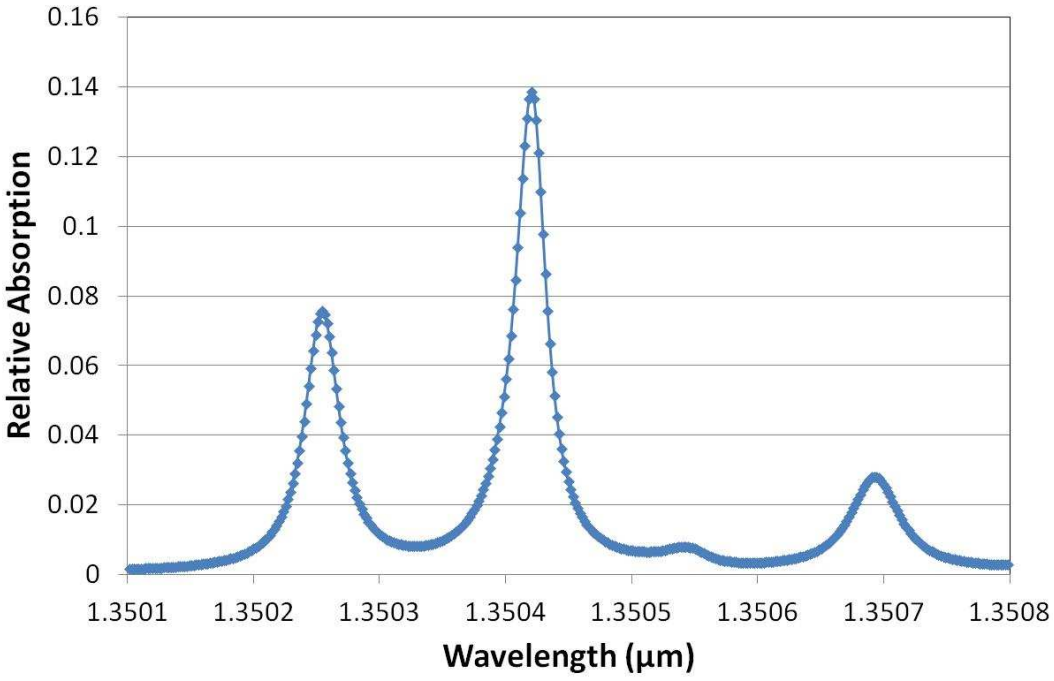

a)

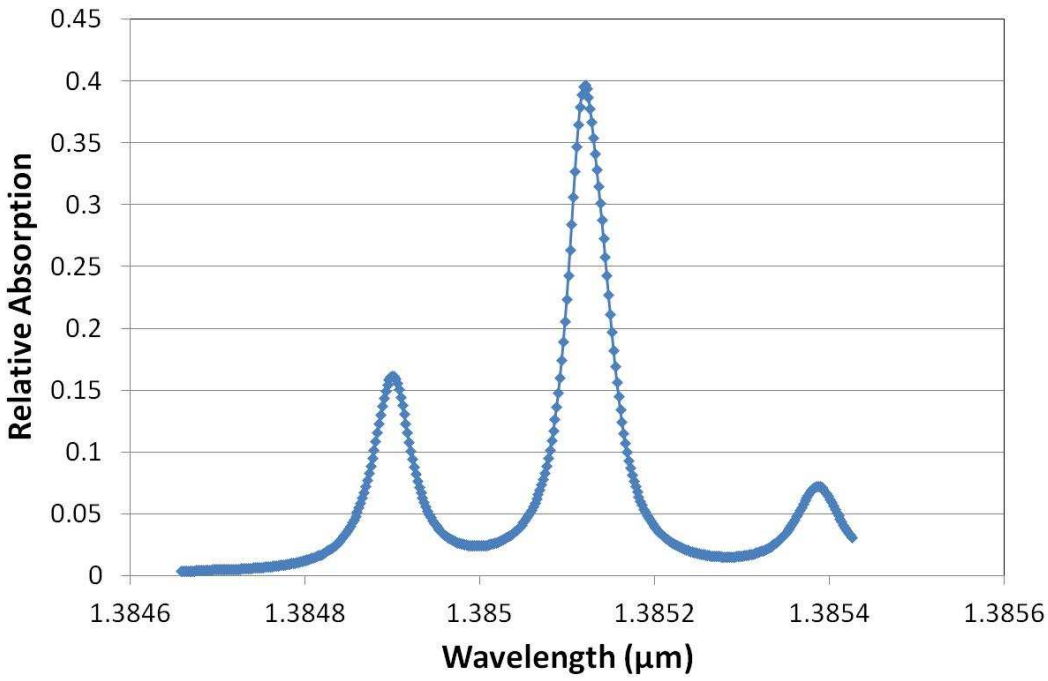

b)

Figure 4.7 Simulated selected water absorption lines for 1% mole fraction, 1atm, 300K and 8cm path length at a) 1350nm and b) 1385nm

The experimental setup shown in Figure 4.8 a) was used to track changes of the wavelength of the 1313 nm DFB laser driven with a constant current of 90 mA. Figure 4.8 b) shows the wavelength varies with time. After a 20 minutes continuous run, the standard deviation of the signal is calculated to be 0.002424 nm about the centre wavelength, which is much smaller than 0.1 nm spectral width of the water absorption features, and therefore acceptable for the measurement system. The same experiment was repeated with a SOA in line after the DFB laser, yielding the data shown in Figure 4.9. The SOA is driven with a 120 mA constant dc current and amplifies the optical signal. The insertion of the SOA does not have any significant effect on the wavelength stability giving a standard deviation of 0.002525 nm after 20 minutes of continuous run. If further wavelength stability is required this can be done with more precise temperature control on the diode laser.

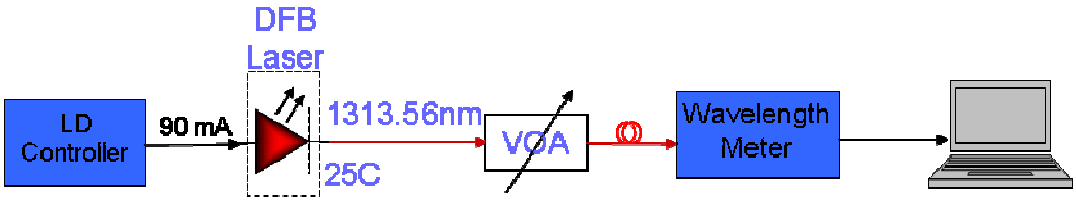

(a)

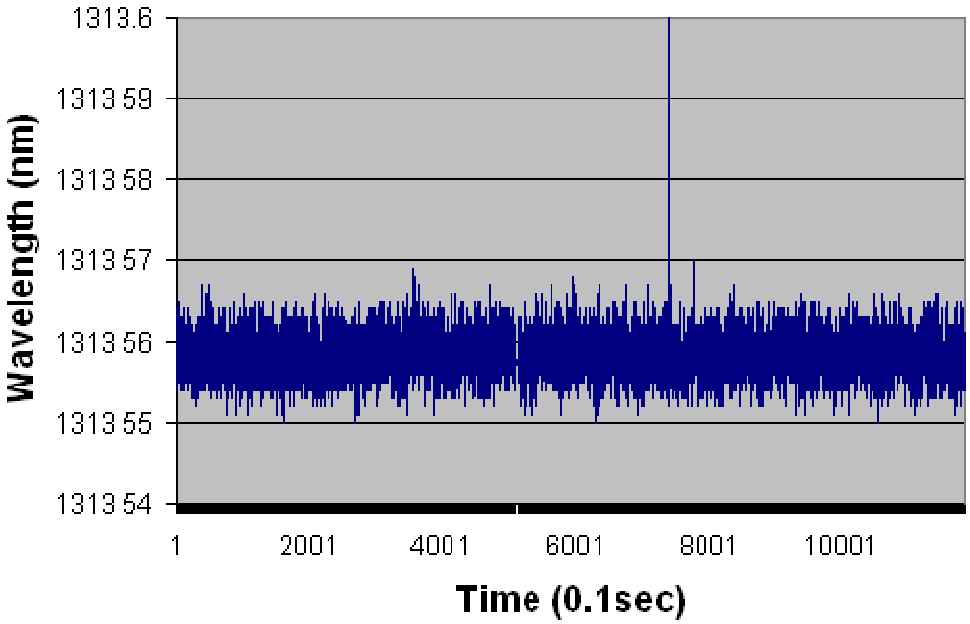

(b)

Figure 4.8 (a) Experimental setup and (b) measured wavelength as a function of time for the standalone DFB laser output

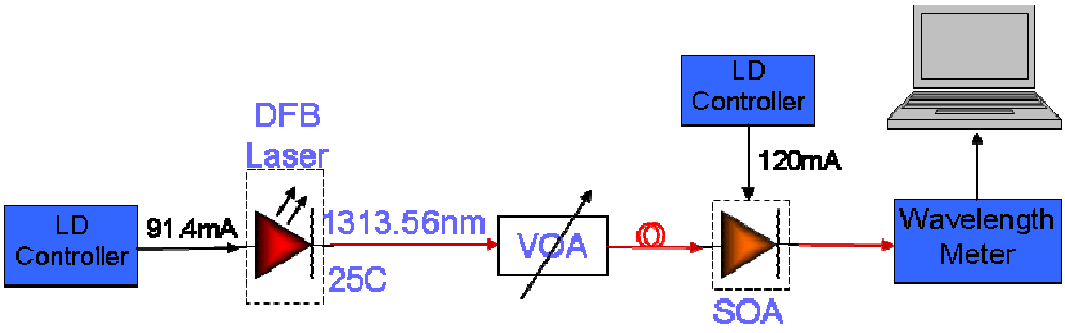

(a)

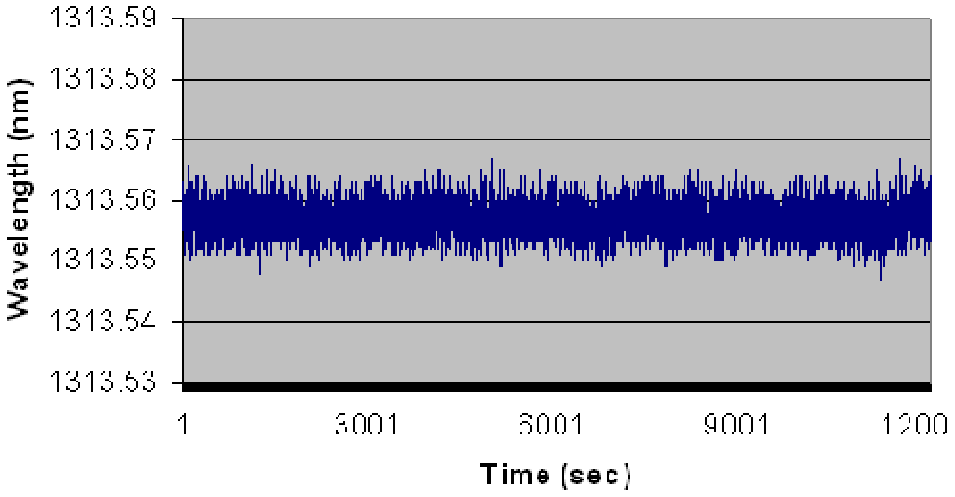

(b)

Figure 4.9 (a) Experimental setup and (b) measured wavelength as a function of time for the amplified DFB optical signal

4.2.3 *Wavelength sensitivity of intensity-modulated SOAs*

When monitoring narrow spectral lines, an essential requirement for fixed-wavelength DAS with phase-sensitive detection is to perform high-frequency intensity modulation without changing the laser wavelength. As discussed section 4.1 the absence of the wavelength-selective optical cavity in the SOA allows intensity modulation to take place without changing the wavelength of the optical carrier. This is a very important property for the intended application since any oscillations of the wavelength about the selected value will add extra complexity to the calibration of the measured absorption signal. In this section, perform a set of experiments is performed in order to establish that tuning the drive current (modulating) or the temperature of the SOA does not alter the wavelength of the emitted beam.

In this experiment a solid silicon etalon with known wavelength response is used to compare two different approaches. Firstly we tested tuning directly the driving

current of the DFB laser and secondly tuning the driving current of the SOA while keeping the DFB laser driving current fixed. Figure 4.10 shows the experimental setup for the former case. The system is comprised of an Applied Optoelectronics 1310nm DFB laser module which is driven by a Thorlabs ITC 510 Laser Diode Controller. The laser temperature has been fixed at 25°C and a digital function generator was used to generate various waveforms to tune the diode laser through the modulation input of the diode controller. The narrow (~0.01 nm) 1310 nm laser beam is pitched through a solid silicon window and then detected by a Thorlabs InGaAs switchable gain Amplified Detector (PDA10CS). All the measurements were taken at unity gain at 17 MHz full bandwidth. The received signal was then monitored on a Digital oscilloscope. The VOA was placed prior to the collimator in order to control the optical power transmitted to the detector.

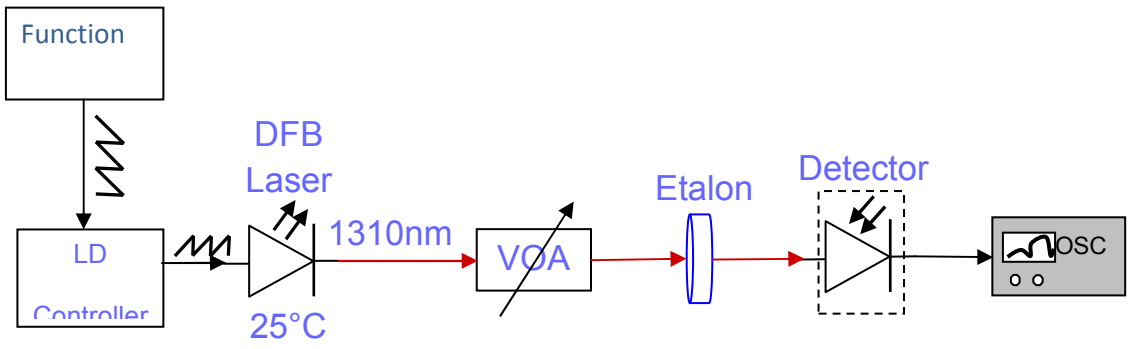

Figure 4.10 Experimental Setup for direct modulation of the DFB Laser and etalon effects investigation

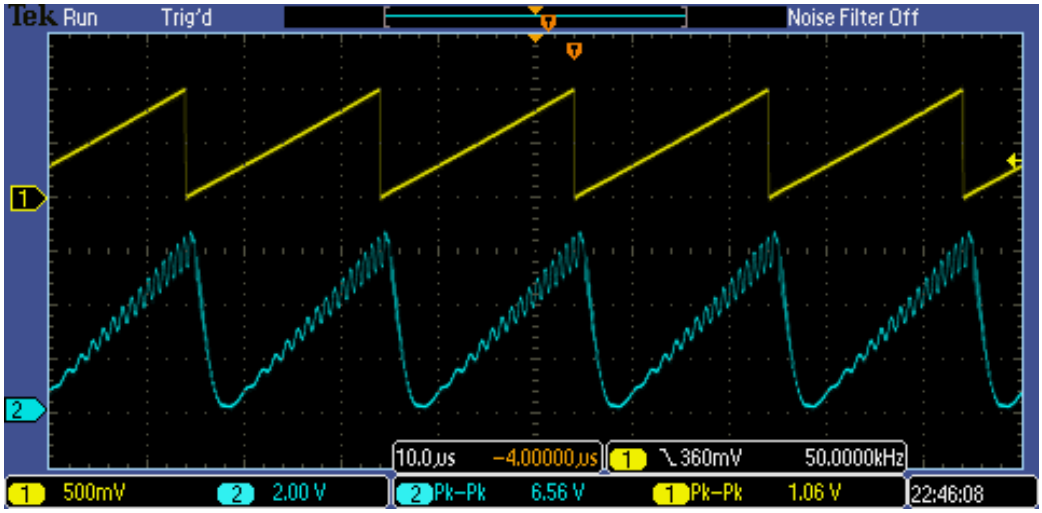

(a)

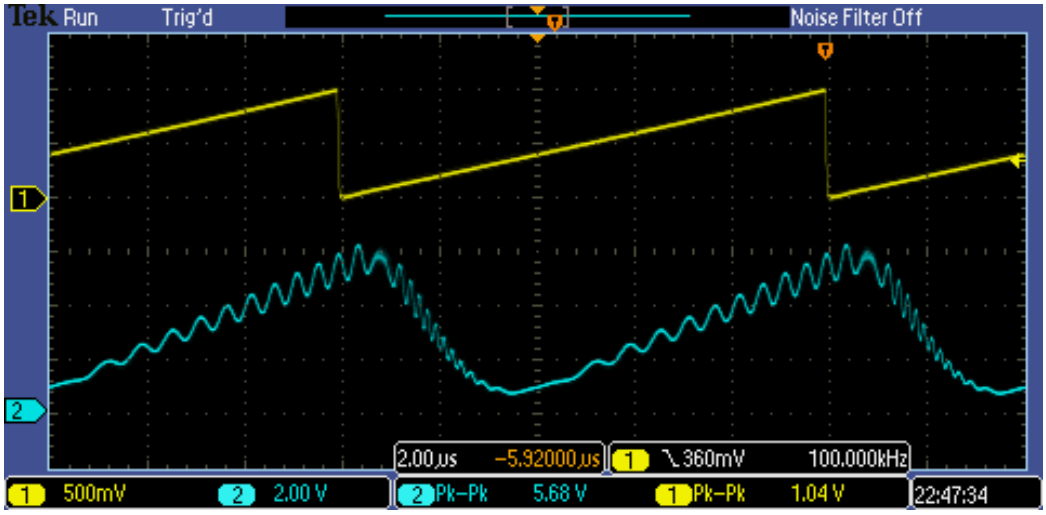

(b)

Figure 4.11 Transmitted (yellow trace) and received signal (blue trace) succeptible to etalon effects at (a) 50 and (b) 100KHz

When an optical beam is transmitted through two parallel, reflecting plates (a i.e. silicon window) the latter acts as a Fabry-Perot etalon [80, 81]. This is basically an optical interferometer which causes the optical beam to transverse in multiple reflections between the two surfaces. Since the relative reflection and transmittance of the beam depends purely on the window length and the index of refraction, solid etalons can effectively transform optical frequency (in our case wavelength) changes to intensity variation. Etalon sensitivity in wavelength variation is used extensively

in high resolution spectroscopy as an accurate wavelength tracking method [82]. In these experiments a 20 mm thick silicon etalon was used with a free spectral range (at 1310 nm) of 5.14 GHz or ~0.03 nm. Figure 4.11 shows the ramp electrical signal (yellow trace) that was used to modulate the DFB Laser, as captured by the digital oscilloscope at 50 and 100 kHz. The second channel of the oscilloscope shows the signal that was captured after travelled through the etalon window (blue trace). As expected the intensity variation of the latter signal suggests wavelength change as the drive current changes.

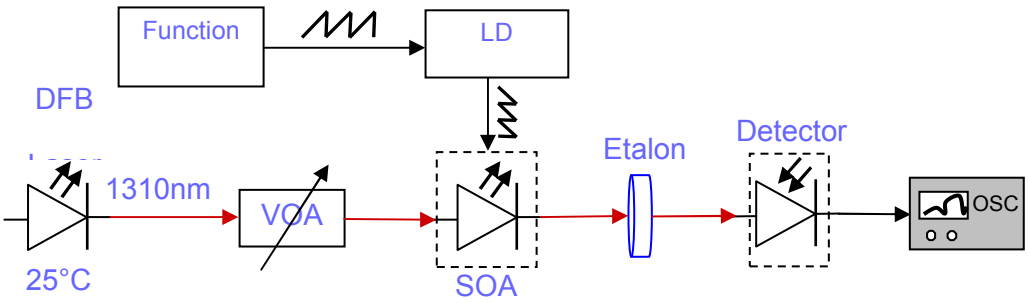

Figure 4.12 External modulation with the SOA for etalon effects investigation, experimental setup

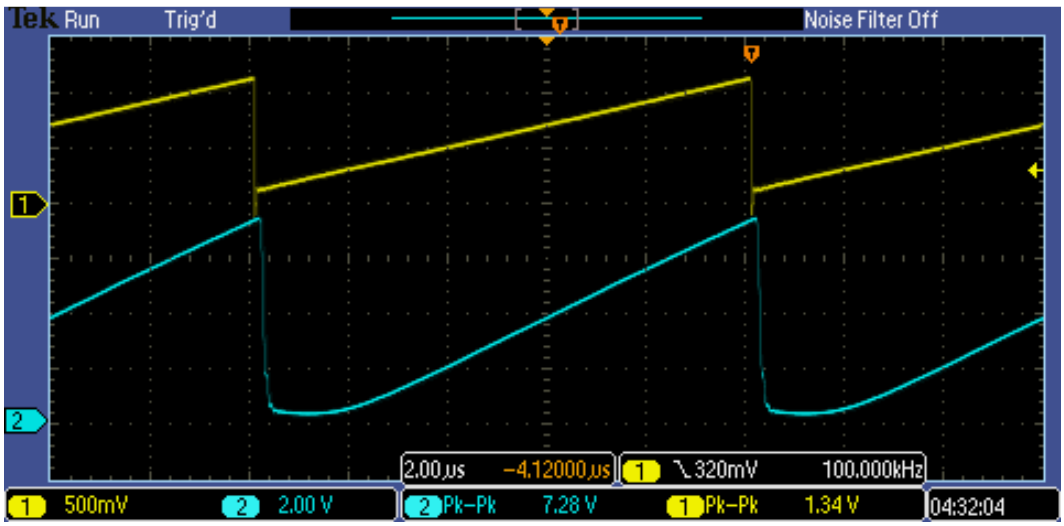

(a)

(b)

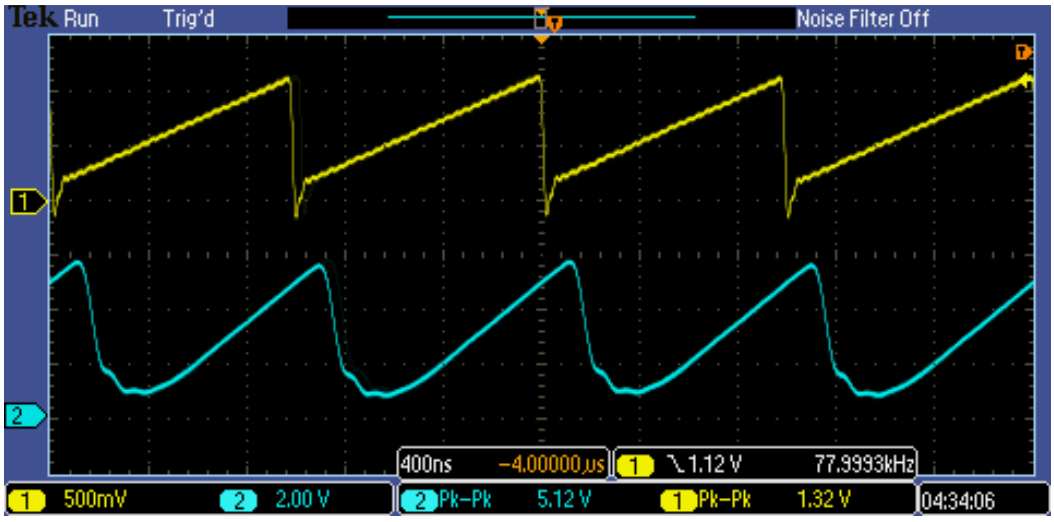

(c)

Figure 4.13 Transmitted (yellow trace) and obtained signal (blue trace) at (a) 100 kHz, (b) 500 kHz and (c) 1 MHz for the configuration in Figure 4.12

In the configuration shown in Figure 4.12 the 1310 nm DFB laser is driven with a constant 100 mA dc current from the Thorlabs controller and the temperature is fixed again at 25°C. The optical output of this laser is then used as input to the SOA after passing through the Optical Attenuator. The SOA is driven by a Wavelength Electronics LDTC2/2 Laser Diode Controller with a ramp signal similar to the one

driving the DFB laser in the configuration in Figure 4.10, and its temperature is fixed at 25°C. The SOA optical output is expected to follow the waveform of the current injected to it by the controller. As it can be clearly seen in Figure 4.13 the signal that it is captured by the detector (blue trace) is an almost identical replica of the signal driving the SOA. The absence of intensity variation on the received signal similar to that in the direct DFB modulation case (Figure 4.11) is a strong indication that the optical signal is wavelength-stable, which is the main requirement. The tests have been repeated for all three wavelengths, for different frequencies (up to 1 MHz) and a number of waveforms (sinusoid and square) and the results, apart from a minor phase shift, were equally satisfying.

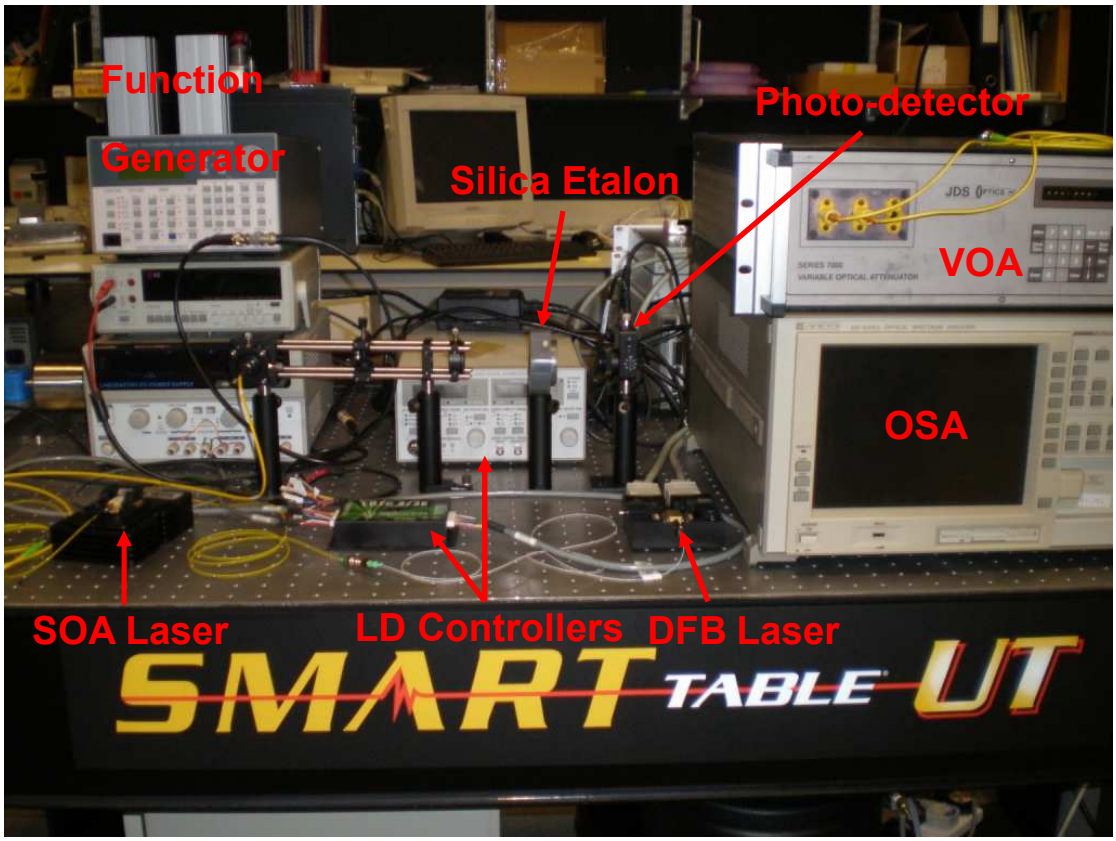

Figure 4.14 Experimental Setup

4.2.4 *Wavelength broadening and phase-sensitive detection*

In the previous section it was demonstrated that the intensity modulation of the SOA with a ramp or sinusoid signal does not affect the wavelength of the optical signal, in contrast to the behaviour observed when directly modulating the DFB lasers. This section presents an investigation of how the external modulation of the SOA driving current affects the lineshape and the amplitude of the recovered absorption signal. The implementation of SOAs for intensity modulation applications has been studied before [83,84], and efficient high-speed operation up to 2.5 Gbits/sec has been demonstrated [85,86]. Briefly, by modulating the bias current of the SOA, the semiconductor gain is also modulated and thus when a continuous wave input is applied, it is also modulated with the same frequency as the modulating current. The presence of optical gain is an advantage of this approach since other external optical modulators attenuate the optical signal. A wavelength scanning approach was used here, where the 1385nm DFB laser was driven by a relatively slow ramp waveform (100 Hz) and the SOA with a fast sinusoid signal (50-250 kHz). The ramp signal is tuned appropriately so that the transmitted wavelength is repeatedly scanned across the H_2O absorption peak at 1385.12 nm. The output signal is then pitched across a free-space path and, due to the air humidity, it is attenuated as it oscillates about the absorption peak. The transmitted signal is then detected by a photo-diode and sent to a lock-in amplifier (Brookdale 9503-SC).

Lock-in detection can considerably improve the SNR of an optical transmission system. By superimposing a high frequency sinusoid signal onto the low frequency ramp, one can move the signal away from baseband optical noise and interference from power systems and room lightning. A reference signal with exactly the same frequency and fixed phase relationship with the modulating signal is multiplied with

the detected signal. The product of this multiplication contains a component exactly at zero Hertz since the two multiplied signals have exactly the same frequency. Thus using a Low-Pass Filter one can obtain an amplified version of the low frequency input signal. As shown in Figure 4.15 a reference signal is supplied to the lock-in amplifier by the function generator which produces the modulating signal. The oscilloscope screen-image shown in Figure 4.15 depicts the high frequency modulation signal (yellow trace), the modulated received signal at the photo-detector (blue trace) and the Lock-in amplifier output (green trace).

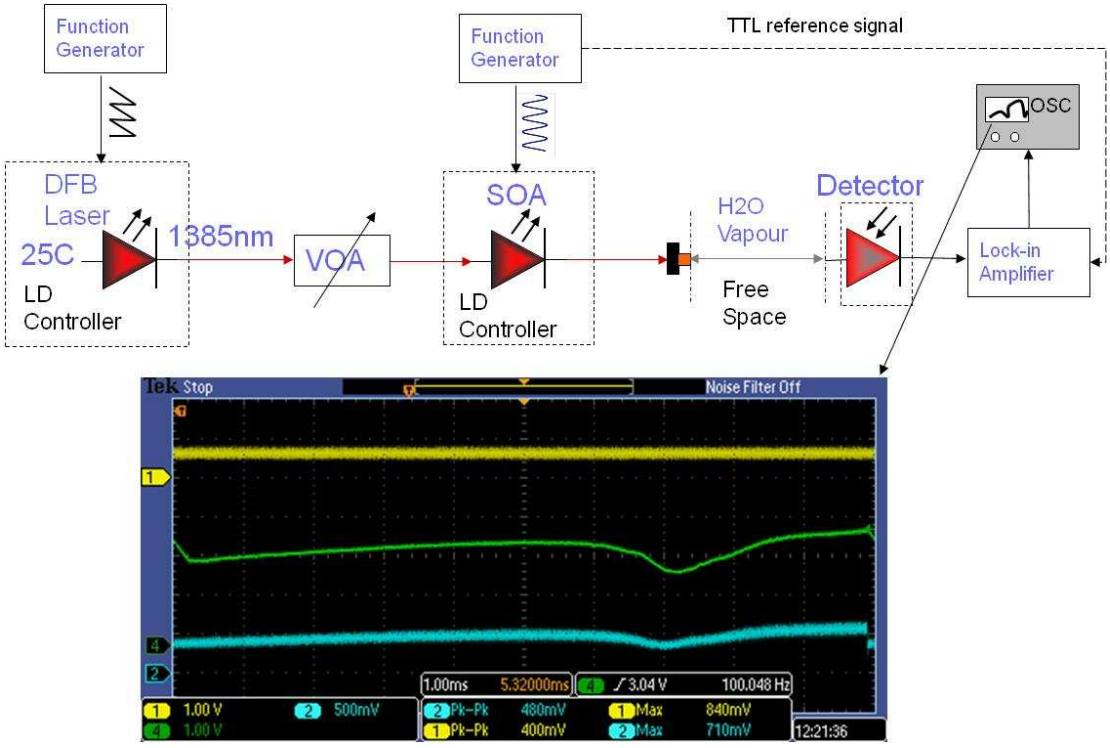

Figure 4.15 Lock-in detection experimental setup and captured signals

The measurement is repeated for different modulation amplitudes (modulation depth) of the high frequency superimposed sinusoid signal and then normalised in order to obtain comparative results. In Figure 4.16 are shown the normalised recovered signals for 50, 100 and 200 kHz after lock-in detection, and how they

compare with the detected un-modulated signal. It can be seen that by increasing the modulation frequency does not affect the lineshape or the linestrength of the recovered absorption feature. The relatively high noise is due to the limited frequency response of the LD controller used for that experiment and to a non-perfect phase relationship between the two signals. Also, the apparent quantisation noise on the traces is due to the relatively low, 8-bit, vertical resolution of the oscilloscope and the scale that have been used. From Figure 4.15 it can be seen that 8 divisions of 1V where used when the data were saved in order to depict all three signals, and for that reason the vertical resolution is only about 31mV. The resolution could have been better if smaller scale (i.e. 0.1V/div) was used. Nevertheless, as one can observe, the baseline signal recovery is very good, indicating the successful operation of SOA modulation and phase-sensitive detection. Also, varying the modulation depth did not have any significant impact on the received signal. These tests demonstrate that the proposed scheme is valid as it does not affect the shape or the line-width of the measured absorption lines.

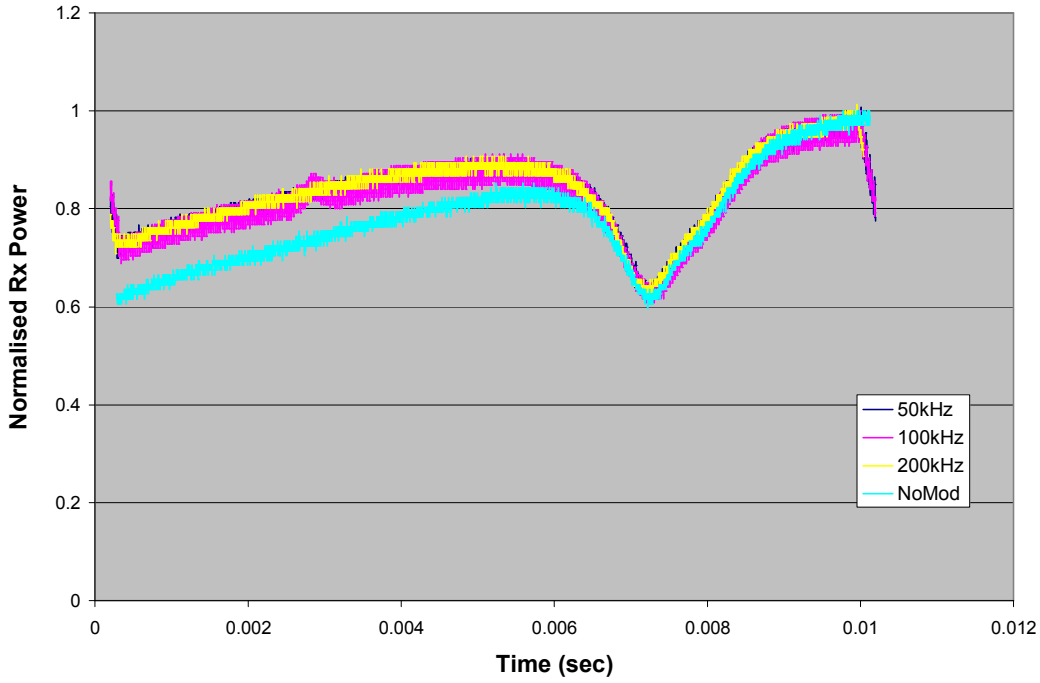

Figure 4.16 Normalised Lock-in Recovered Signal

4.2.5 *SOAs 'off-state' power leakage*

The SOAs used for this experiment are commercial devices designed to operate as in-line optical amplifiers in the region of 1310 nm. In the application proposed here SOAs are also used as optical switches for TDM operation. However, throughout the experiments reported here a potentially undesirable effect has been observed, as follows: There is an amount of optical power that leaks through the SOA when it is switched off (no modulation current is applied). This power leak increases with input power and when the light shifts towards longer wavelengths. As shown in Figure 4.17 the amount of power that leaks through the device when the drive current is zero can reach up to 10% of the total input power at 1385 nm. This effect limits the accurate TDM functionality of the SOA since at any given time there is some optical power from both wavelengths received at the detector. Nevertheless, as it is shown in section 4.2.6, for the period when the SOA is in the 'off' state no modulation

frequency is applied on the optical signal. In that case, the lock-in amplifier and the third order 30 kHz High-Pass filter [87] on the detection circuit will reject any baseband signal that lie outside the resonant modulation frequency. Thus there will be no interference to the power level on the measured absorption-induced signal.

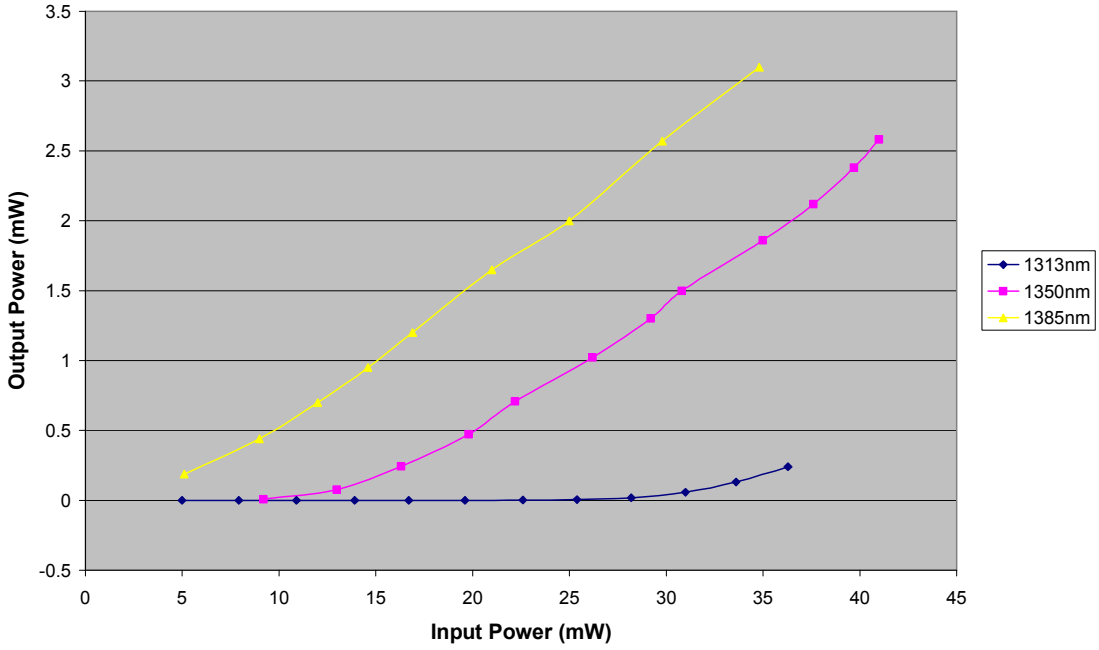

Figure 4.17 SOA Insertion Loss

4.2.6 *Simultaneous Intensity Modulation and Optical Switching*

The last requirement of the newly proposed scheme is fast switching capability for TDM operation between the two resonant wavelengths. In section 4.2.3 has been shown that directly switching on and off, or modulating the DFB Lasers, is not a practical approach, as it results in wavelength change of the optical beam which is a serious impediment for the new measurement scheme. Thus some means of external switching/modulation is required. External modulators such as Opto-acoustic, semiconductor Electro-Absorption modulators and Electro-Optic Lithium niobate modulators [88] are widely used in communication systems but are not ideal for the

design proposed here. Although they exhibit better modulation performance compare to SOAs, external modulators induce optical power loss which is critical in the proposed system as it affects the total optical power budget, in contrast to the SOAs which can amplify the transmitted signal. Thus, it is attempted to do simultaneous optical switching and modulation of the optical beam using the SOA.

The Signal Adjustment Circuit described in Chapter 3 is used to produce the TDM modulation signal and the experimental setup is shown in Figure 4.18. The TDM signal is used to drive the two SOAs through the WLD Controllers. The 1350 nm and 1385 nm DFB lasers are driven with a constant current for fixed wavelength operation. The two optical beams are amplified and modulated by the SOAs with the TDM driving signals generated by the Signal Adjustment circuit with 2 kHz switching frequency between the two wavelengths. Then they are multiplexed with a 2x2 coupler and pitched through a 10 cm free-space path before being detected by a photo-receiver. A variable optical attenuator is being used for the photo-receiver protection from excessive optical power. The DFB lasers are driven by an arbitrary dc current as the scope of this test is just to validate the operation principle of the system and not to extract accurate water vapour absorption measurements. All laser sources and amplifiers have been set to operate at 25°C constant temperature.

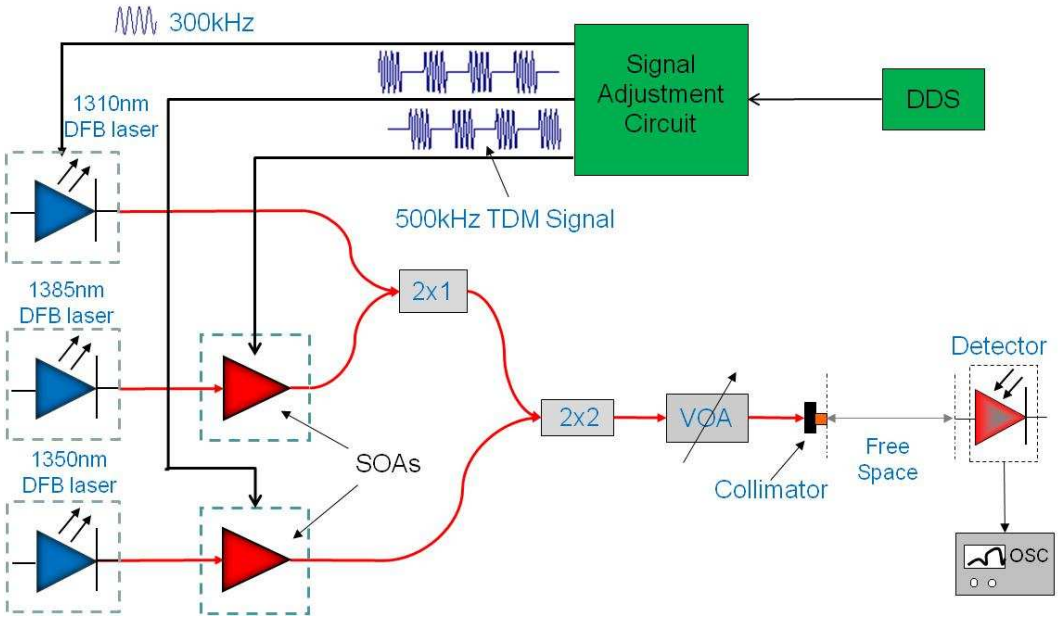

Figure 4.18 Experimental setup of simultaneous optical switching and modulation with SOAs.

All driving and detected signals were captured and analysed by the digital oscilloscope. Figure 4.19 shows the waveforms at 300 kHz driving and the detected signal for the 1310 nm reference DFB laser modulation. The good signal quality and relatively linear modulation is confirmed by the fast Fourier Transform (FFT) of these signals shown in Figure 4.20, where about 40 dB difference between the fundamental and the second harmonic component can be seen.

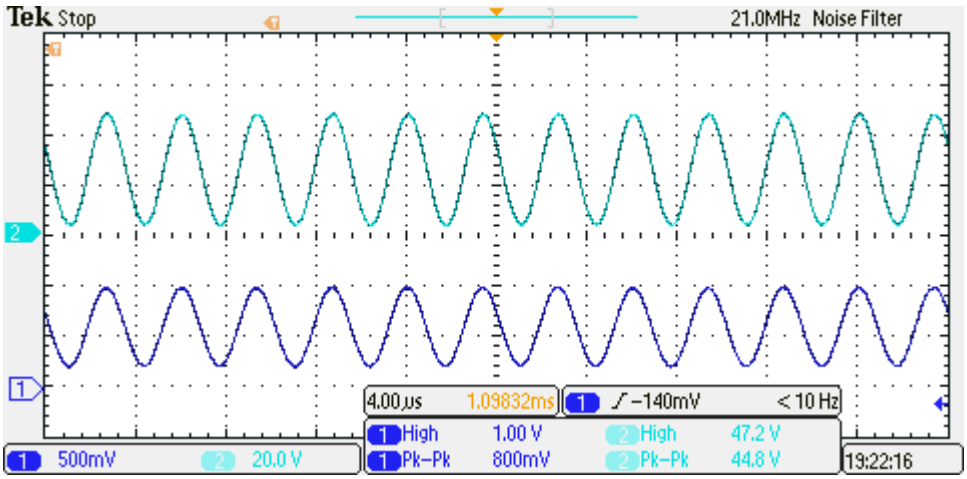

Figure 4.19 300 kHz Modulation signal (dark blue) for the 1310 nm reference wavelength and the corresponding detected (light blue) signal

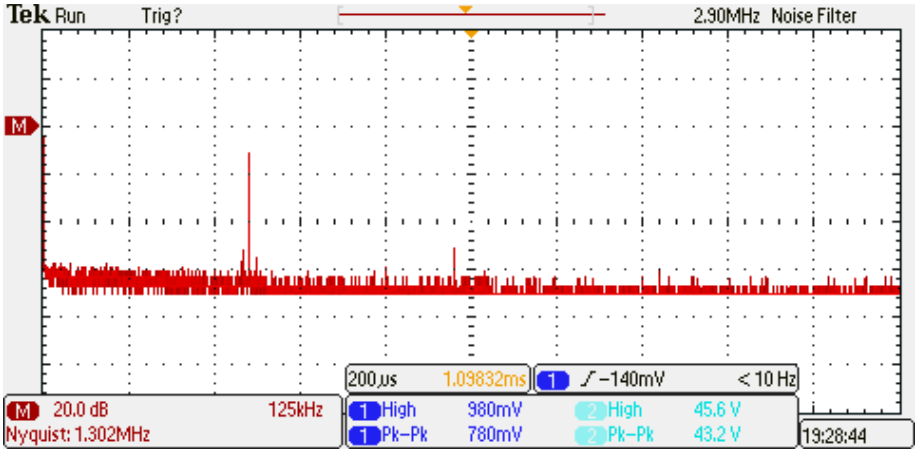

a)

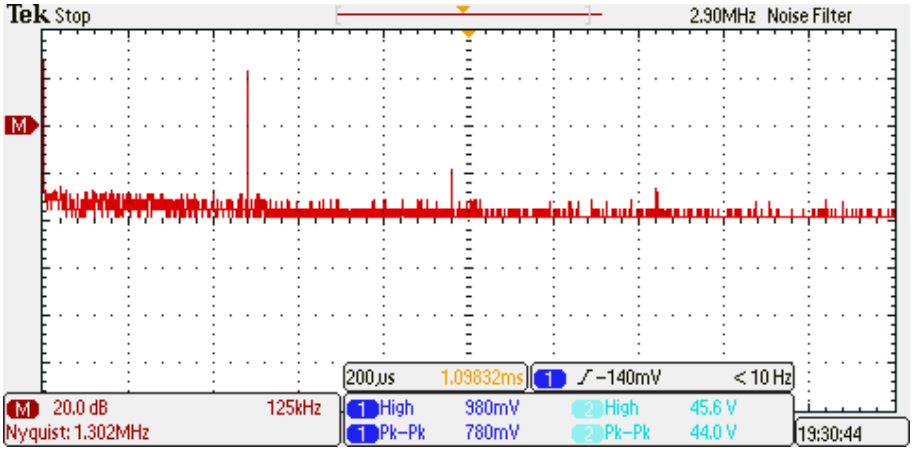

b)

Figure 4.20 Fast Fourier Transfrom for (a) 300 kHz modulation signal and (b) the received modulated signal

Figure 4.21 shows the switching waveform for the modulation of the 1350 nm wavelength SOA and the corresponding detected signal as they captured by the oscilloscope. A comparison between the FFTs' of these two signals (Figure 4.22) shows a rise in the second harmonic component at 1 MHz on the detected modulated optical signal which mainly attributed to the on/off switching effects and non-linearities of the SOA modulation. Still there is about 23 dB difference between the fundamental modulation frequency and the second harmonic component which satisfying for phase-sensitive detection. A Similar rise in the second harmonic component at 1 MHz as in the 1350 nm wavelength case can be seen at 1385 nm as it shown in Figure 4.22 and Figure 4.23. The small rise of the second harmonic component at 1385 nm compare to the 1350 nm case is mainly due to the higher Amplified Spontaneous Emission component at the first wavelength as the peak wavelength deviates from the 3 dB bandwidth of the SOA. Nevertheless, there is still a sufficient 20 dB difference compare to the fundamental modulation frequency.

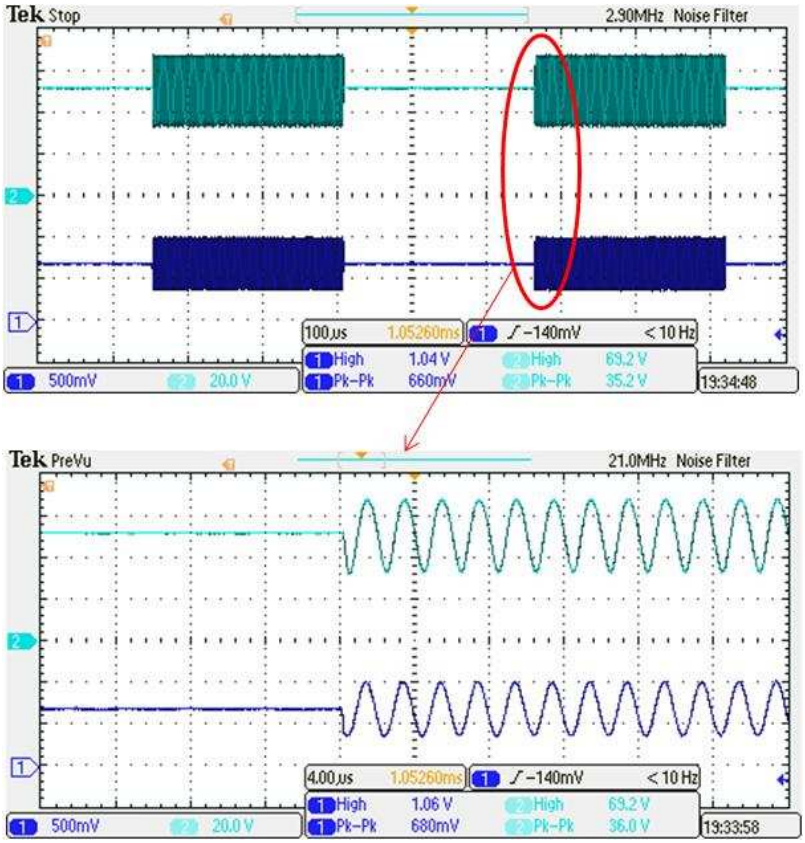

Figure 4.21 Driving (dark blue) 500 kHz TDM modulation signal for the 1350 nm wavelength and the corresponding detected (light blue) signal.

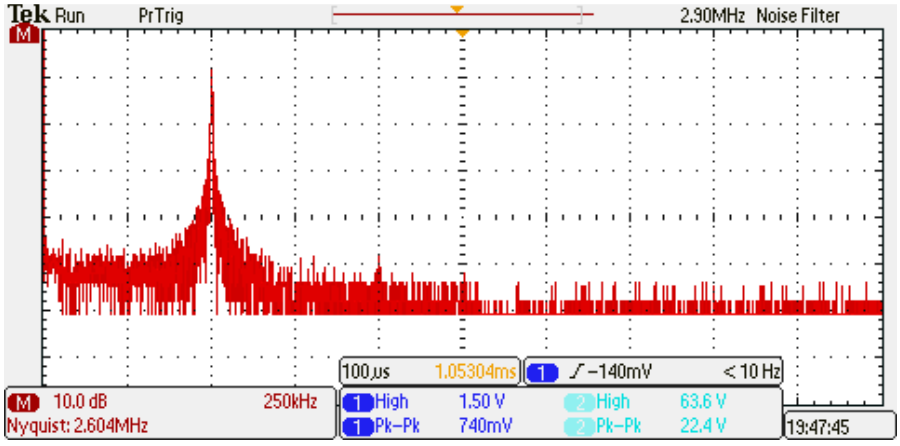

(a)

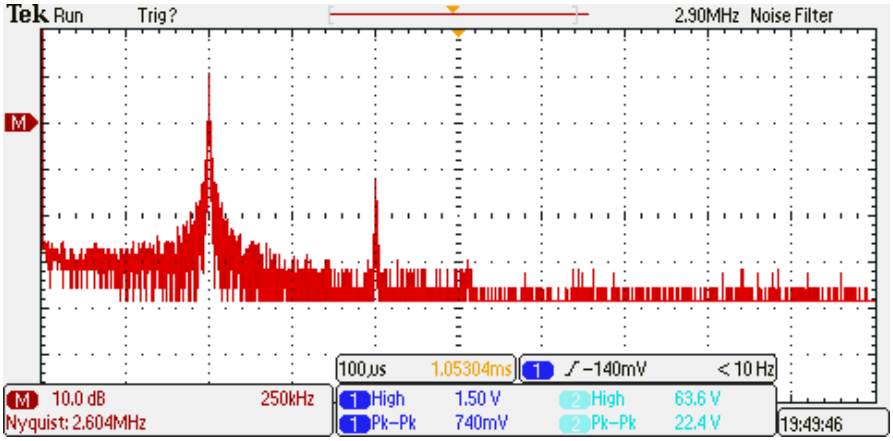

(b)

Figure 4.22 Fast Fourier Transfrom for (a) the 500 kHz TDM modulation signal for the 1350 nm wavelength and (b) the received modulated signal.

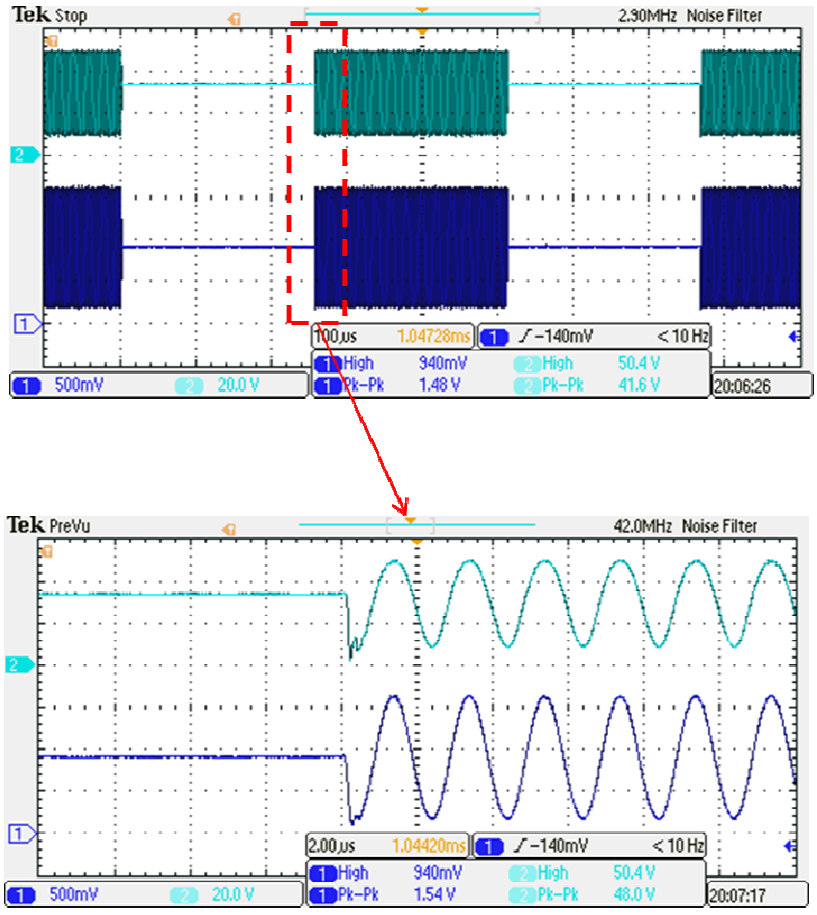

Figure 4.23 Driving (dark blue) 500 kHz TDM modulation signal for the 1385 nm wavelength and the corresponding detected (light blue) signal

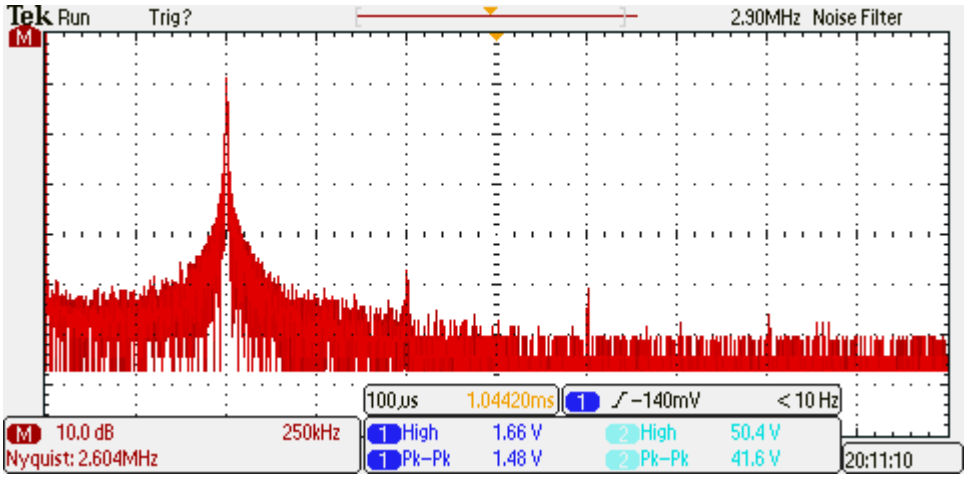

a)

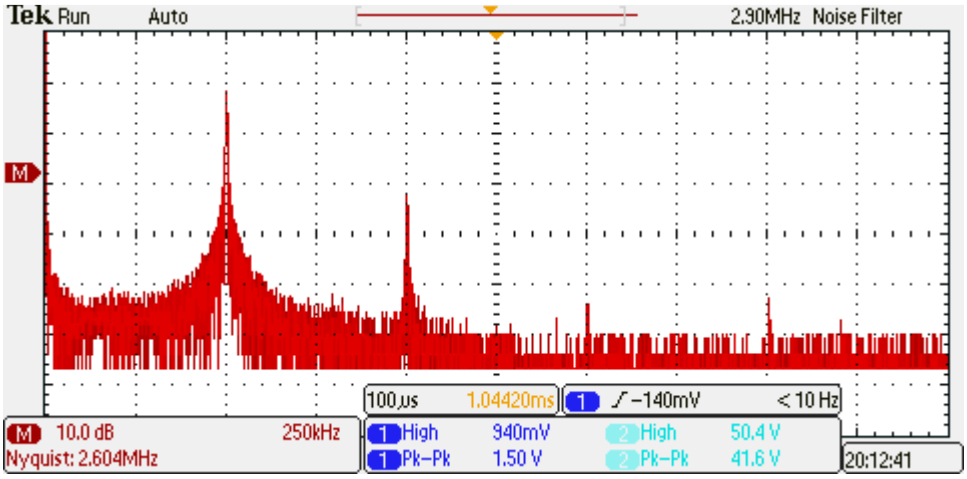

b)

Figure 4.24 Fast Fourier Transfrom for a) 500 kHz TDM driving signal for the 1385 nm wavelength and b) corresponding FFT of the received modulated signal

The result of simultaneous intensity modulation and TDM switching with SOAs can be seen in the waveform of the combined, AC-coupled detected signal shown in Figure 4.25. The modulation amplitude and dc levels were intentionally adjusted to different values so that one can easily distinguish the two multiplexed signals. A

smooth transition between the two wavelengths can be clearly seen and indicates efficient switching operation. In the FFT response shown in Figure 4.26 there is a strong 2nd harmonic signal with about 22 dB difference to the fundamental frequency which is filtered out by the lock-in circuitry.

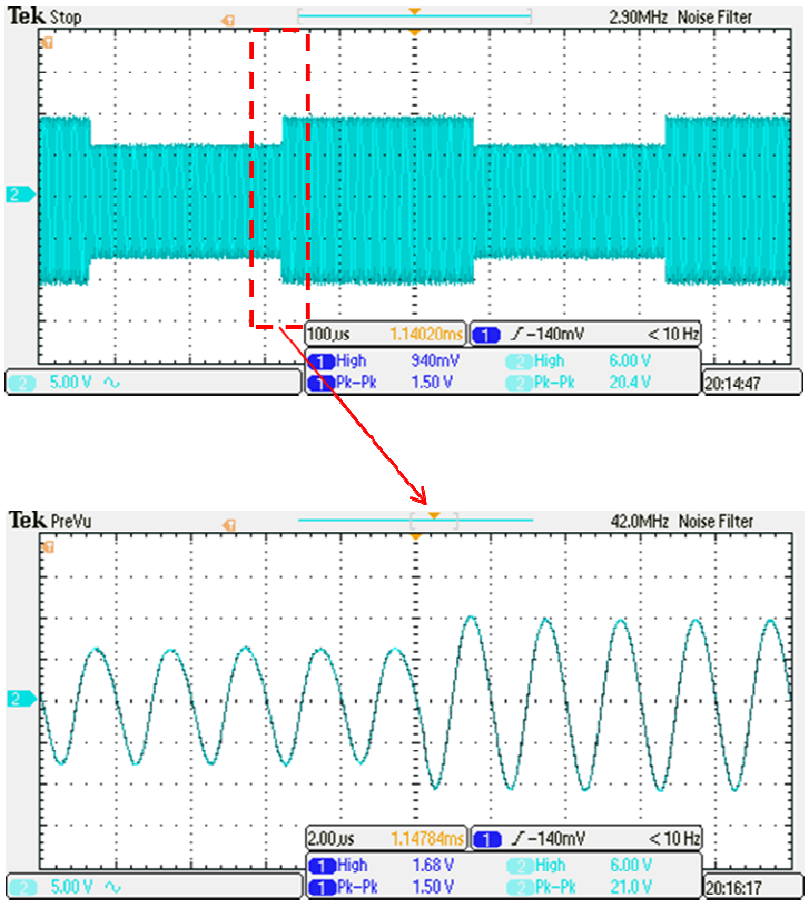

Figure 4.25 Modulated 500 kHz, Time Division Multiplexed 1350 & 1385 nm detected waveform with 2 kHz switching frequency

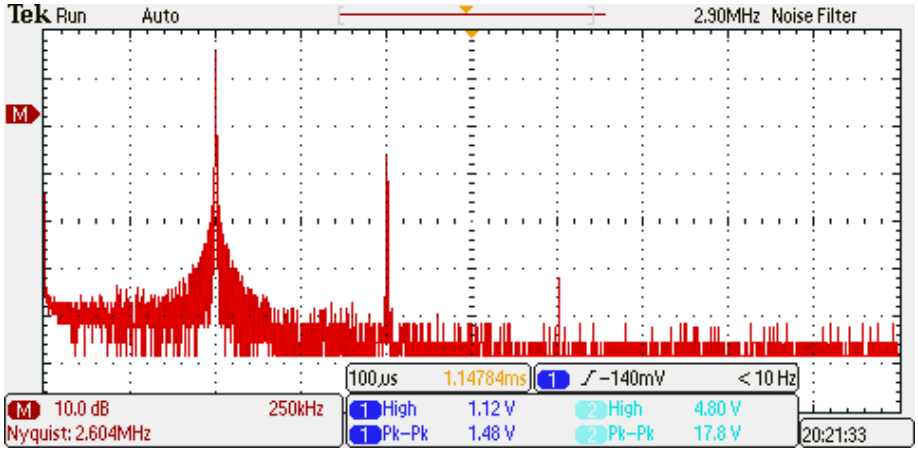

Figure 4.26 Fast Fourier Transfrom for 500 kHz Time Division Multiplexed 1350 & 1385 nm detected signals

The combination of the three modulated signals at 1310, 1350 and 1385 nm is shown by the waveform in Figure 4.27 (a). The FFT response of the multiplexed signal shown in Figure 4.27 (b) (125 kHz per division) contains the two main frequency components at 300 and 500 kHz as well as the strong second harmonic component of the TDM signal at 1 MHz. The second harmonic signal is about 22 dB weaker than the fundamental frequency at 500 kHz as in the standalone case shown in Figure 4.26. This significant second harmonic component is filtered out by the post lock-in circuitry which contains a 6^{th} order 50 kHz Low Pass filter, and will have no effect on the measured demodulated dc levels.

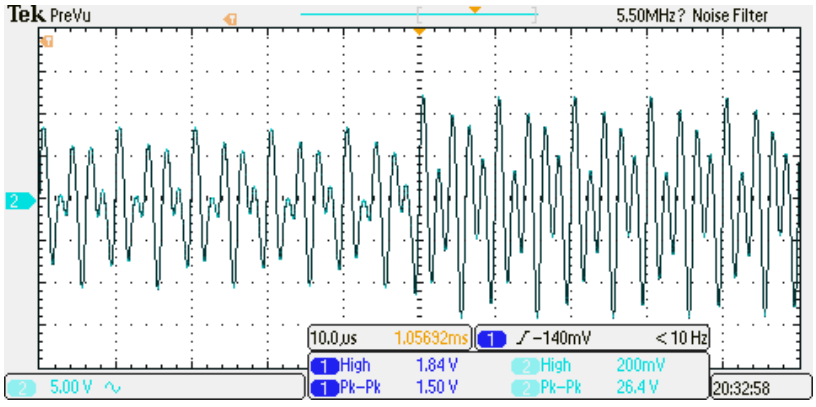

a)

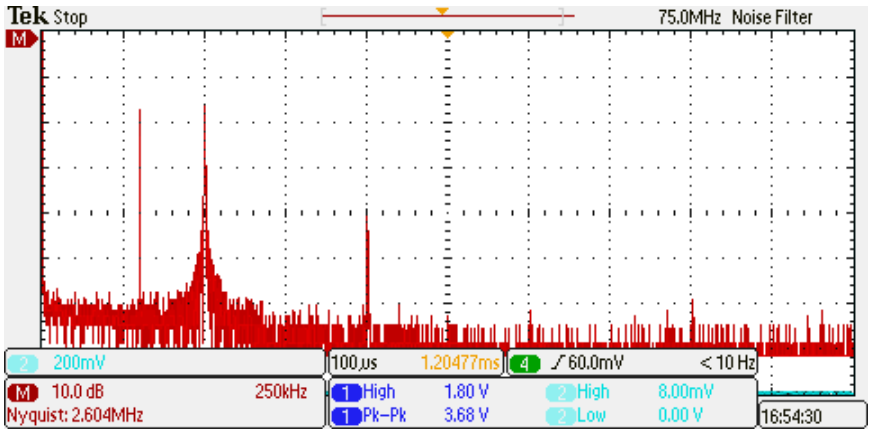

b)

Figure 4.27 (a) The three-wavelength (1310, 1350 and 1385 nm) multiplexed waveform and (b) the Fast Fourier Transfrom of the combined signal

As anticipated, both the optical modulation and switching has been successfully accomplished by the SOAs. The TDM received signal is almost noise-free and the time response to ON-OFF switching is less than a microsecond. This is not surprising, since the carrier recombination lifetime of semiconductors is in the order of tens to hundreds of picoseconds, or even tens of picoseconds in heavy saturation conditions, which is inversely proportional to the SOA modulation bandwidth [89]. The only possible limitation of this application is the excessive power input into the SOAs since the DFB lasers used for these experiments have output power levels up to 30 mW. The power saturation effect can limit the optical amplification level and the maximum modulation depth of the transmitted signals. A simple way to eliminate this unwanted effect is to place in-line optical attenuators prior to the SOAs to control the optical power levels entering the device.

4.3 **Summary**

An introduction and a general description of SOAs are given in this chapter. An S-band, commercial off-the-self device is characterised and tested based on the system's requirements. Broadband amplification (up to 1385 nm), wavelength stability over time, fast optical switching and amplitude modulation have been all tested in the lab. Wavelength insensitivity of intensity-modulated SOAs have been also successfully demonstrated, as it is a very crucial requirement of the intended application. Simultaneous intensity-modulation and optical switching with the SOA are also performed and the signal quality is assessed both in time and frequency domain.

Chapter 5

Single Channel Scanned-Wavelength Water Absorption Measurements

In order to practically establish that the newly proposed scheme meets the requirements for gaseous H_2O measurements and to evaluate its performance, a number of single-channel tests were carried out. For these experiments, it was decided to adopt a wavelength scanning approach for a number of reasons. Firstly, it is a more reliable way to establish that, by modulating the light intensity with an SOA, we do not induce any wavelength shift. Any wavelength changes due to the high frequency modulation will inevitably cause distortion and/or broadening of the recovered spectral lines. Moreover, the scanning approach provides a good assessment of the accuracy and precision of the new scheme. Finally, successful recovery of the chosen water spectral lines would be a strong indication that the new scheme can be possibly applied as an alternative to WMS for any other gas species in the Near-IR as long as strong absorption overtones are present.

5.1 Experimental Setup

The experimental setup is shown in Figure 5.1. A tunable DFB InGaAsP diode Laser (NEL NLK15BE) is driven by a 50 Hz triangle ramp signal. The diode temperature and the minimum and maximum levels of the ramp signal were adjusted so that the laser output wavelength was scanned across the entire selected water absorption feature. The triangle signal was preferred to the typically used saw-tooth ramp in

order to avoid, in the latter case, the high frequency components present at the sharp transition from the high current level back to baseline. The wavelength-tuned output of the laser was then amplified and intensity-modulated by the SOA described in Chapter 4. Two modulation frequencies were tested at 300 kHz and 500 kHz. Both the DFB Laser and the SOA were controlled by a Wavelength Electronics LDTC 2/2E controller. Before the signal entered the absorption path two small portions were tapped off, one was injected into a Fibre-Ring Resonator and used for real-time wavelength measurement, and the second went straight to a photodiode for power referencing.

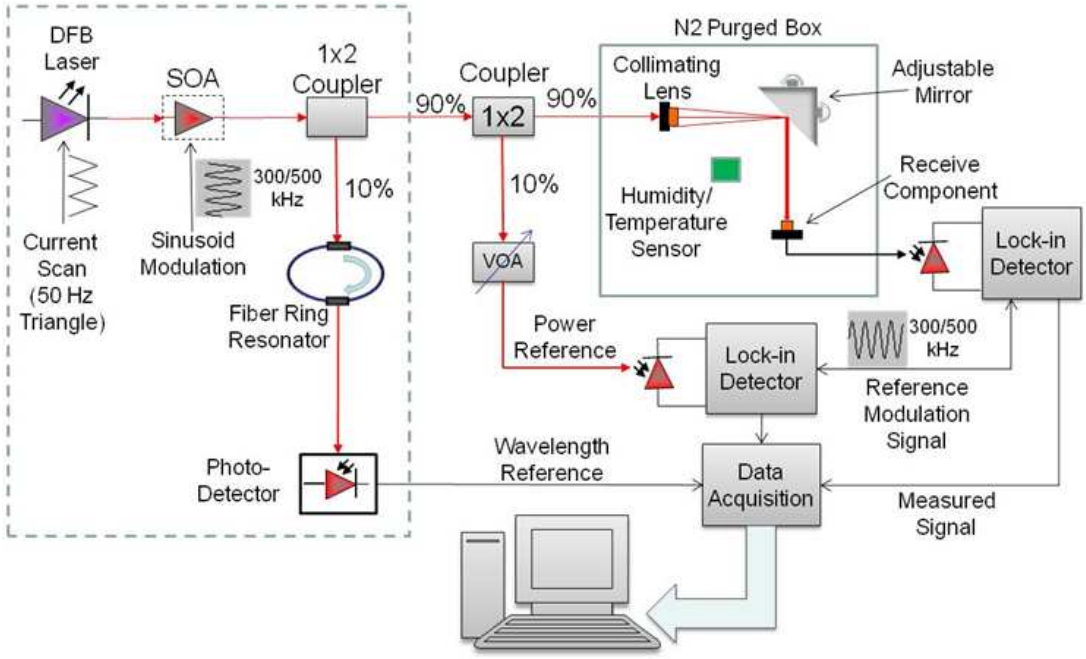

Figure 5.1 Single-Channel Scanned-wavelength measurement experimental setup

The modulated signal was then pitched through a 20 cm optical path and partly absorbed due to the water content of the atmospheric air. In order to achieve better control over the relative humidity (RH) in the absorbing path, the latter was carefully placed in a partly shielded box as shown in Figure 5.1. The air in the box could be purged of water using a nitrogen flow. The resulting “zero water” absorption signal

can be used as a highly accurate power reference signal, since it is otherwise subjected to the same transmission losses as the measured absorbed signal when water is present. An RH and temperature sensor (Sensirion EK-H5) with up to 5% absolute error was used to continuously monitor these two variables near the absorption path area. Prior to the light being pitched across the absorbing path it was collimated with an anti-reflection coated, adjustable focus aspheric lens (Thorlabs CFC-2X). An adjustable mirror was also used as shown in Figure 5.1 to provide the extra two degrees of freedom for optimum beam alignment between the send and receive optical components.

5.2 **Real-time Wavelength Reference**

In order to obtain accurate spectral linewidth measurements a high-resolution wavelength tracking mechanism is required. A simple solution could be to use a commercially available wavelength meter. However, this option is impractical in this case due to the fast scanning rate of the diode lasers, and the signal fluctuations due to the intensity modulation. Moreover, the relationship between the current scan value and the wavelength shift is non-linear due to thermal effects. Bulk optics such as solid Fabry-Perot etalons have been previously used for monitoring the wavelength change of the transmitted signal in similar cases [22]. A portion of the transmitted light is tapped off and pitched through a component with known wavelength response. The output signal consists of consecutive fringes which have wavelength spacing between them proportional to the changes of the input frequency. The distance between two consecutive peaks is called the Free Spectral Range (FSR) and it is given by Eq. 2, where c is the speed of light in vacuum, n is the refractive index of the medium, L is the length of the medium, and θ is the angle

of incidence. The water absorption features that are to be scanned in this work have a linewidth of about 0.3 nm FWHM at 1 atm. Thus, the FSR of the etalon should be at least tenfold smaller in order to obtain an adequately resolved wavelength scale. Based on Eq. 5.1 an etalon with 0.3 GHz FSR should be about 70 cm long which is clearly impractical and cost prohibitive.

$$FSR = \frac{c}{n * L * cos\theta} \tag{5.1}$$

In this work we designed and fabricated a fibre-ring resonator similar to the one proposed by Johnstone et al. [90]. This component consists of two spliced 2x2 optical couplers and produces a response as shown in Figure 5.2, similar to the solid etalons. The fibre resonator is relatively low cost, needs no alignment and is stable. The FSR follows Eq. 2 and the wavelength resolution can be simply improved by increasing the length of the ring cavity. Using Urquhart's analyses [91] and MATLAB [Appendix B] the response of the ring resonator was modelled. Figure 5.3 shows the simulated response for about 90 cm total ring length and different coupling ratios from 20-80%. As can be seen, the finesse (contrast ratio) depends on the coupling ratio into the ring. For this work the resonator was fabricated by SIFAM with two identical 60-40% couplers, with 40% optical power going into the ring. In order to create the wavelength mapping on the time axis three well-documented water absorption lines were used as absolute wavelength reference. These lines are located at 1350.25 nm, 1350.42 nm and 1350.7 nm, and can be all recovered with a single scan of the diode laser. The MATLAB code performing these tasks is given in Appendix C. By simultaneously recording the scanning signal and the resonator response the frequency change between each peak is calculated as described in [90].

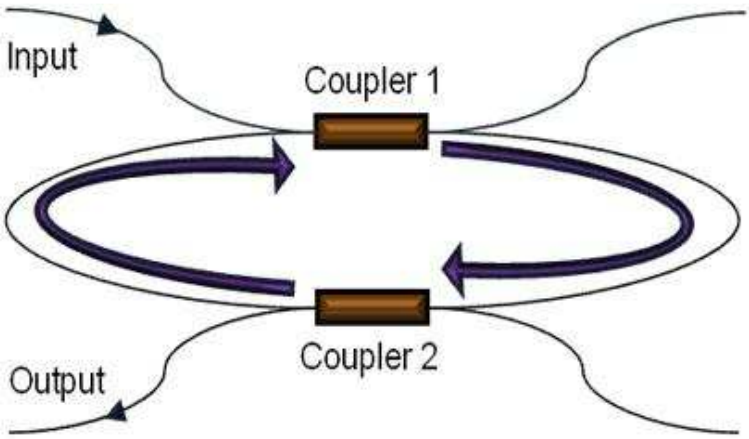

Figure 5.2 Schematic of fiber-ring resonator.

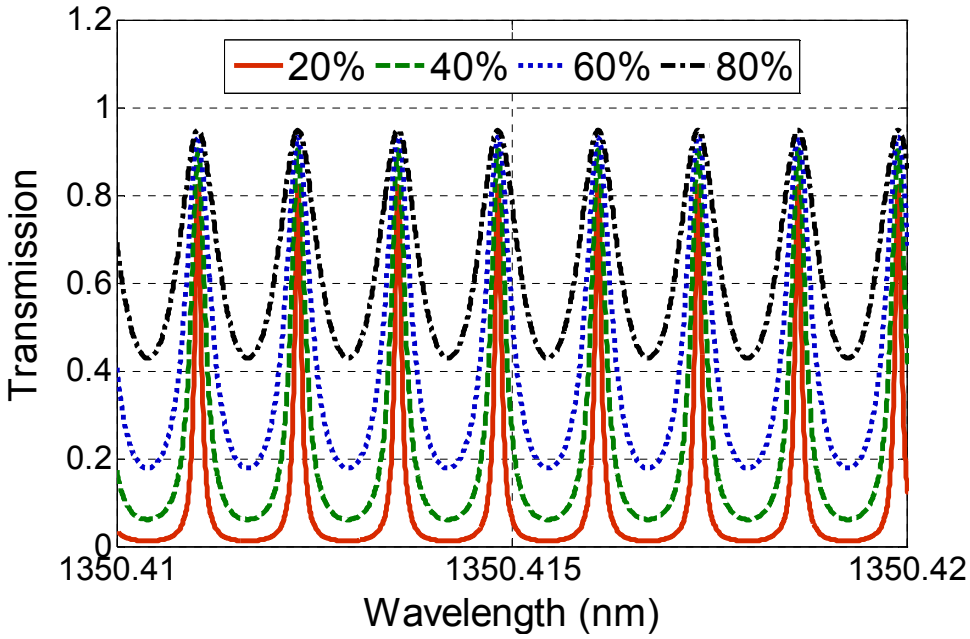

Figure 5.3 Simulation of the Ring-resonator transmission response with wavelength for 80cm ring length and different coupling ratios into the ring.

5.3 Data Acquisition and Processing

All measured signals (absorbed signal, power reference and the resonator response) are sent out with BNC cables to a 1.25 MS/s, 12-bit National Instruments PCI-6071E

data acquisition card. A Labview visual code has been implemented to simultaneously record the measured signals at a rate of 250 kS/s. Synchronous data acquisition is an essential requirement, especially for accurate wavelength reference and spectral line visualization. Figure 5.4 shows an example of received data for a scan around the 1385.12 nm overtone, (where the absorbed signal is shown by the blue curve). It also shows the recorded signal of the power reference fraction as well as the "zero" absorption signal for the case where the optical path is fully purged of water. The power reference signal was scaled with an optical attenuator and any remaining offset were subtracted in order to match with the transmitted signal. It can be seen that the density of the resonator signal is not uniform with the time index, due to the fact that the wavelength variation over an individual scan is not linear in terms of wavelength versus time. Wavelength mapping of the received signal based on the resonator signal

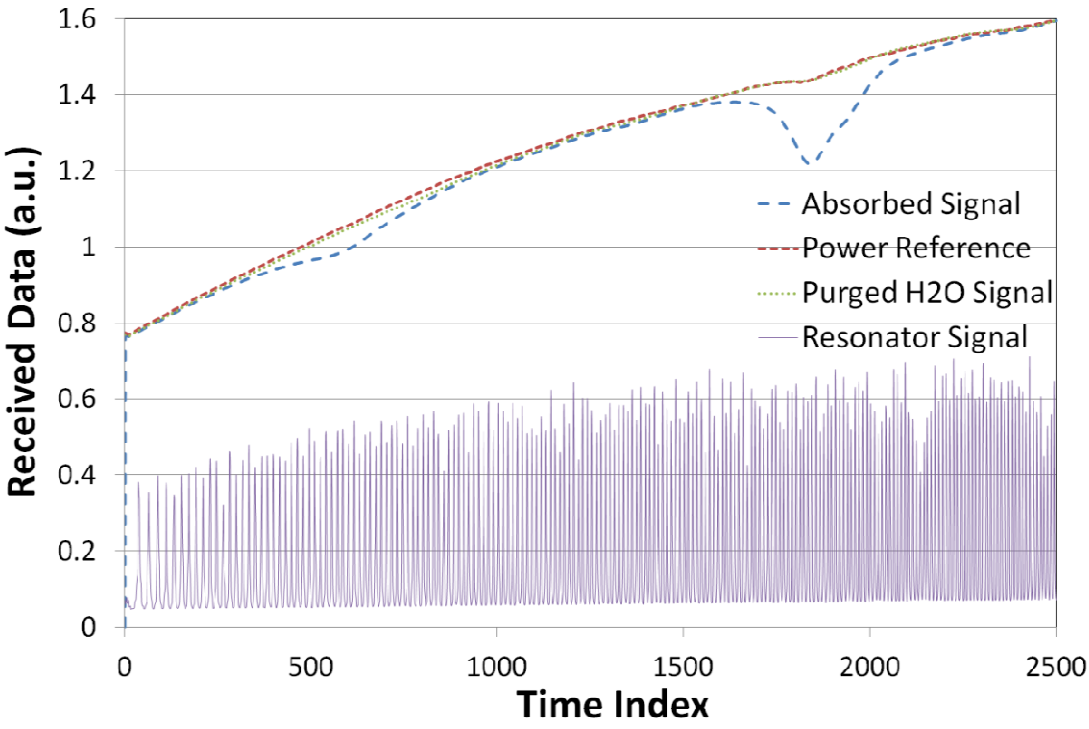

Figure 5.4 Example of acquired data (1385 nm). The power reference signal was adjusted with a variable optical attenuator to match with the transmitted signals.

Absolute absorption line recovery is achieved by taking the point-by-point ratio between the absorbed signal and the baseline "zero" absorption signal. Two options have been considered for this task. The first option was to use the power reference channel as the baseline, and the second was to use the purged humidity signal instead. However, as is clearly illustrated in Figure 5.5, there are significant differences between these two signals. These discrepancies are mainly due to the different transfer characteristics between the two transmission channels such as reflectivity, mode coupling and material dispersion. On the other hand there is very good matching between the absorbed and the purged signal in the zero absorption areas. Thus, all the recovered spectra shown in this work have been obtained by taking the ratio between the absorbed and purged signals.

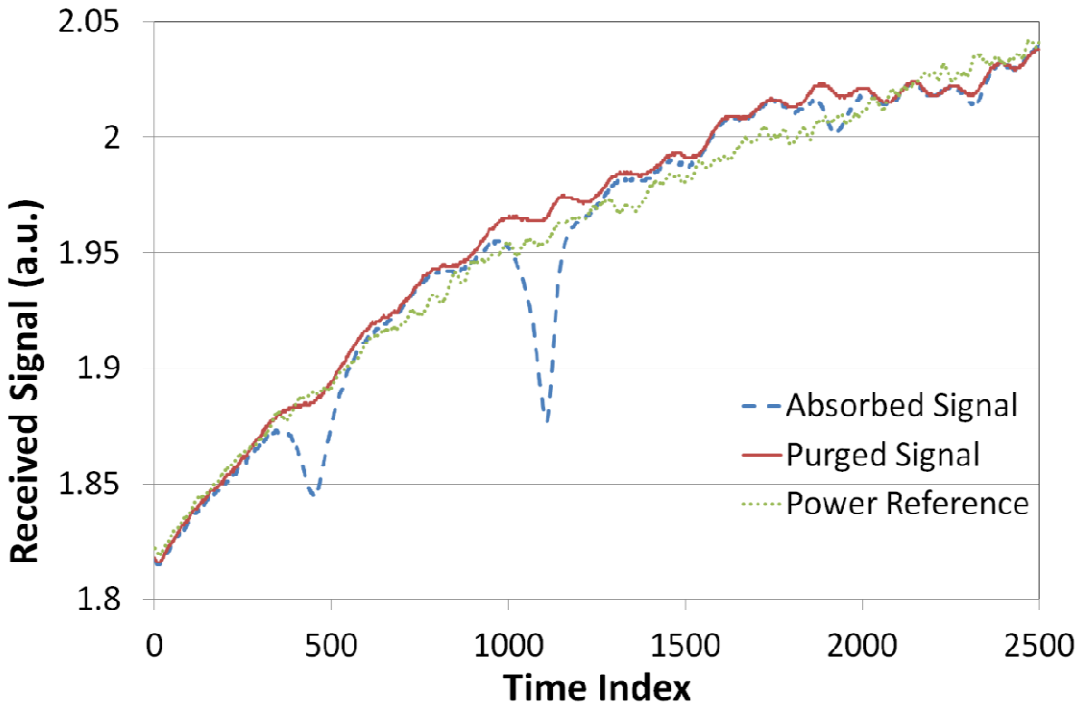

Figure 5.5 Acquired data at 1350 nm. The baseline discrepancies between the power reference and partially absorbed signals dictate the method for the spectra recovery.

Statistical noise has also been taken into account in each measurement by averaging 100 consecutive scans, and assessed by calculating the standard deviation (STD) of the measurement at each scan point. This was a point-by-point averaging process implemented in Labview prior to the ratio calculation. The data were also separated and processed individually in up-scan and down-scan sets around the peak of every triangle scan. This was necessary because of thermal properties related to wavelength mismatch between each side of the triangle ramp. Figure 5.6 shows a typical example of the variation of STD with time (i.e. wavelength) for 100 scans around the 1350.42 nm absorption peak. The absolute STD, i.e. precision, for each scan point was in the range 0.002 – 0.003 a.u., which is 0.1 – 0.2% relative precision of each measurement.

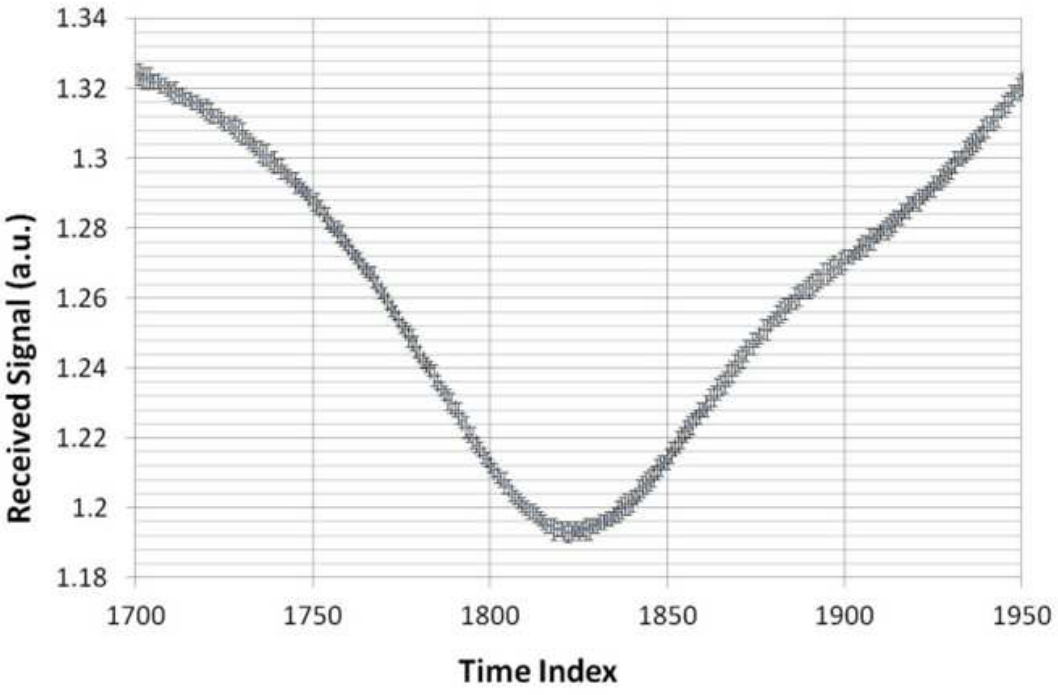

Figure 5.6 Average of the received signal (+- standard deviation) for 100 scans

5.4 **Signal Reception**

With a view to evaluating the performance of the proposed scheme a number of different signal receive methods have been tested. The properties of the receiving component are extremely important as they have a major impact on the overall noise performance of the system, thus determining the sensor sensitivity. Multimode (MM) fibre is commonly used in engine applications for receiving light and delivering it to a photodetector, and the implications have been extensively studied [92,93]. The relatively large core diameter allows good optical coupling, easy mechanical alignment and high throughput. These are very useful properties in a harsh environment where beam steering and light scattering are dominant effects. However, the high number of optical modes propagating along the fibre follow slightly different paths, causing constructive and destructive interference amongst the modes and creating a random speckle pattern on the detector surface. Any changes occurring on the optical link such as fibre vibrations, etalons and wavelength shifts, enhance the modal noise effects, which appear as random non-Gaussian noise.

Figure 5.7 shows an example of recovered spectra at 1350 nm with bare multimode fiber used as the receive component. The spectra are overlaid with the simulated data for the same conditions (40% RH, 23°C, 1 bar). Although there is a relatively good fit between the absorption features, there is a clear mismatch in the non-absorbing areas. Similar effects are present in the 1385 nm region (Figure 5.8) where the experiments is repeated three times but the recovered spectra always deviate considerably from the simulation. Significantly contributing factors for this divergence are the intermediate time interval between the absorbed and humidity-

purged measurements used for this line. The system was also extremely sensitive to vibrations and any source of optical fluctuation or electronic interference. Thus, when using a multi-mode fibre for signal reception the accuracy and precision of the measurement were significantly impaired by etalon and modal noise effects.

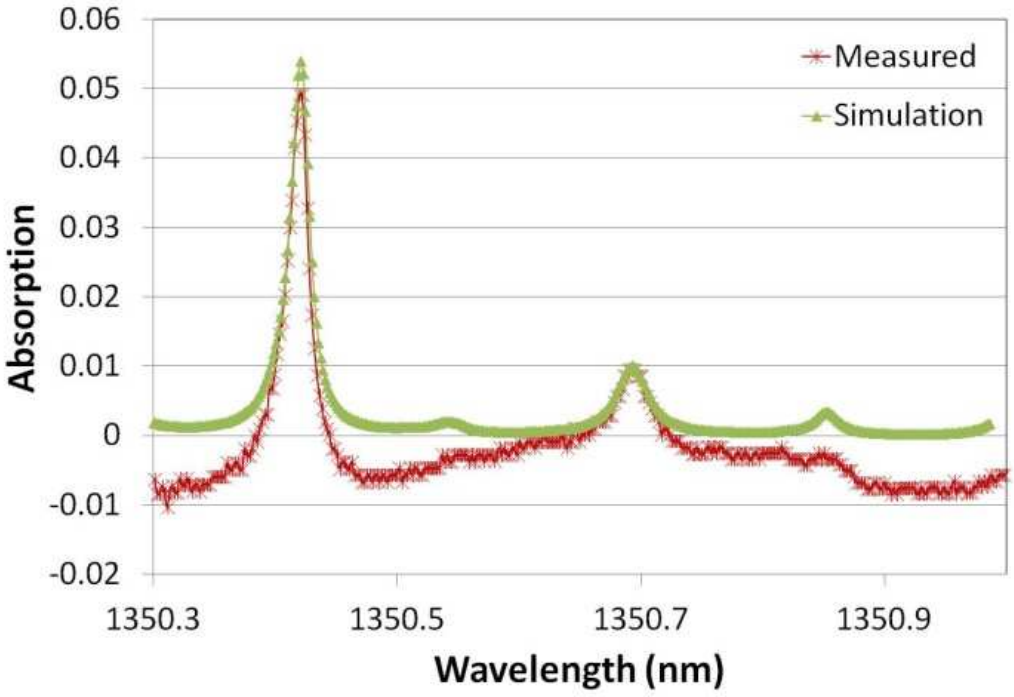

Figure 5.7 Recovered absorption features in the 1350nm region with Multimode Fiber as receive component (40% RH at 23°C).

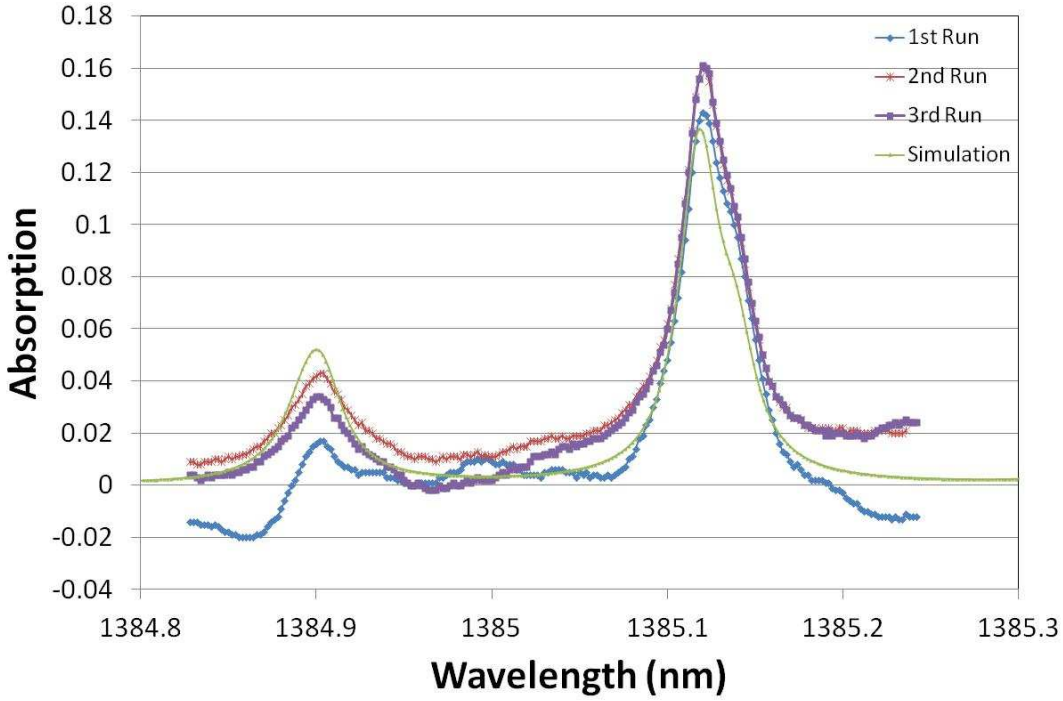

Figure 5.8 Recovered absorption features in the 1385 nm region with Multimode Fiber as receive component (35% RH at 21.5°C).

Another commonly used approach for enhanced light capturing is the use of Gradient Index (GRIN) fibre collimators. In this work we tested both SMF 9/125 μm, and 100/110 μm MM fibre collimated with AR-coated, 1.8 mm diameter lens and 0.5 NA in a stainless steel cylindrical tube about 25 mm long (GRINTECH GmbH, Jena, Germany). Collimated MM fibre offered easier alignment and high power throughput but suffered the same modal noise effects as the bare multimode fibre. The GRIN rod collimated single mode (SM) fibre however, was almost free from modal noise interference. Figure 5.9 shows an example of recovered spectra around the 1350.42 nm absorption peak overlaid with simulated spectra under the same conditions. An excellent correspondence between the absorption features can be seen, although there is still some mismatch in the baseline, probably due to back-reflections and etalon effects. In the 1385 nm case shown in Figure 5.10 etalon effects are also small compared to Figure 5.8. Nevertheless, the main drawback of

the single mode fibre is the coupling efficiency sensitivity due to the small core diameter and the susceptibility to vibrations, especially under the extremely harsh conditions that prevail in engine measurements.

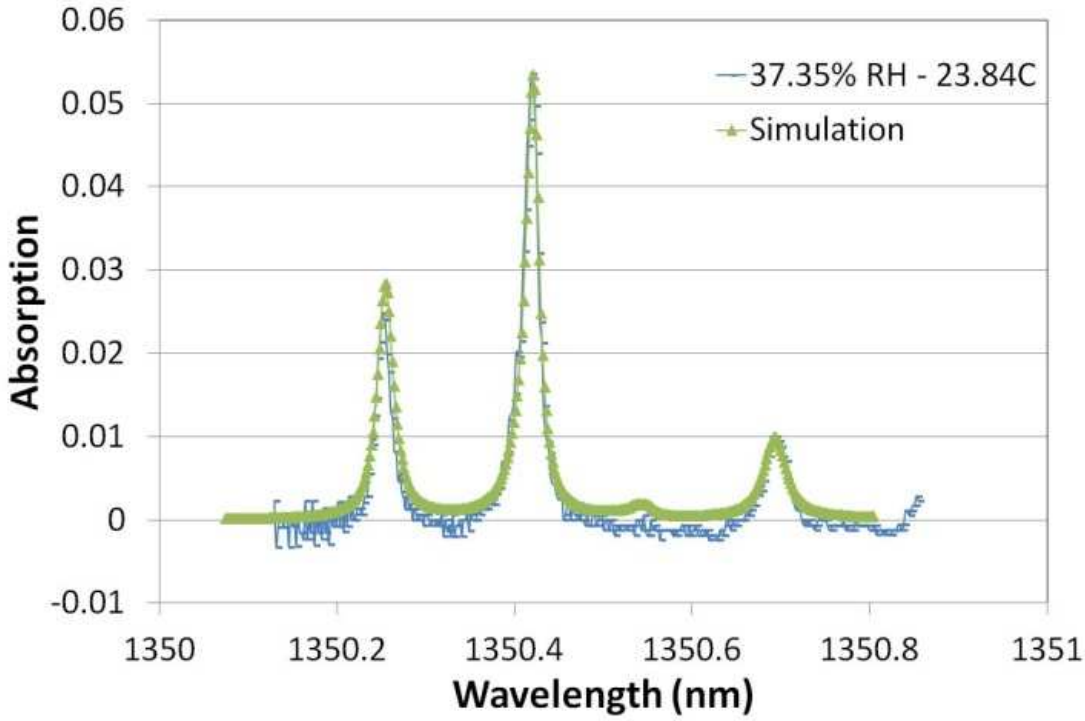

Figure 5.9 Recovered absorption features in the 1350 nm region with Single Mode GRIN Rod Collimated Fiber as receive component (37.35% RH at 23.8°C).

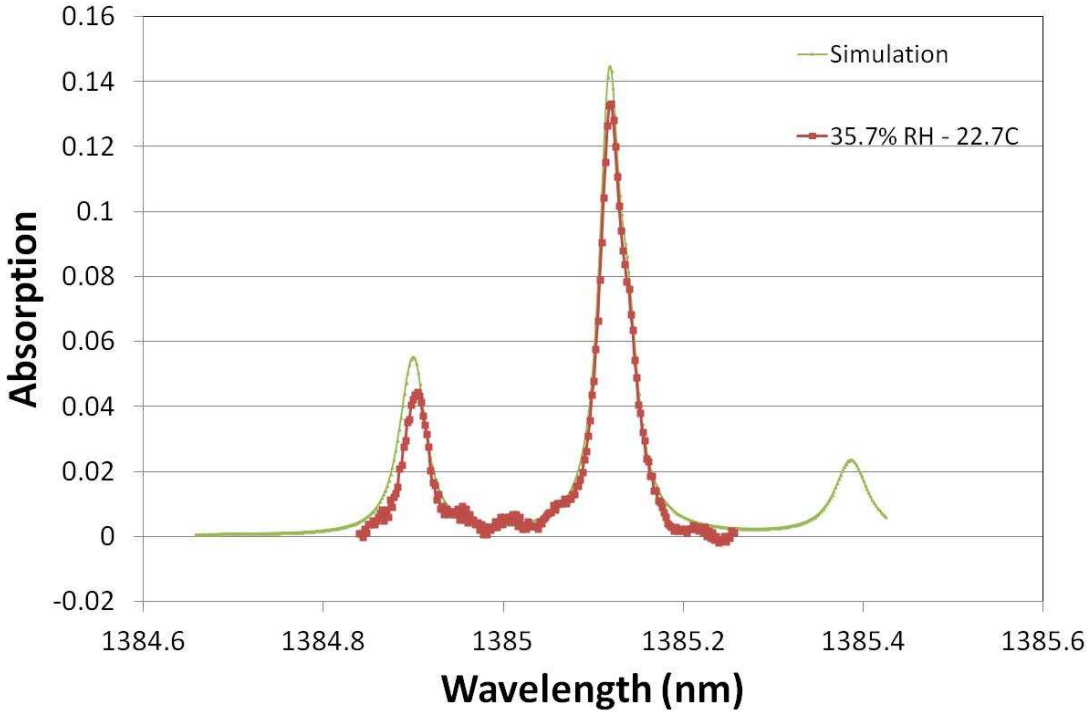

Figure 5.10 Recovered absorption features in the 1385 nm region with Multi Mode GRIN Rod Collimated Fiber as receive component (35.7% RH at 22.7°C).

5.5 Photo-Detector Signal Reception

All the signal reception approaches tested in the previous section introduce some optical noise in the recovered data. Since the scope of this work is to evaluate the newly proposed scheme, it was decided to minimise these effects by coupling the transmitted light beam directly into the photo-receiver. Figure 5.11 and Figure 5.12 show a few typical examples of recovered absorption lines at 1350.4 and 1385.1 nm using this approach. The two different modulation frequencies at 300 and 500 kHz have been tested without having any significant effect on the recovered data. By directly coupling the optical beam to the detector, excellent spectral line recovery for both tested wavelengths can be achieved. The baseline noise is virtually eliminated. Also mechanical vibrations and fibre orientation had minimal effect on the scanned measurement. The latter is a key property since engine applications are inevitably

exposed to such conditions. Comparison between measurement and simulation in Figure 5.11 shows absorption accuracy at the peak of the 1350.42 nm transition to be better than 0.3%; other scans at different RH values yield accuracy as good as 0.2% at the peak of this transition. The linewidth and the line-shape of the recovered absorption features of interest are also almost identical to the simulated ones, apart from a slight mismatch on the wavelength scale (Figure 5.11, Figure 5.12 (b)) which is in the limits of the wavelength resolution (0.02 nm).

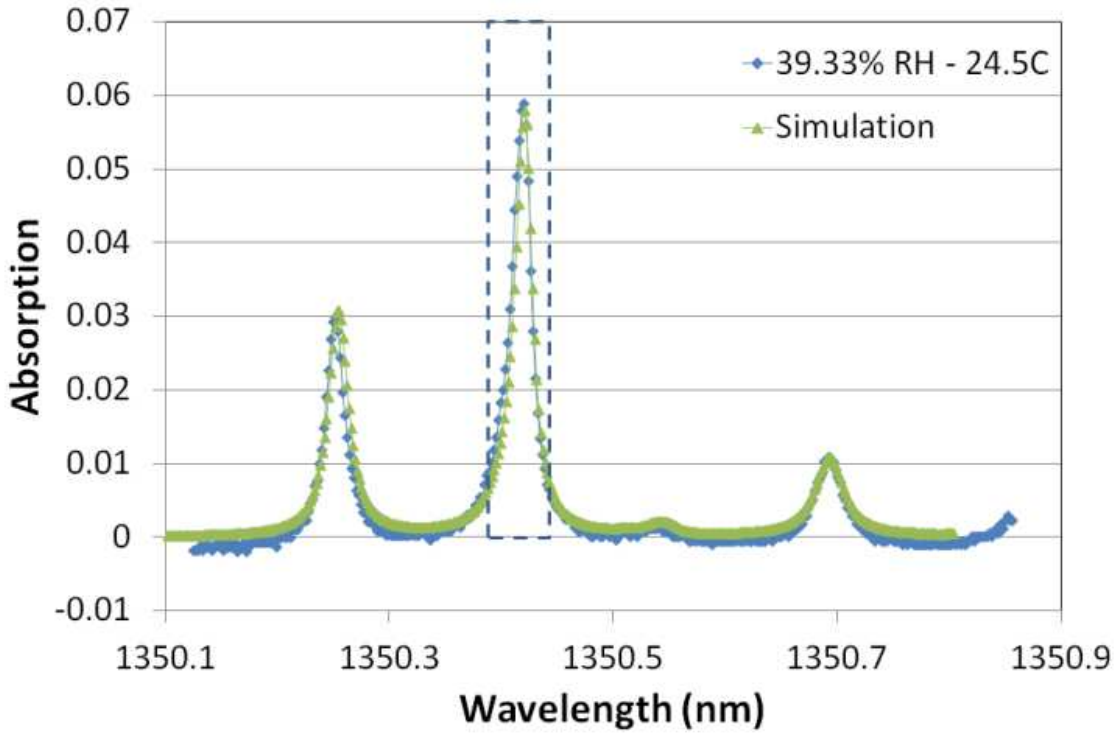

(a)

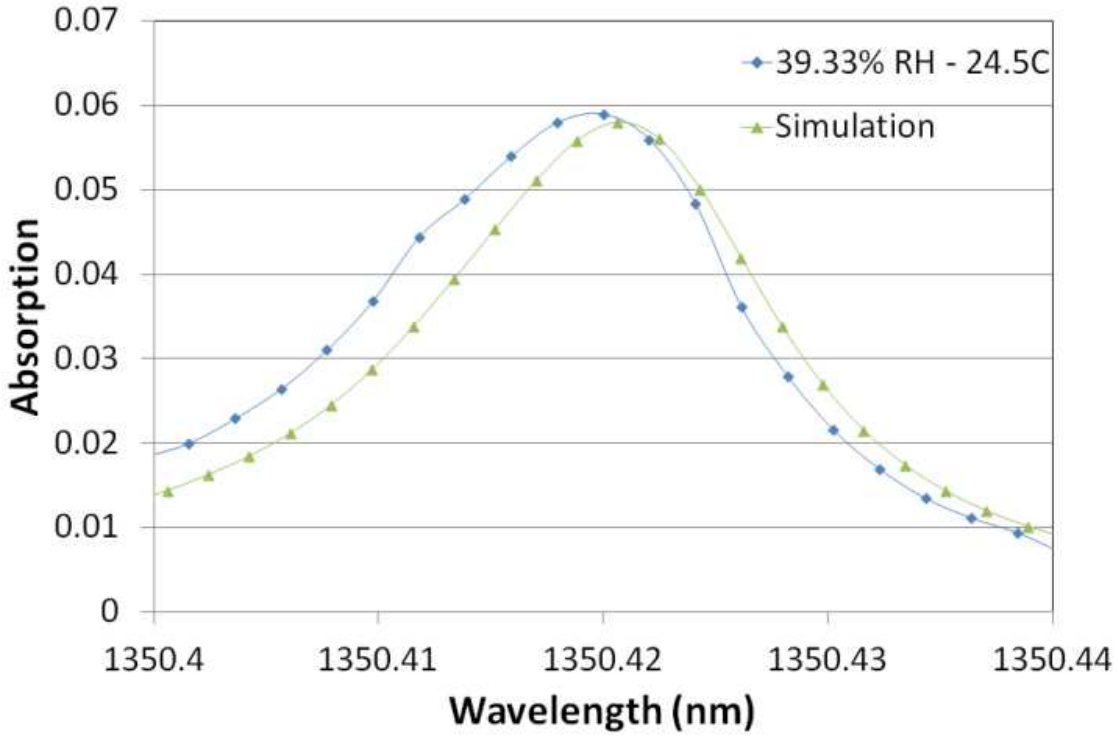
0.07
0.06
0.05
0.04
0.03
0.02
0.01
0
Absorption
39.33% RH - 24.5C
Simulation
1350.4
1350.41
1350.42
1350.43
1350.44
Wavelength (nm)

(b)

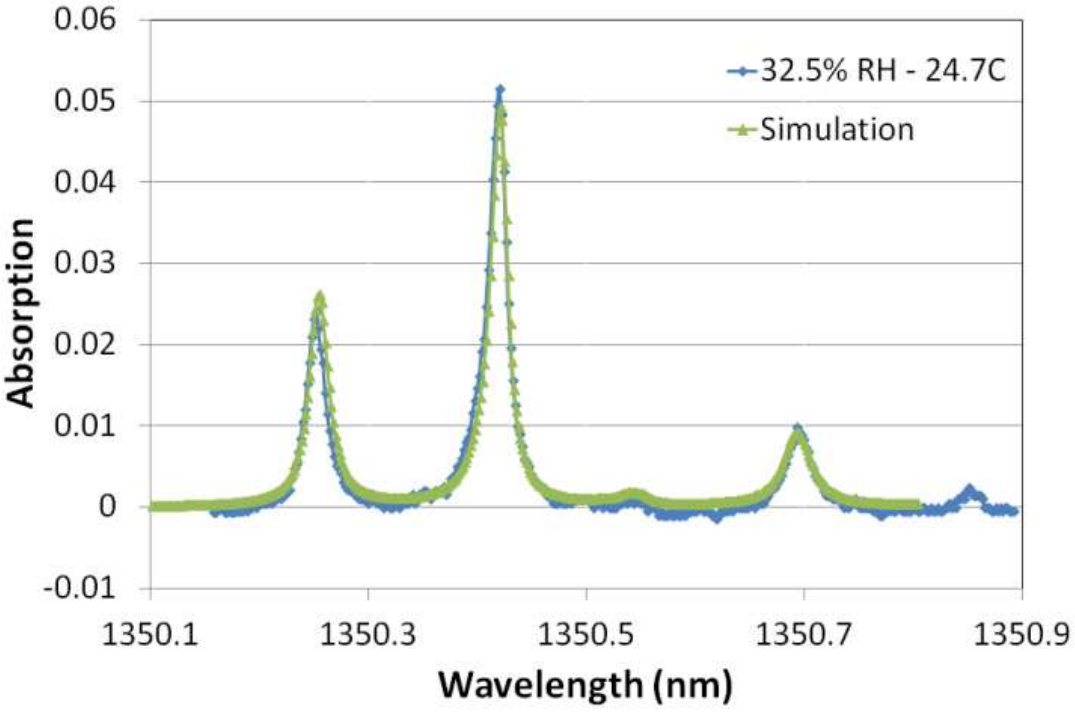
0.06
0.05
0.04
0.03
0.02
0.01
0
-0.01
Absorption
32.5% RH - 24.7C
Simulation
1350.1
1350.3
1350.5
1350.7
1350.9
Wavelength (nm)

(c)

Figure 5.11 Measured water absorption spectra in the 1350 nm region (a) 300 kHz modulation frequency, (b) a narrow part of the spectrum in (a), around the selected peak absorption, and c) 500 kHz modulation frequency.

In the case of the 1385.12 nm transition the peak absorption accuracy is poorer compare to the 1350.42 nm case, at about 1.5% (Figure 5.12). The poorer accuracy at 1385 nm could be attributed to the fact that this particular wavelength is located well outside the 3 dB operating bandwidth of the commercial SOA used for these experiments. The discrepancy is also within the limits of the RH error as measured by the humidity sensor. As expected, the carrier modulation frequency and the amplitude of the intensity did not alter the recovered spectral linewidth. It is also interesting to note that saturation of the SOA when the input power was too high did not have any detrimental effects on the recovered dc signals. Measurements show great repeatability apart from a power offset mismatch observed occasionally between the absorbed and the purged signal, probably due to transmission changes between the two measurements.

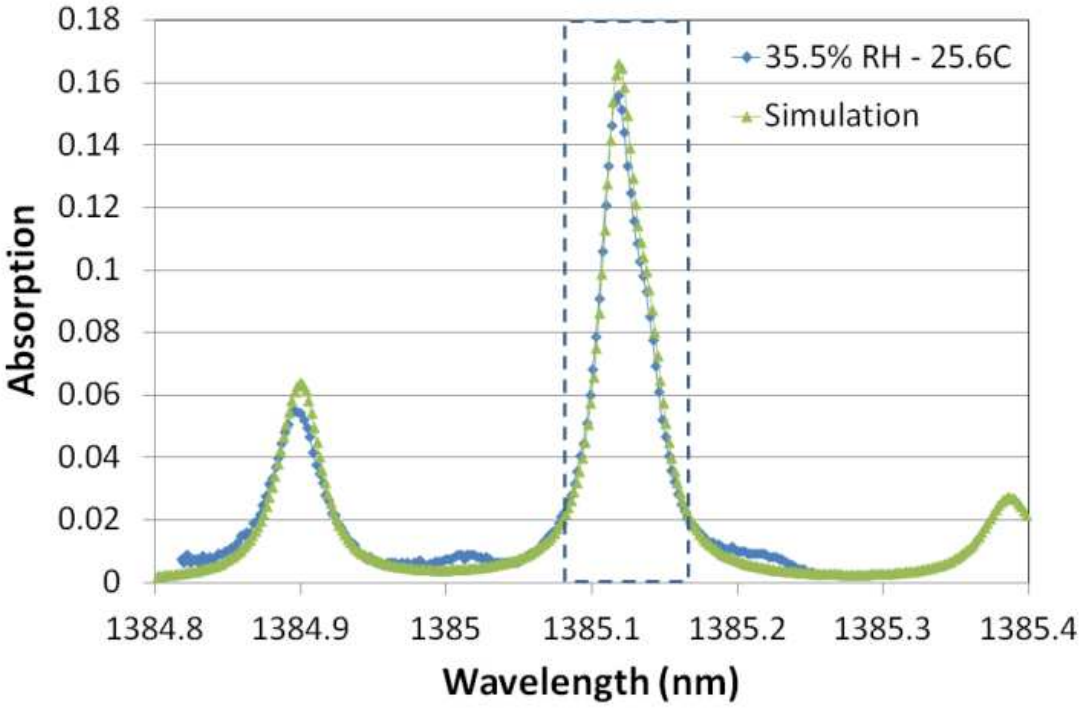
0.18
0.16
0.14
0.12
0.1
0.08
0.06
0.04
0.02
0
Absorption
35.5% RH - 25.6C
Simulation
1384.8
1384.9
1385
1385.1
1385.2
1385.3
1385.4
Wavelength (nm)

(a)

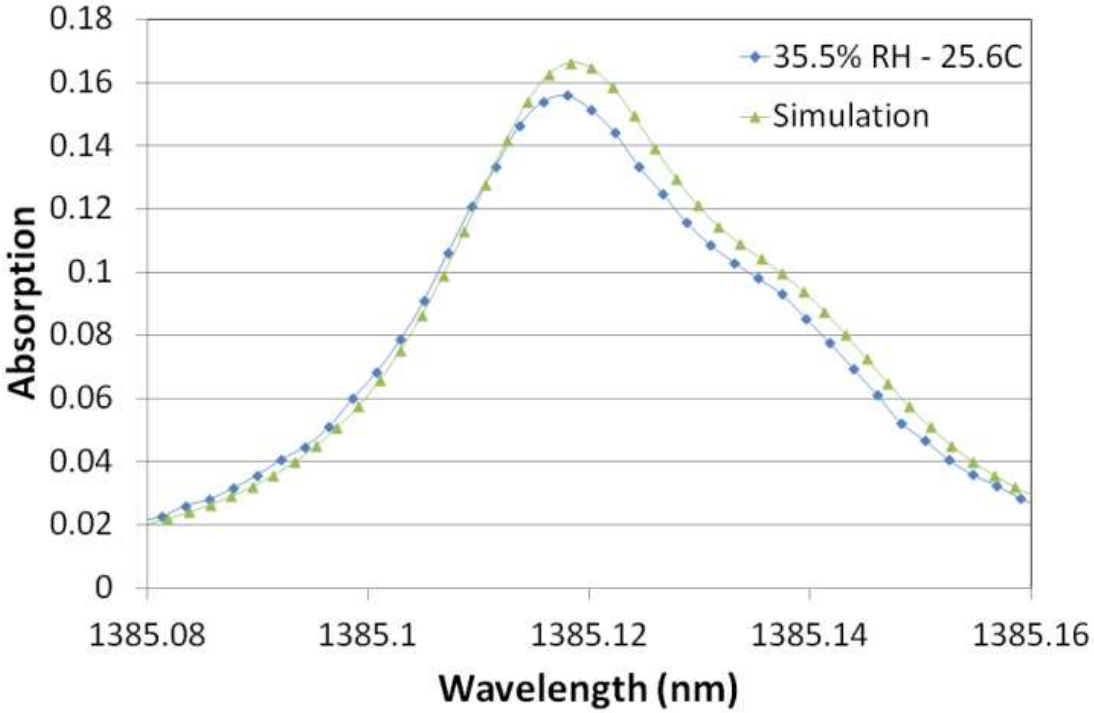
0.18
0.16
0.14
0.12
0.1
0.08
0.06
0.04
0.02
0
Absorption
35.5% RH - 25.6C
Simulation
1385.08
1385.1
1385.12
1385.14
1385.16
Wavelength (nm)

(b)

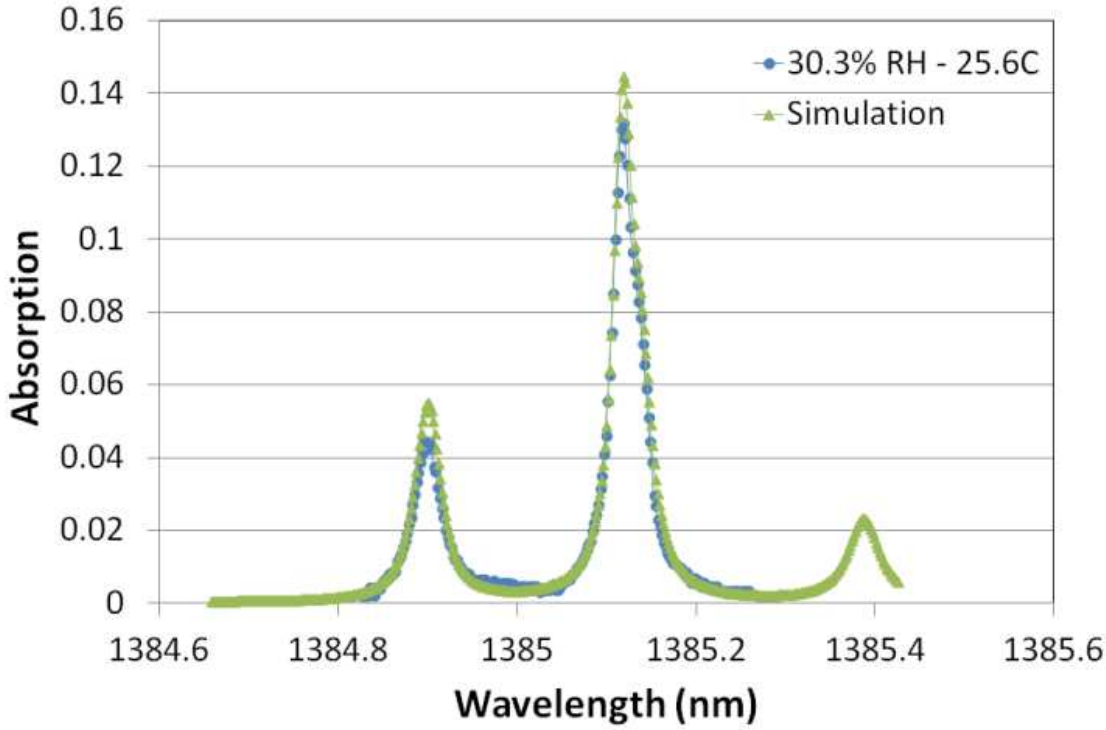

(c)

Figure 5.12 Measured water absorption spectra in the 1385 nm region for (a) 300 kHz, (b) a narrow part of the spectrum in (a), around the selected peak absorption, and (b) 500 kHz modulation frequency.

5.6 **Summary**

A scanning wavelength approach has been used here in order to assess the newly developed scheme. Two DFB lasers were current-tuned with a triangle ramp about the selected absorption features and external high frequency intensity-modulation has been applied on the sawtooth signal. A controlled laboratory demonstration on atmospheric air humidity showed excellent agreement between simulated and measured absorption lines. Strong etalon effects appeared in the detected signal when it was captured with multimode fibres, were eliminated by using bare photo-detectors. A real-time wavelength tracking scheme with a fibre-ring resonator has

been also developed for accurate wavelength mapping of the time domain reordered signal.

Chapter 6

Fixed-Wavelength Water Absorption Measurements

Having successfully demonstrated in Chapter 5 the scanned-wavelength water vapour absorption measurement, it is attempted in this Chapter to measure water concentration and temperature with the fixed-wavelength multi-colour approach as described in Chapter 3. A preliminary implementation of this scheme on an optical engine is also presented here.

6.1 Single-Channel Ratiometric Temperature Measurement

6.1.1 *Optical setup and data acquisition*

The experimental setup for the laboratory demonstration is shown in Figure 6.1. Since all three lasers in this scheme are operated at a fixed-wavelength, the fibre ring resonator sub-system was removed from the system shown in Figure 5.1. The launch side of the scheme is described in section 4.2.6. The two resonant laser beams are tuned to the selected absorption peaks and the non-absorbing reference at the water absorption-free 1310 nm area. The switching frequency between the two absorbed wavelengths in this case was 2 kHz. The power levels of the multiplexed modulated signals have been intentionally chosen to be different so they can be easily distinguished. The TDM Signal Adjustment Circuit generates a periodic step between the two SOAs based on a zero-crossing counter of the 500 kHz waveform. Figure 6.2 (a) shows the oscilloscope trace measured using a photodiode receiving the three-wavelength dual-frequency multiplexed beam.

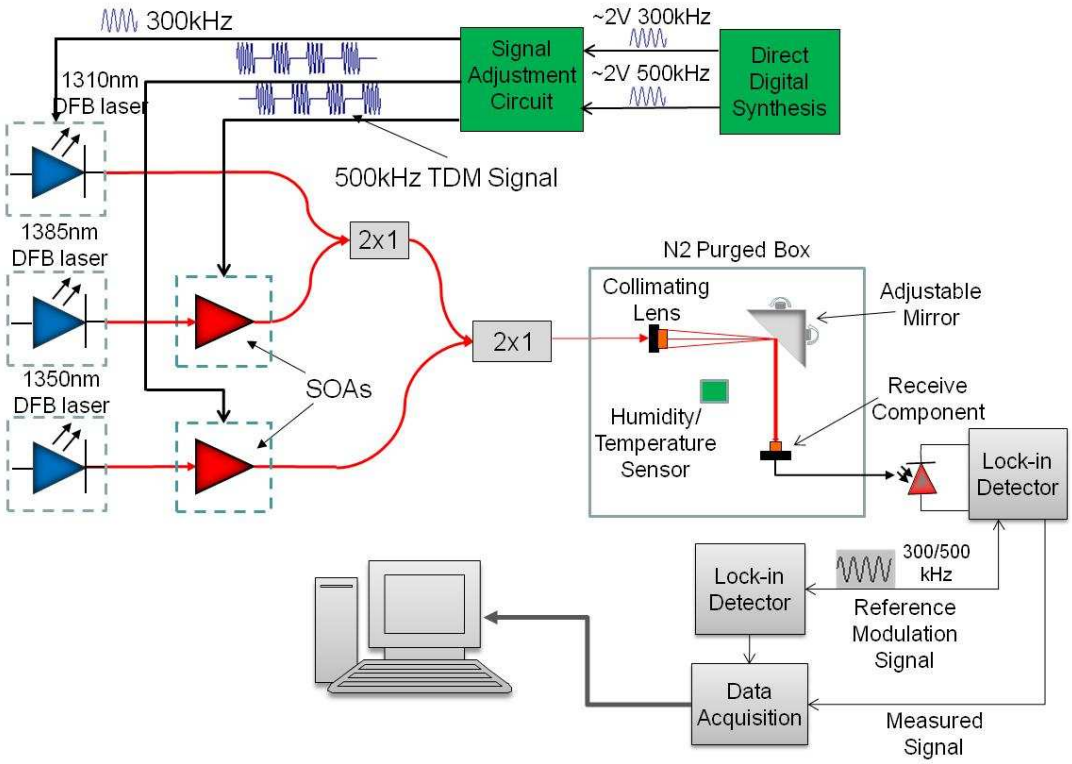

Figure 6.1 Fixed-Wavelength Time-Division-Multiplexing Experimental Setup

The near-square waveform shown in Figure 6.2 (b) is the demodulated TDM measured transmission signal obtained after traversing the 20 cm water-containing path in Figure 6.1; the high level of the square-wave is the 1350 nm signal, and the low level is the 1385 nm signal. Figure 6.2 (c) shows the same waveform when the water in the absorption path is purged by a nitrogen flow. The measured demodulated signal for the reference wavelength (1310 nm) is shown by the near-constant trace in each of the latter two Figures, showing that the non-species attenuation along the transmission path is very similar in each of the two conditions. The magnitude difference of the two square-wave signal levels in Figure 6.2 (b) and (c) are purely due to the H_2O vapour absorption-related attenuation of the non-purged signal. The average value of the higher and the lower level of this series correspond to the fixed-wavelength transmission of the selected transitions, and their ratio can be used to infer the averaged path temperature and hence the water vapour

mole fraction as described in Section 2.4. The periodic spikes on the reference signal are due to electronic noise from the driving TDM circuit and can be minimized with appropriate filtering and data processing.

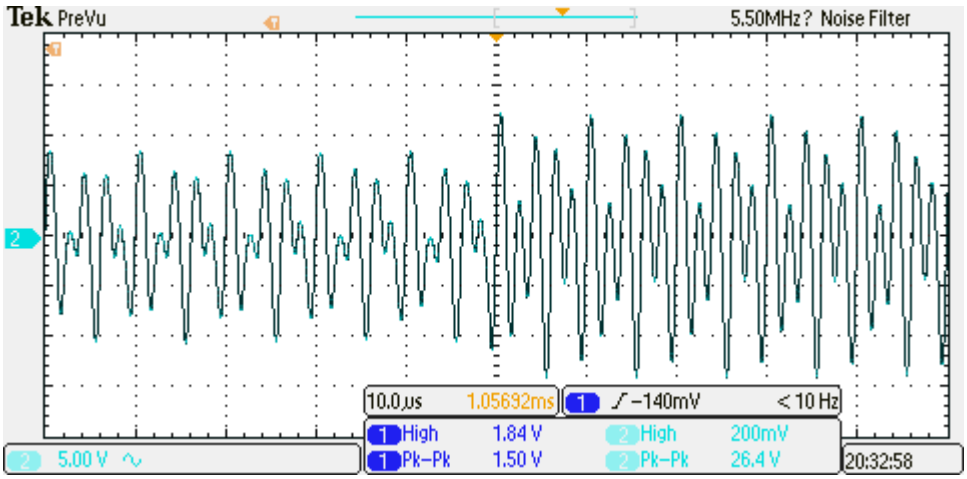

(a)

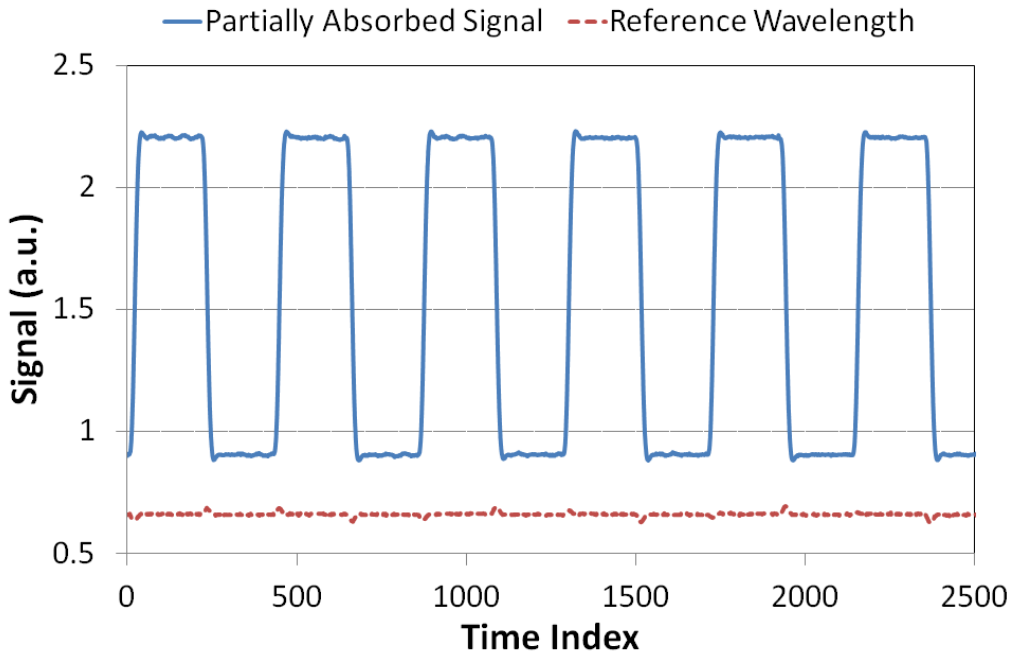

(b)

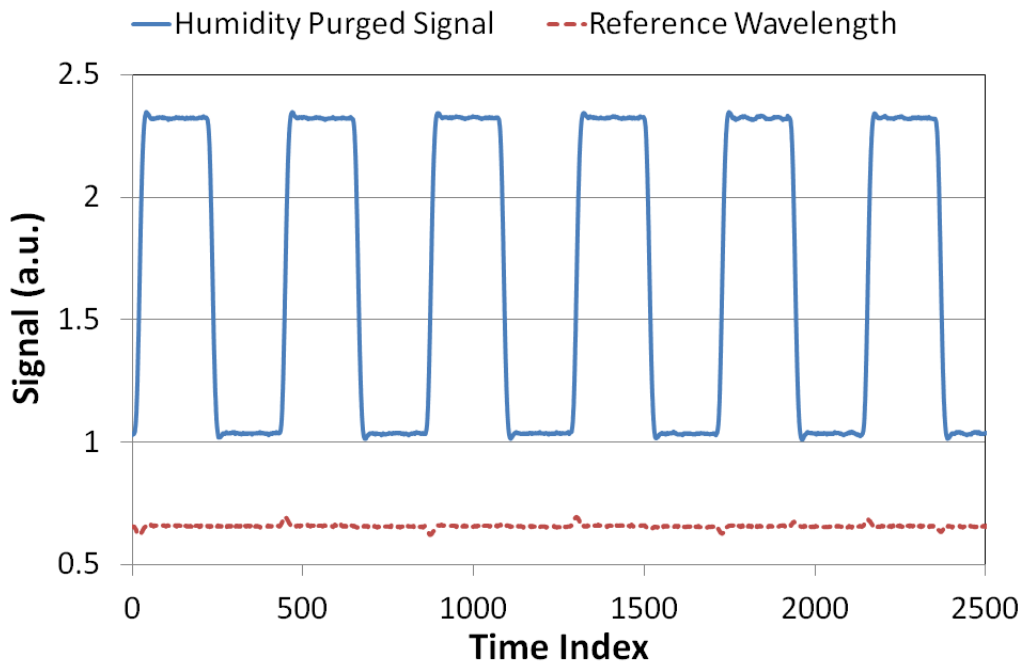

(c)

Figure 6.2 a) A screen-shot of the multiplexed modulated signals for 2 kHz switching frequency, b) demodulated recovered signal and reference wavelength for 25.7% RH and 26°C (switching frequency 2.5 kHz), and c) same signal under purge humidity conditions

6.1.2 *Fixed-wavelength data analysis*

Figure 6.3 a) shows a number of peak absorption measurements for each of the selected wavelengths taken under room temperature (~25°C) and different Relative Humidity (30-50%) conditions. Similar to the scanning wavelength approach, the relative absorption values are the ratios of the absorbed signal and the maximum transmitted signal which is measured under purged humidity conditions as discussed in Section 5.3. The recorded temperature and RH obtained from the Sensirion sensor have been used to simulate the peak absorptions as described in Section 5.5. As it can be seen in Figure 6.3 (a) the difference between the measured and simulated relative absorption values for both wavelengths is maximum 0.01 which suggests

that the measurement accuracy is better than 1%. The error in these measurements is mainly attributed to electronic noise in the detection circuit and the 3% absolute error of the RH/temperature sensor used for the simulation. Figure 6.3 (a) also shows linear fits to the measured data and the simulated data. By taking the absorption ratio of the two wavelengths with known pressure, a temperature map similar to the one shown in Figure 3.5 can be created.

Figure 6.3 (b) shows the measured and simulated two-wavelength absorption ratios as a function of concentration (mole fraction), taken for different RH values. These data correspond to the first point (300 K, 1 Atm) in Figure 3.5 with slight variations in absorption ratio, since the room temperature during the experiments was not constant (24 - 25°C). Thus, as explained in Chapter 3 the calculated absorption ratio of the measured wavelengths is independent of the actual species mole fraction, and for known pressure, the temperature can be estimated without knowing the actual species concentration. Subsequently, with known temperature the gas concentration along the optical path can be calculated using the Beer-Lambert equation for either of the two wavelengths used. As it is shown in Figure 6.3 (b) the absorption ratio deviation between measurement and simulation in less than 0.03, which gives an about 3% relative error. This is the first demonstration of temperature estimation with the newly developed system and indicates the great potential of the technique. With modifications of the detection electronics such as improved receiver bandwidth for the TDM signal, and more accurate temperature control of the diode lasers, even better accuracy can be expected.

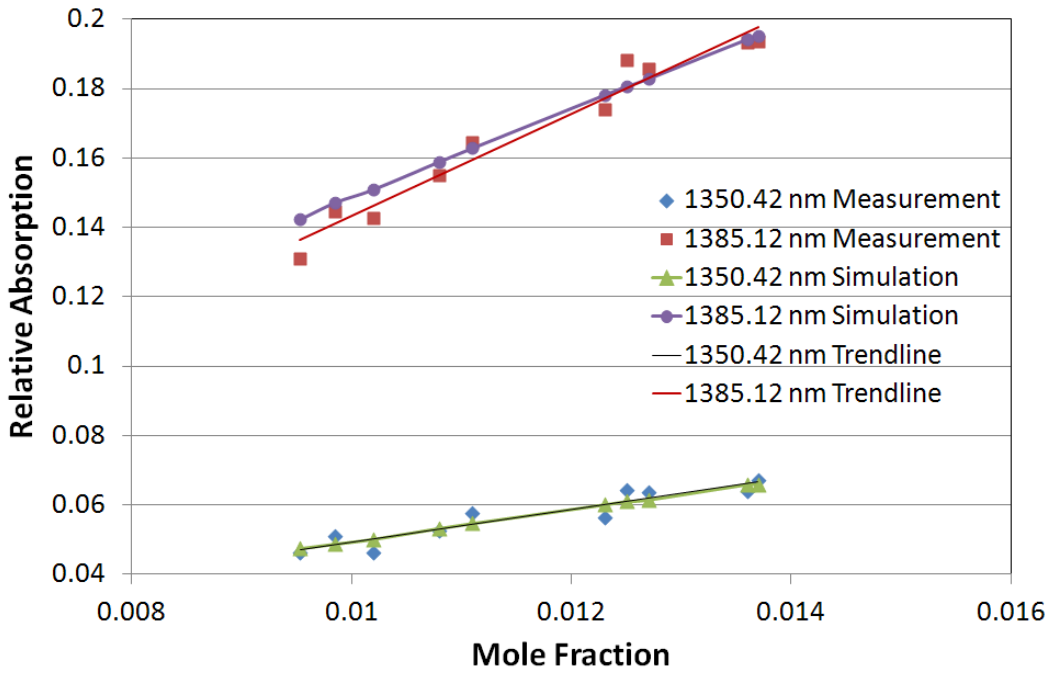

(a)

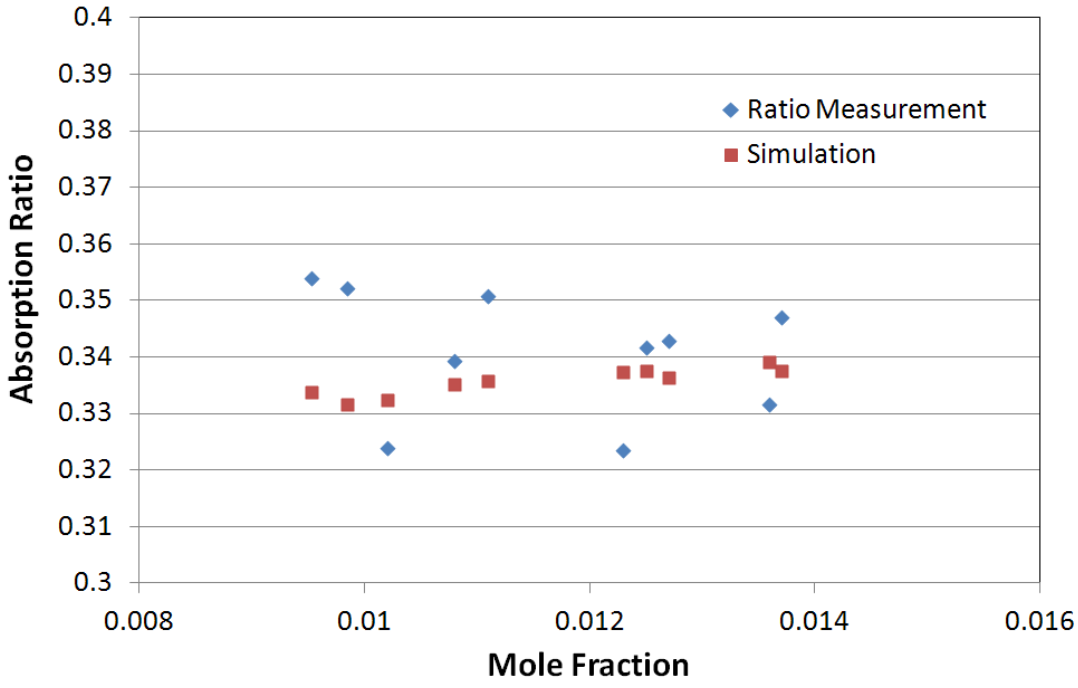

(b)

Figure 6.3 a) Peak absorption data for different conditions of H_2O concentration and temperature both measured and simulated, along with linear fits, and b) the corresponding two-line absorption ratios ($A_{1350.42\ nm}$ / $A_{1385.12\ nm}$).

6.2 **Multi-Channel In-Cylinder Water Absorption Measurement**

A number of preliminary tests of the newly developed scheme have been performed on an optical IC engine. The main objectives of these tests are to evaluate the new scheme, to identify the main technical challenges and to determine the potential for tomographic image reconstruction measurements. As it has been mentioned earlier, Intake and Compression strokes are of particular interest since humidity distribution into the chamber can be used as a marker for mapping of residual gas from the previous cycle. During the Power stroke for fired engine operation the temperatures develop into the chamber could be as high as 2000 K and there are not validated spectroscopic data available at these conditions. Due to time and budget restrictions, this work mainly focused on qualitative investigation of the proposed scheme and not on quantitative high-accuracy measurements. In collaboration with the Sir Harry Ricardo laboratories at the University of Brighton, under the supervision of Dr Steven Begg, a series of H_2O absorption measurements have been carried out.

6.2.1 *Optical engine configuration*

A single-cylinder Ricardo Mk4 Hydra optical engine fitted with a Gasoline-Direct Injection (G-DI) 4-valve Dual Overhead Camshafts cylinder head has been used for these experiments. An analytical report of the engine parts, mechanical setup and control can be found in [94] and brief description is given here. Optical access to the cylinder of this research engine is available through a quartz piston and a coated 45° mirror, and also through a 20 mm thick quartz annulus (optical liner) fitted below the cylinder head (Figure 6.4). The cylinder head used in the testing was a 4-valve poppet valve pent-roof designed by Ricardo Laboratories. The compression ratio of

this engine is 9.195:1 and its speed for varying loads was controlled by a dynamometer.

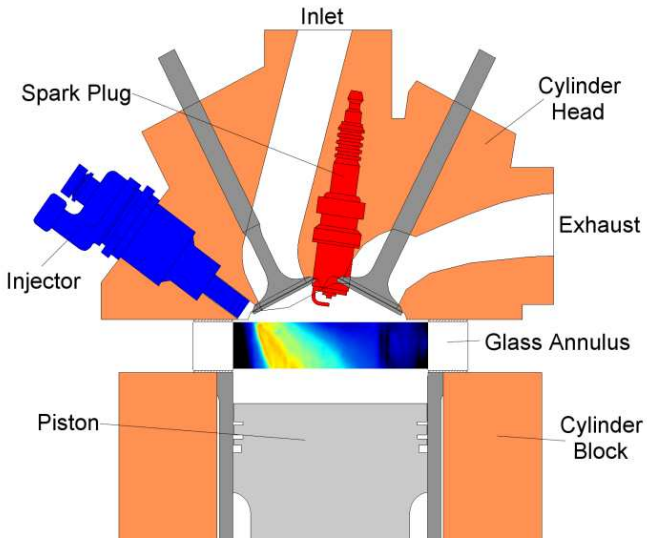

Figure 6.4 Cross section view of the Ricardo Mk4 Hydra optical engine [94]

The fuel injector used here was a single-hole, swirl type, Bosch C2 DI injector controlled by a Bosch injector driver box via the crank angle encoder, Z8 processor interface boxes and a Visual Basic-driven serial PC interface. The custom-built fuel rig consisted of a 5-litre tank feeding a low-pressure circuit driven by a standard Port Fuel Injection (PFI) pump at a pressure of 1.25 bar. This in turn fed a G-DI pump coupled to a conventional automotive fuel rail containing a pressure gauge for external monitoring. The fuel rail was also fitted with the conventional pressure transducer and solenoid valve to regulate injection pressure (95-100 bar). A standard Mitsubishi coil on plug system (Diamond FK0138) was used with NGK spark plugs driven by the encoder and the Z8 processor interface boxes and software.

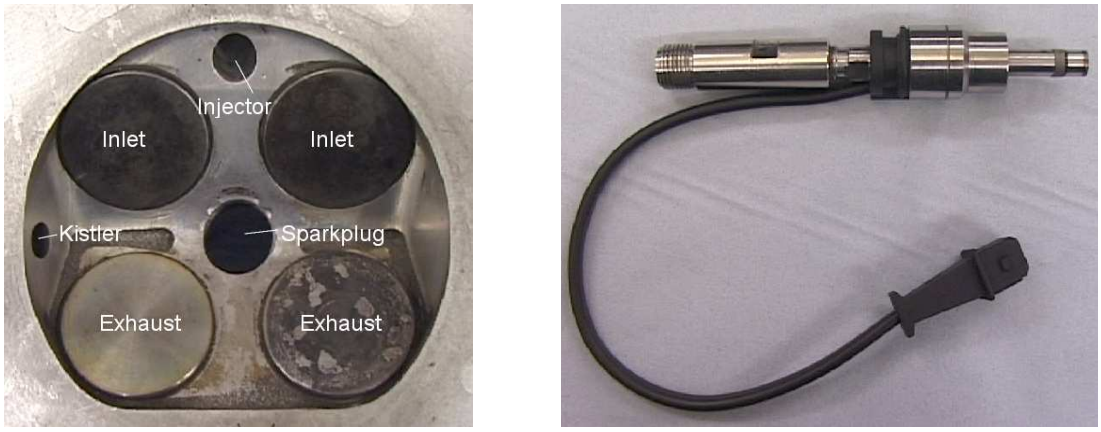

Figure 6.5 a) Pent roof of the cylinder head (injector, sparkplug and pressure transducer removed), and b) Bosch C2 injector

Throttle control was enabled by the use of a butterfly valve located at the entrance of intake plenum and driven via an interface board and potentiometer, using either a linear or logarithmic scale. Fine control of the butterfly valve was realised by using a DC motor coupled to a 100:1 ratio gearbox. Further fine-tuning was enabled by inserting one of a number or orifice plates, ranging in size from 2 mm to 5 mm, into the air stream before the butterfly valve. The use of a Kistler 4045A2 pressure transducer located in the plenum enabled the monitoring of IMAP through an MTS CAS high-speed data-logging system. Another Druck pressure transducer coupled to a digital display gave a read out of Internal Manifold Pressure (IMAP) for reference in the lab during testing. An ETAS lambda sensor (Lambda Meter LA4) was fitted to the engine to enable the monitoring of the Air-Fuel-Ratio (AFR) during engine operation.

6.2.2 *Engine measurement opto-electonic setup*

The fixed-wavelength approach described in Section 6.1 was used for the engine demonstration tests and the opto-electronic setup used is the same as that in Figure 6.1. Additionally, the multiplexed signal was split into three channels before being pitched through the optical liner in order to obtain three different beams that were

pitched at different angles across the cylinder. The number of the beams used was chosen based on the physical limitations and the size of the mounted collimators and detectors around the engine. The optical arrangement of the beam collimators and the photo-detectors are depicted in Figure 6.6. In order to investigate how the beam angle of incidence to the normal to the optical liner affects the data quality, one beam was placed in a near-diametric position (i.e. about 360° angle) and the other two were placed at a larger angles relative to the normal. The optical collimators and detectors used here are the same type as those used for the laboratory measurements and were mounted on an optical bench and a set of four rails which were firmly bolted on the floor isolated from the engine, in order to eliminate effects due to engine vibrations. The mounting elements were placed at the highest possible point on the optical liner, so that the beam blockage period in the 4-stroke cycle due to the piston is kept to a minimum. All optical mounting components were placed and tightened on an optical bench, which was rigidly bolted on the floor detached from engine vibrations.

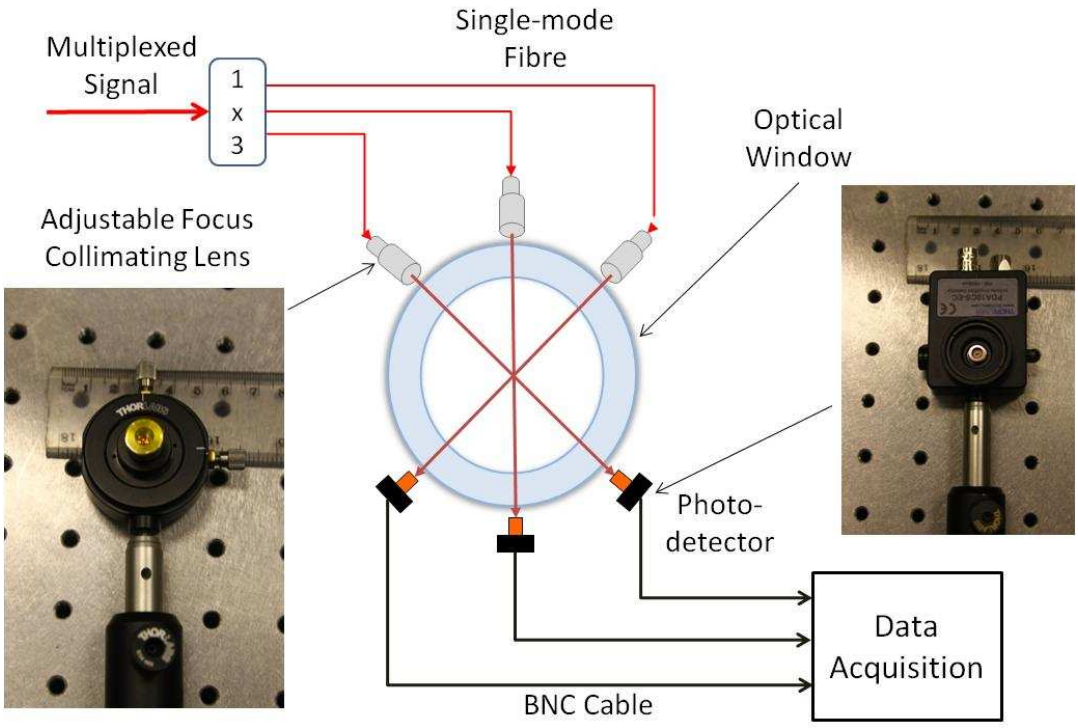

Figure 6.6 Top view of the physical arrangement of the transmitting/receiving elements around the optical window.

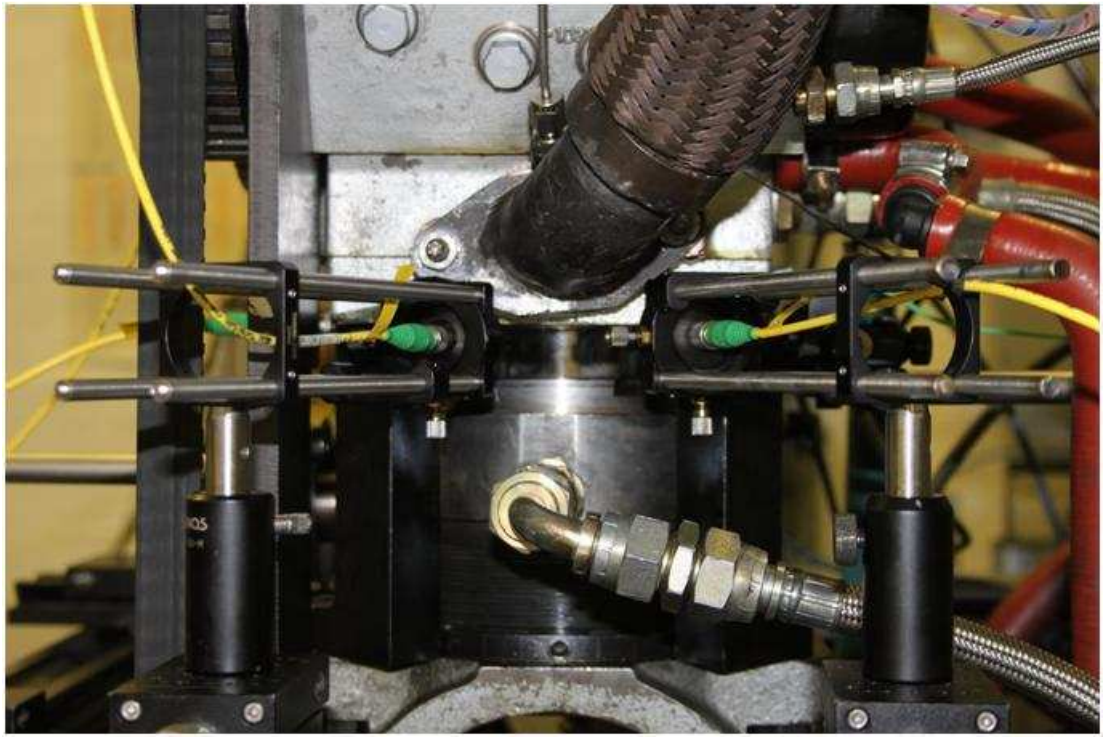

Figure 6.7 Optical components mounted around the engine

In the laboratory demonstration of the fixed-wavelength scheme presented in Section 6.1, a 1310 nm diode laser was used to account for non-absorbing related attenuation, since this wavelength region is water-absorption free. Unfortunately, during the engine tests the 1310 nm laser diode failed unexpectedly and due to the strict time limitations of these experiments, it was necessary to employ an alternative non-ideal approach. The only available alternative at the time was a back-up 1385 nm tunable diode laser. The main concern with that laser though was that, the 1385 nm region is interspersed with several water absorption features (Figure 3.1) and tuning it to a completely absorption-free area is not possible. The entire tuning range of that diode was experimentally examined through temperature and bias current control, and the absorption lines present in that area were examined through the spectral databases. It was found that the optimum wavelength regions that this diode could actually be tuned to the minimum water absorption were at about 1384.2 and 1384.5 nm. As shown in Figure 6.8 the absorption at this wavelength range only locally exceeds 3% even at elevated temperatures and pressures.

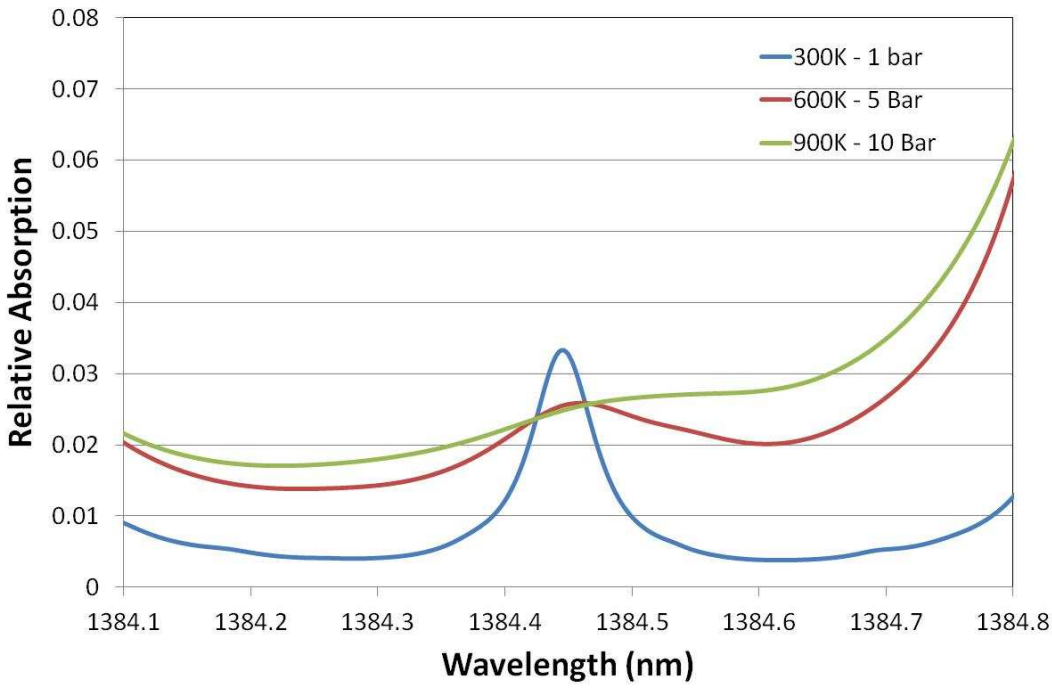

Figure 6.8 Wavelength modulation range of the 1385 nm reference diode laser

The reason for having this relatively large tuning range is that this DFB diode laser is directly modulated with a high-frequency signal, which means that the wavelength was also modulated. Moreover, the modulation amplitude had to be large enough so that the lock-in circuit could detect the fundamental harmonic. Another problem that has arisen with the replacement reference laser was with the multiplexer. This was a WDM-type multiplexer which turned out to be wavelength selective for each input port. Thus, the input port for the 1310 nm could not be used for the 1385 nm replacement laser. An extra 2x2, 50/50% optical coupler had to be used to add that emergency reference wavelength, which introduced significant loss to the power budget of the system, especially for the new 1385 nm reference wavelength. To mitigate against that loss, 10 dB gain was added to the thorlabs PDA10CS switchable detectors reducing the channel bandwidth to 75 MHz, which is still well above the bandwidth requirements of our system.

6.2.3 *Unfuelled Motored Operation*

In the first stage of the experiments the engine has been tested in a non-fired, motored operation mode at 1000 rpm. All measured and monitoring signals were recorded by the Baseline Adapt CAS data acquisition system in a time-based logging mode at 150 kS/s per channel, including the in-cylinder pressure, the Manifold Pressure (MAP). The duration of the measurement was set to 14 seconds meaning that about 116 full four-stroke cycles were recorded at 1000 rpm in each experiment. All recorded data were logged on a single csv file and subsequently processed and analysed with MATLAB. For the motored-engine case the continuously recorded data were separated into individual cycles based on the encoder signal [Appendix D].

Figure 6.9 shows a sample of the data recorded during a full 4-stroke for each channel. The figure includes the TDM-absorbed signal, the reference wavelength signal, the MAP signal as well as the in-cylinder pressure variation during the cycle. The MAP trace is used to calibrate the actual in-cylinder pressure. Due to the rapid switching rate (~2°CA) of the TDM signal of the two resonant wavelengths, the trace is very condensed in the full cycle graphs, and thus it appears as a thick single line. As it is shown bellow, it is a varying amplitude square-wave signal with the higher and lower levels representing each resonant wavelength. The apparent gaps on the logged measurement signals are due to the optical beam blocking by the piston as it reaches TDC. In particular, Channel 1 is blocked from about 46 °CA before and after TDC, whereas Channels 2 and 3 are blocked for about 54 °CA, since they were placed slightly lower on the optical liner. This difference between the heights of the projections was due to mechanical limitations of the optical elements. The power

offset of the detection electronics has been subtracted from the absorbed and the reference signal prior to the data analysis, as in the laboratory experiments.

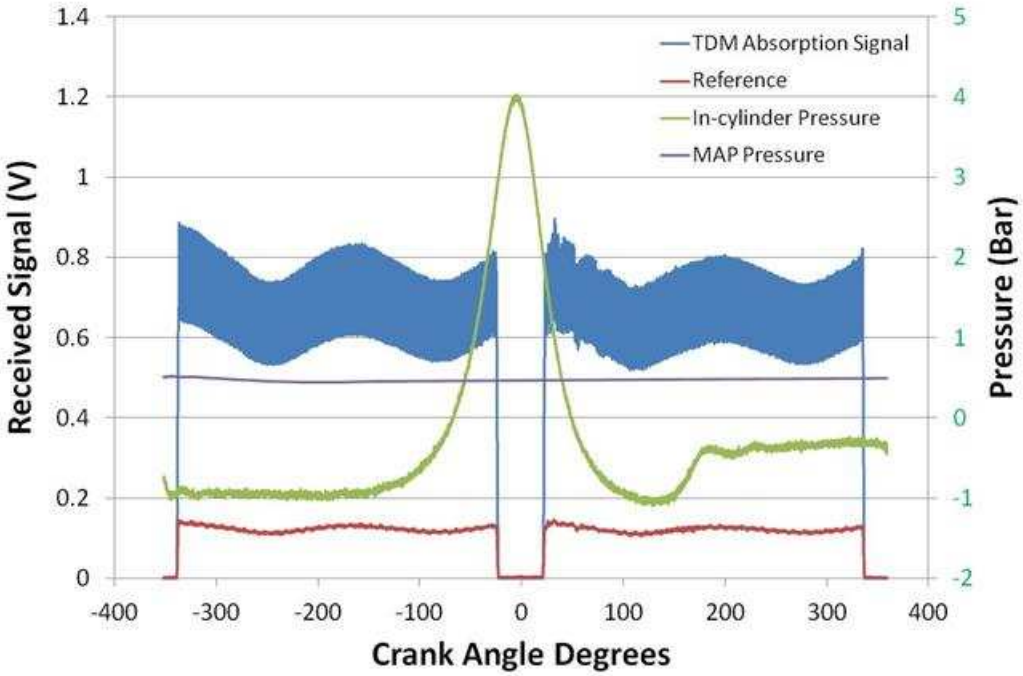

(a)

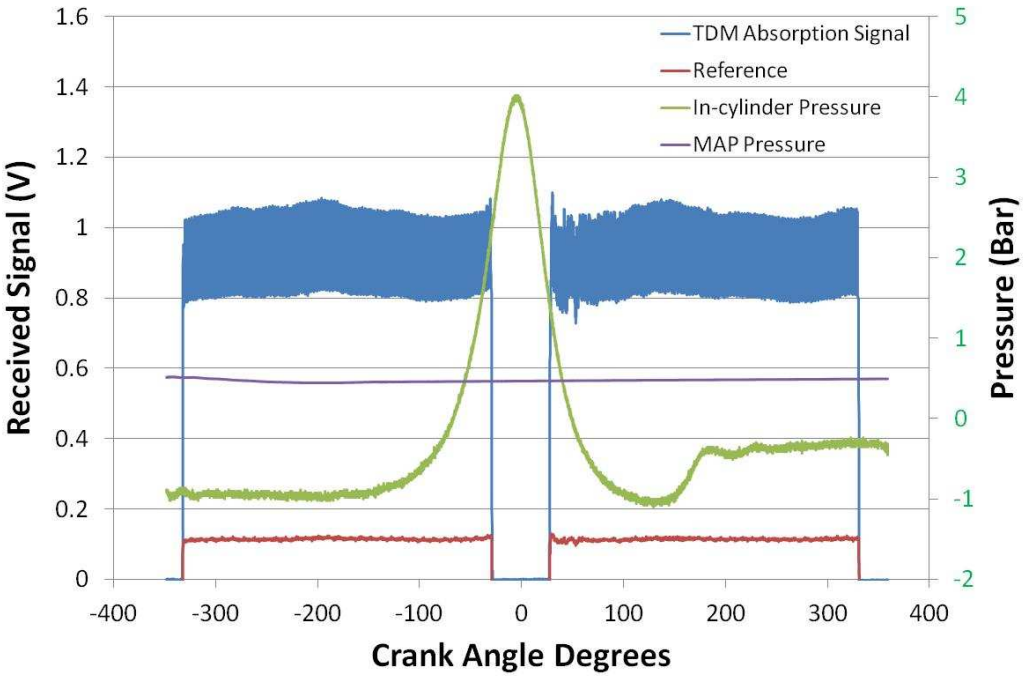

(b)

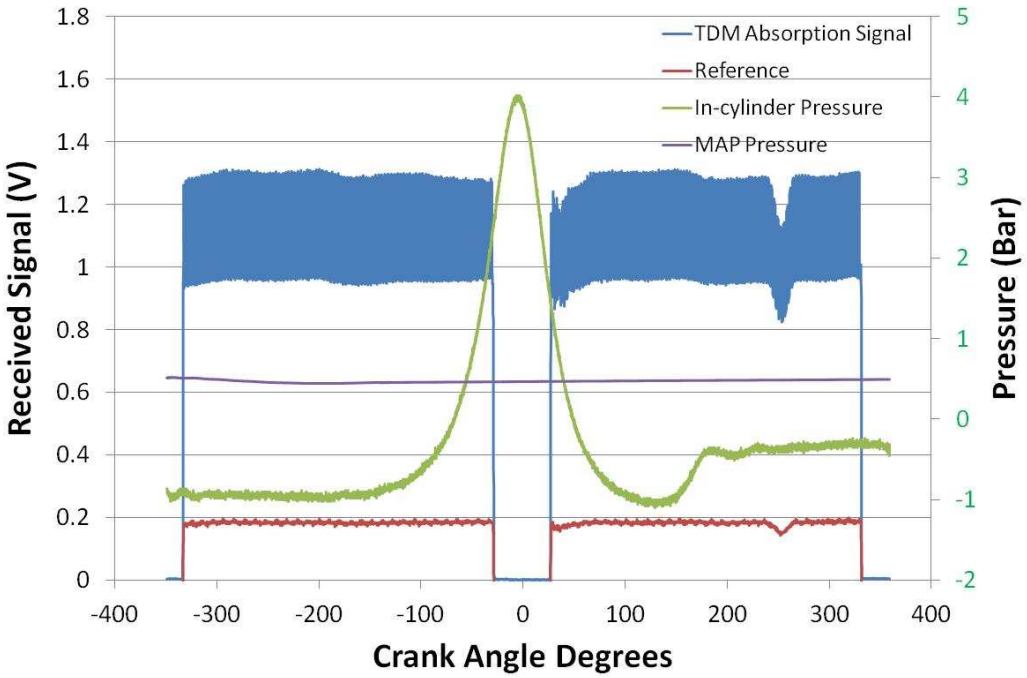

(c)

Figure 6.9 All captured data for a single cycle of the motored engine operation plotted against the °CA encoder signal for a full 4-stroke cycle for a) Beam 1, b) Beam 2 and c) Beam 3

As can be seen in Figure 6.9 the Beam 1 signal is subject to a periodic intensity variation which is repeatable in each cycle. This periodic oscillation was highly dependant on the engine speed which suggests that it can be attributed to a resonating mechanism related to the engine vibration. This oscillation does not appear on the Beams 2 and 3, probably due a slight optical mounting mismatch amongst the three beams. As can be seen in Figure 6.10 (a) and (b) the non-absorbing reference signal for each channel is subject to similar intensity oscillation during the engine cycle and thus it can be used to normalise the intensity fluctuations of the TDM signal. Nevertheless, due to the non-ideal non-resonant laser as explained in Section 6.2.2, the reference intensity is considerably weaker than the

absorbed signal, and it is also subject to a high frequency electronic noise which makes normalisation problematic. For that reason a post-processing digital filter has been composed in MATLAB to de-noise the reference signal. This filter consists of one 2nd order Butterworth Low-Pass-Filter cascaded with a 2-stage median filter [Appendix E] and the resulting filtered signal is shown in Figure 6.10 superimposed on the recorded noisy reference signal. The smoothing effect of that filter is more clear in the second graph.

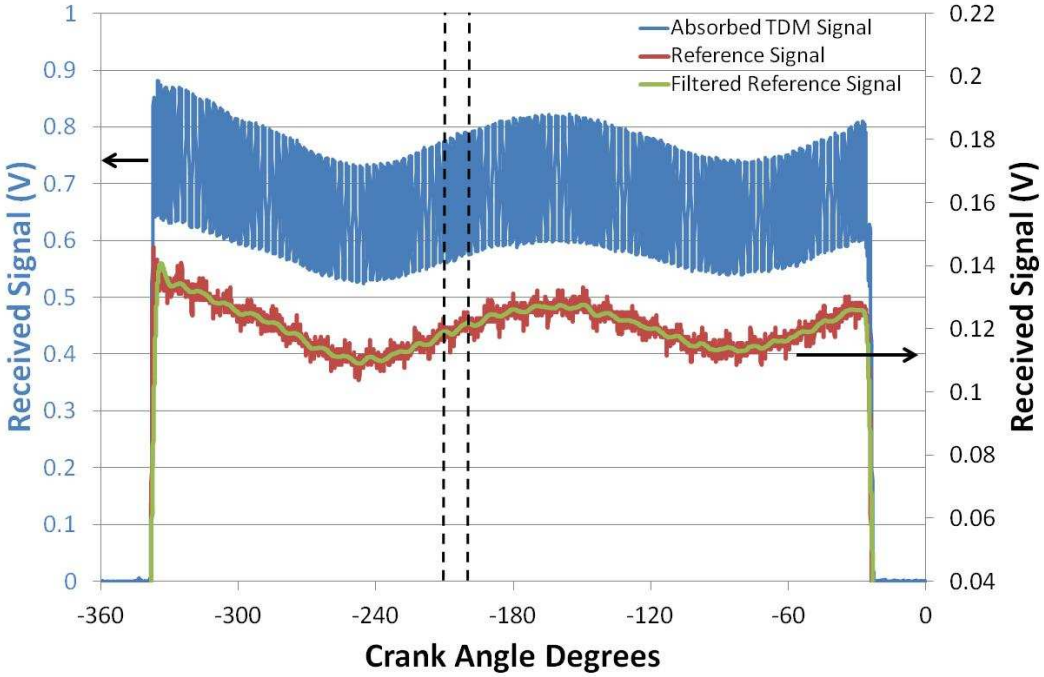

(a)

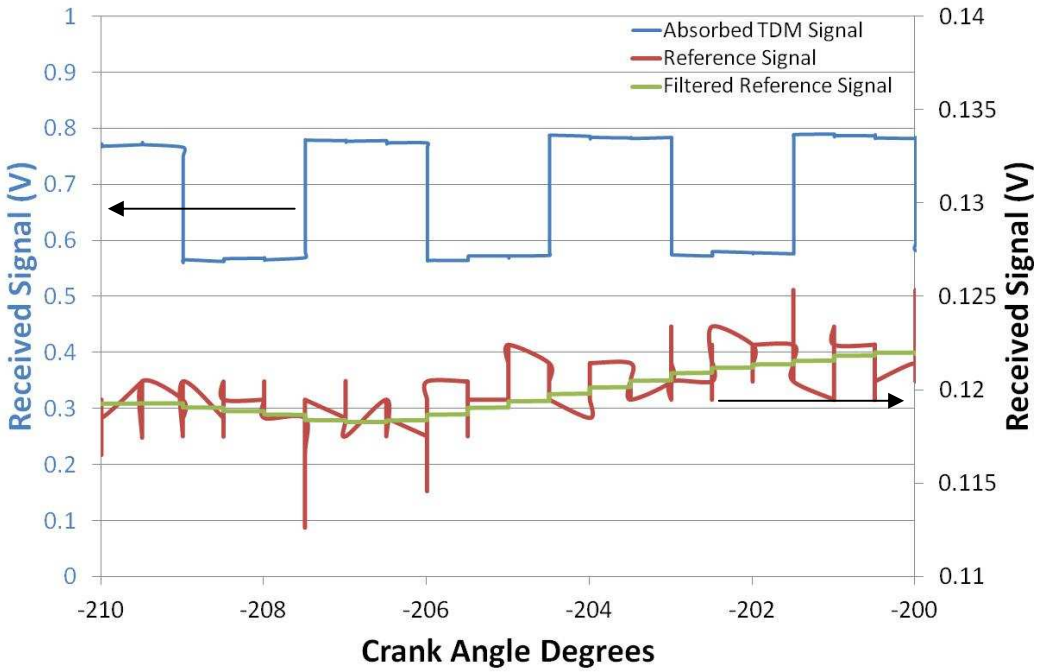

(b)

Figure 6.10 Measured TDM-absorbed signal and the original and de-noised version of the reference signals for a) half cycle, and b) for the 10 °CA subsection indicated with dotted lines in a).

The resulting TDM signal normalised by the filtered reference is shown in Figure 6.11 along with the in-cylinder pressure variation during the full cycle. Closer inspection of the 2-colour absorption signal reveals augmented noise effects during the power stroke, immediately after the piston blocking of the beam. This noise is mainly attributed to beamsteering effects due to rapid pressure variation and in-cylinder temperature gradients at that instant. Similar to the laboratory demonstration in Section 6.1, the higher level of the TDM signal corresponds to the 1350nm wavelength and the lower level to 1385nm. For the separation of the two wavelengths, a MATLAB code has been compiled (Appendix F) which scans and identifies the local maximum and minimum regions (or valleys) by calculating the

variance of a pre-defined consecutive number of points. Setting a limit for the minimum acceptable value of the variance, the intermediate points between the high and low level were rejected. The envelope curves are then plotted based on the the mean values of the selected points and by linear interpolation between these peak areas. An example of the resulting TDM signal envelope separation is shown in Figure 6.12.

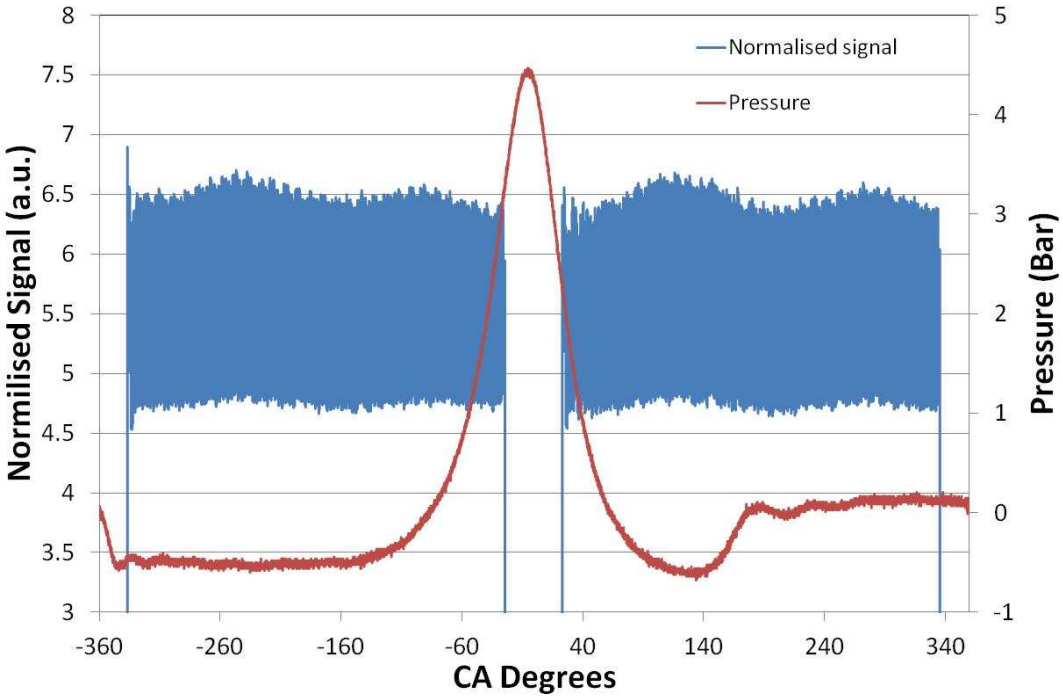

Figure 6.11 Measured Channel 1 signal normalised with the filtered reference and in-cylinder pressure.

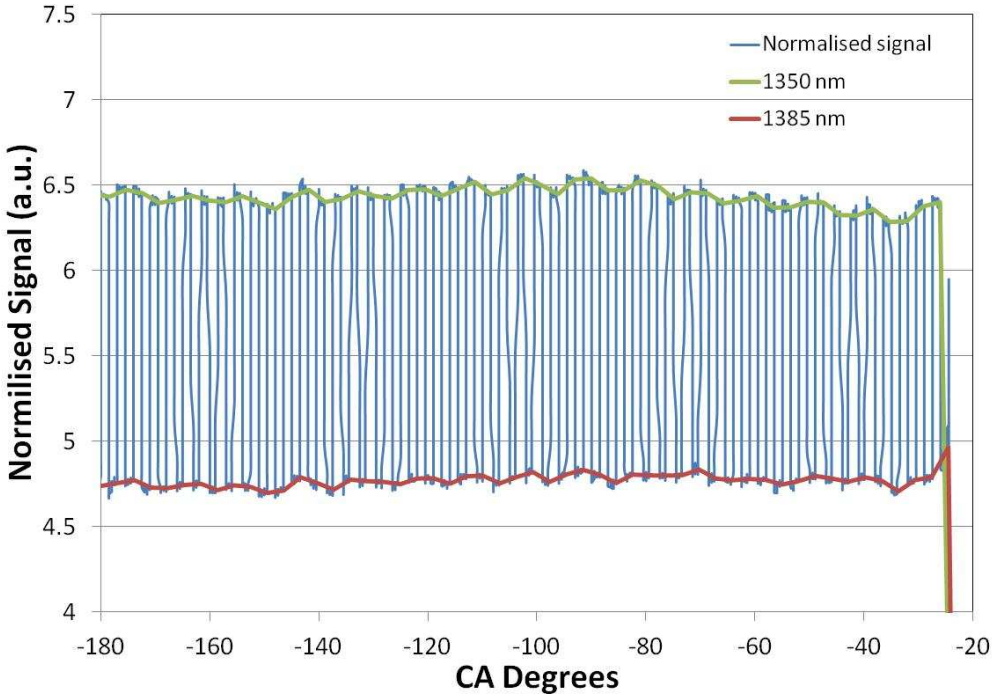

Figure 6.12 Wavelength separation of the TDM signal with the high level envelope correspond to 1350 nm and low level to 1385 nm.

Figure 6.13 shows the resulting separated normalised levels correspond to the two wavelengths, and the resulting 1385 over 1350 nm transmission ratio during one cycle. The two levels are then further smoothed with a dual-stage Median filter and the resulting ratio of the filtered signals is also shown on the same graph. As it can be seen in Figure 6.13 the falling piston at -340 °CA unblocks the beam, and in the remainder engine intake stroke, the two transmission signals show significant variation as does the ratio between them. In order to calculate the in-cylinder temperature, and subsequently the water vapour mole fraction, the measured traces should be calibrated against a reference point, which is usually about -180 CA° at BDC where the in-cylinder pressure and temperature have their minimum values. If the beamsteering effects are also to be taken into account the calibration should take place at every °CA point in the cycle at the same conditions, but with no-absorber present (i.e. dry air into the injector), which in practice is very difficult to achieve.

Here, due to the non-ideal experimental conditions and the poor signal referencing, the signal distortion due to non absorption related noise could not completely eliminated in order to produce accurate quantitative data, and thus we focused on a qualitative analysis of the data.

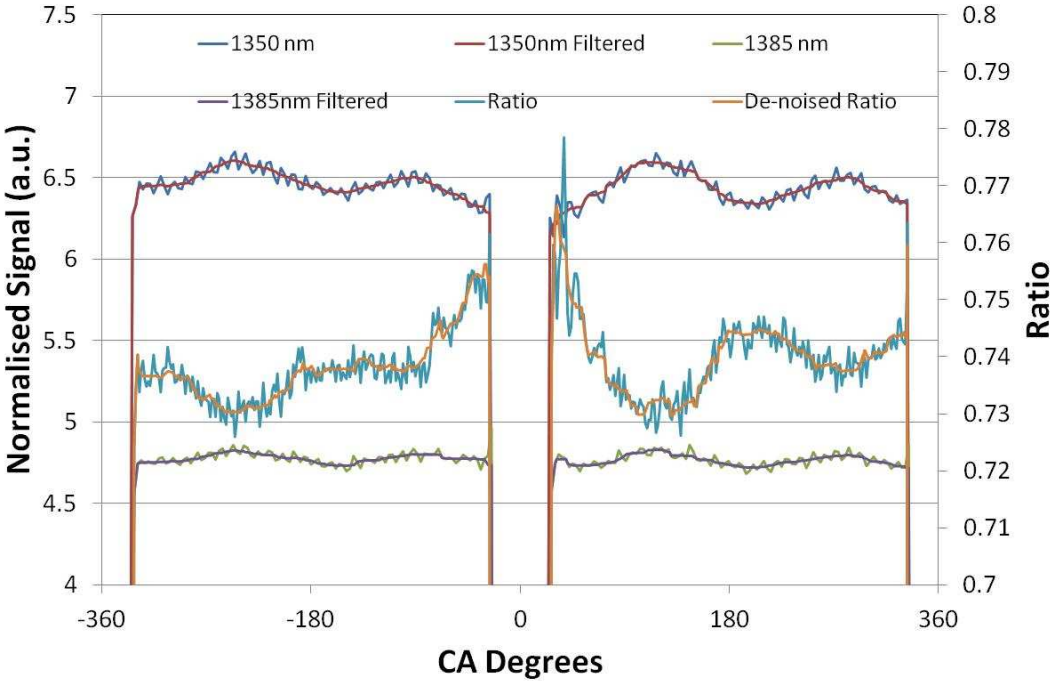

Figure 6.13 Separated normalised Channel 1 signal level before and after denoising and corresponding ratios

Figure 6.14 shows the averaged ratios of 116 consecutive motored cycles for the beams 1 and 2, plotted against the in-cylinder pressure, which was the same for each cycle. The four strokes of each cycle and the peak intake and exhaust opening positions are also shown. During the intake stroke it appears that the ratio is responding to the incoming cold gas and the variation of in-cylinder pressure to a value below atmospheric, while the mole fraction of water is expected to be constant. Figure 6.15 shows a simulation, based on spectral databases, of how the transmission ratio of the selected wavelengths changes with temperature and pressure, for constant mole fraction. Based on these curves both of the thermodynamic changes during the

intake stroke would be expected to cause the transmission ratio to fall, as it is indeed can be seen around the intake valve peak opening region (i.e. -253 °CA). Also, based on that simulation, the two-colour transmission ratio of the selected lines is expected to rise when pressure and temperature are increasing for constant mole fraction. This is indeed happening towards the end of the compression and on the beginning of the power stroke as temperature and pressure reach their peak values. A relative drop of the ratio can be observed towards the end of the end of the cycle when the exhaust valve is opening. The above observations are very good indicators for the qualitative evaluation of the acquired data, even though there is an evident mismatch between the actual ratios of the two channels. The latter suggests that a robust calibration approach is necessary in order to obtain accurate quantitative results.

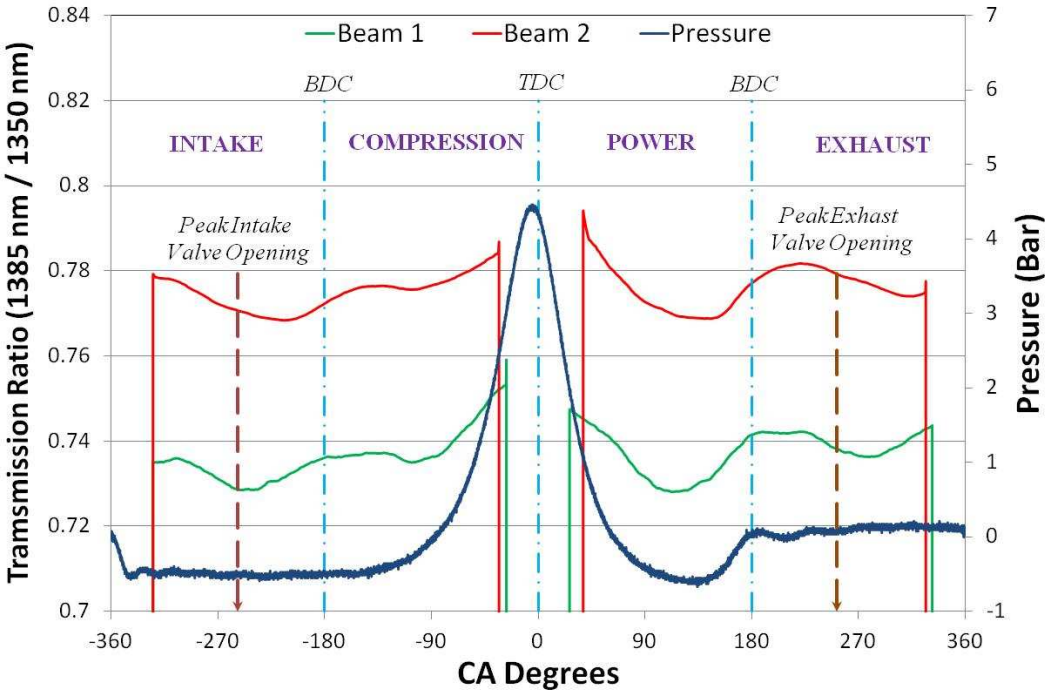

Figure 6.14 116 cycles averaged ratio for beams 1 & 2 versus in-cylinder pressure.

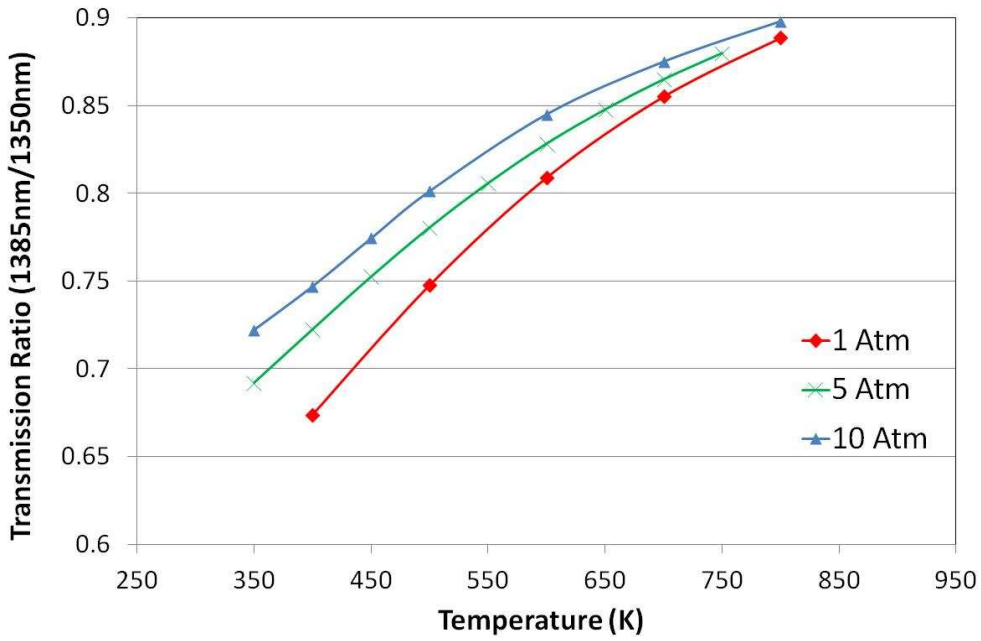

Figure 6.15 Simulated Fixed-Wavelength Transmission ratios for fixed 10% H_2O mole fraction, as temperature and pressure increases.

6.2.4 *Fired Engine Operation*

During the fired engine operation various combustion conditions were tested for different lamba air/fuel ratios and intake manifold throttle positions. Figure 6.16 shows the recorded raw data during a full cycle with air-to-fuel ratio 17:1 (lambda = 1.15). In comparison to the motored case described in the previous paragraph, Figure 6.16 also shows the fuel injector trigger signal during the intake stroke. The data processing procedure in this case was slightly different due to a fault on the encoder signal, which instead of resetting at every cycle (720 °CA), it was abruptly resetting during the cycle. The MATLAB code used to separate the data into individual cycles was based on the Injection signal and it is shown in Appendix G.

Figure 6.16 (b) corresponds to beam 2 and it can be seen that for the duration of the air/fuel injection it is apparently blocked. This is probably because beam 2 is inadvertently crossing just below the injector's nozzle, and when the mixture is

injected it almost completely blocks the optical path of the beam. Apart from a small drop to transmission signals' power level due to the window fouling, the general shape of the measured signals during the intake and compression strokes, are quite similar to the corresponding motored case signals show in Figure 6.9. Nevertheless, in the fired case the absorption-resonant TDM signal appears to be slightly 'squeezed' during the compression stroke since the mixture is introduced into the chamber and the water concentration is increased. As expected, the signals appear to be more distorted at beginning of the power stroke after the combustion which is due to the extreme thermodynamic change and severe beamsteering effects.

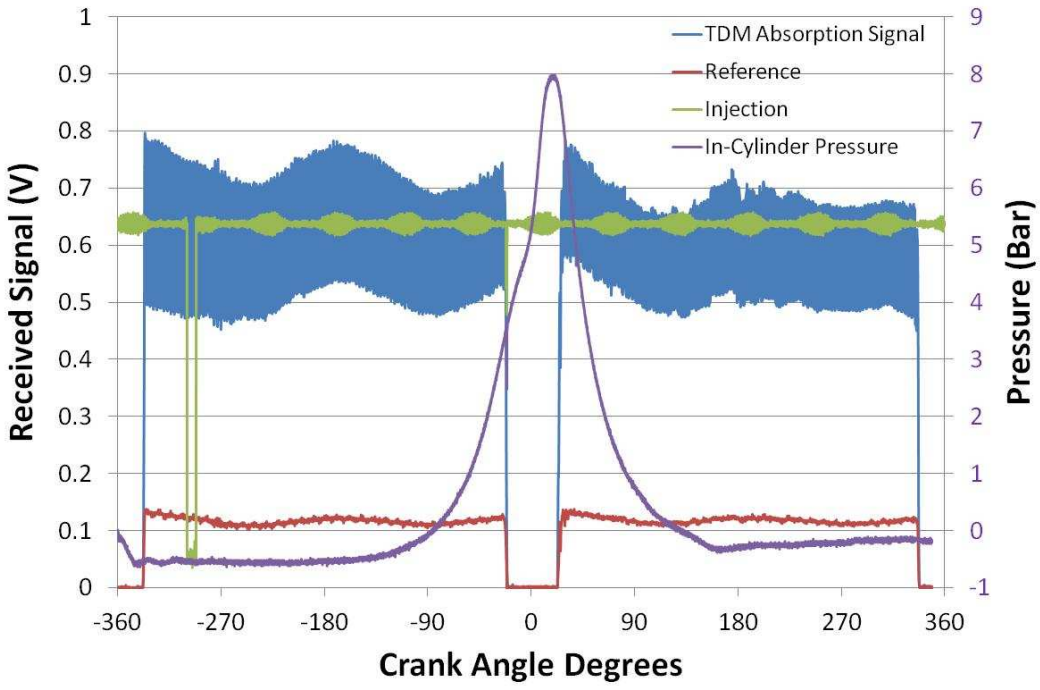

(a)

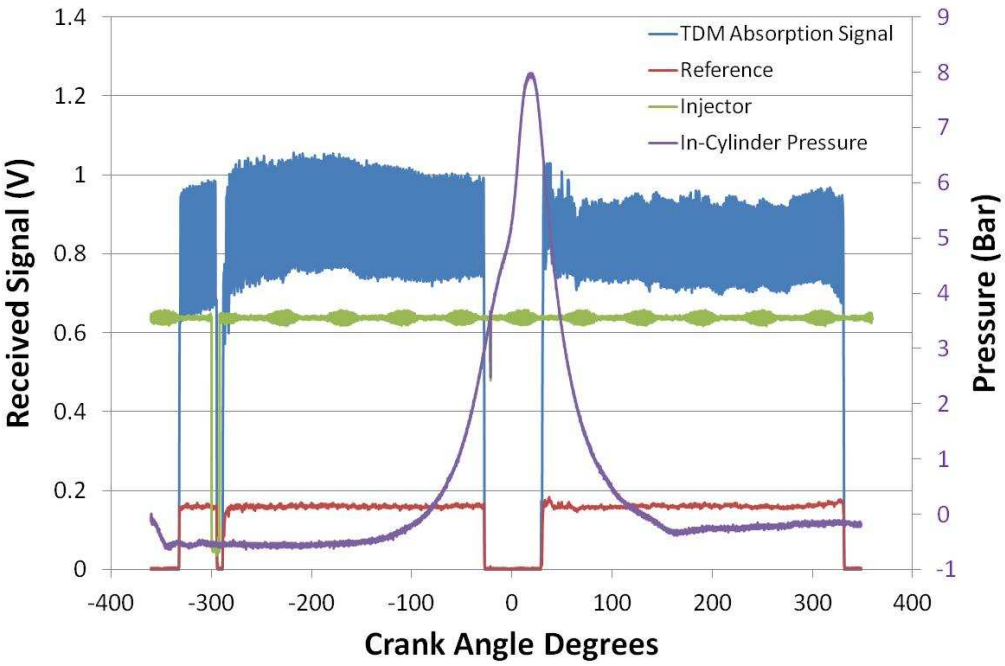

(b)

Figure 6.16 Recorded raw data for a single cycle during fired engine operation for a) Channel 1 and b) Channel 2. High pressure indicated open throttle position.

Figure 6.17 shows the separated signal levels (wavelengths) normalised by the reference signal and filtered following the same procedure as in the motored case. Similar to that case, as the pressure increases towards the end of compression stroke the two-wavelength normalised transmission ratio is also increasing as expected. Also the increment is more sharp in this case due to the introduction of the air/fuel mixture. During the Power stroke of the fired case however, there is an apparent rise on the low-level 1385 nm signal instead of a decrease, as it would be expected due to the absorption from the combustion-produced water vapour. This abnormal detected intensity increment is mainly attributed to the severe beamsteering effects due to the rapid pressure drop, and the resultant refractive index variation. Power stroke in fired operation is in general accompanied with extreme thermodynamic effects which need more thorough investigation before making any reliable measurements.

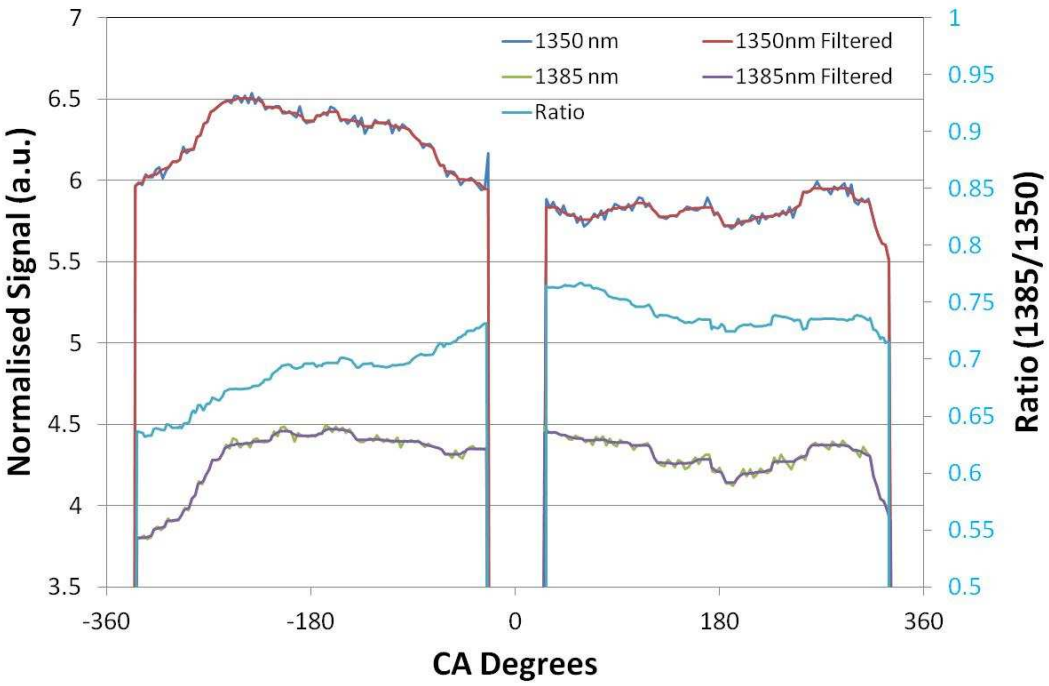
1350 nm
1350nm Filtered
1385 nm
1385nm Filtered
Ratio
Normalised Signal (a.u.)
Ratio (1385/1350)
CA Degrees
7
6.5
6
5.5
5
4.5
4
3.5
1
0.95
0.9
0.85
0.8
0.75
0.7
0.65
0.6
0.55
0.5
-360
-180
0
180
360

(a)

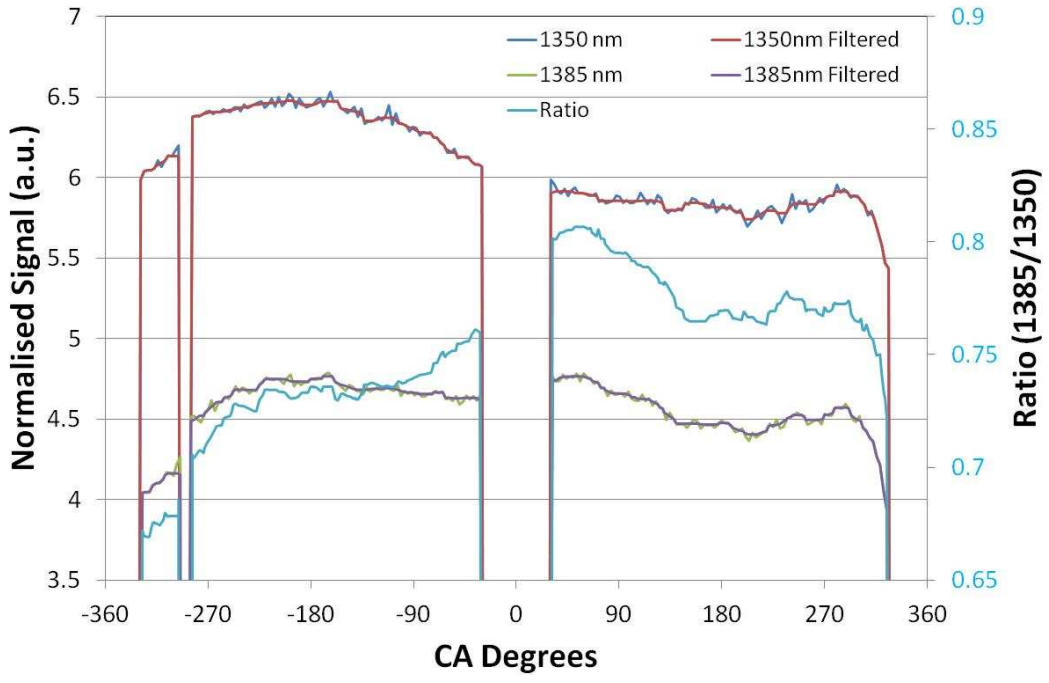
1350 nm
1350nm Filtered
1385 nm
1385nm Filtered
Ratio
Normalised Signal (a.u.)
Ratio (1385/1350)
CA Degrees
7
6.5
6
5.5
5
4.5
4
3.5
0.9
0.85
0.8
0.75
0.7
0.65
-360
-270
-180
-90
0
90
180
270
360

(b)

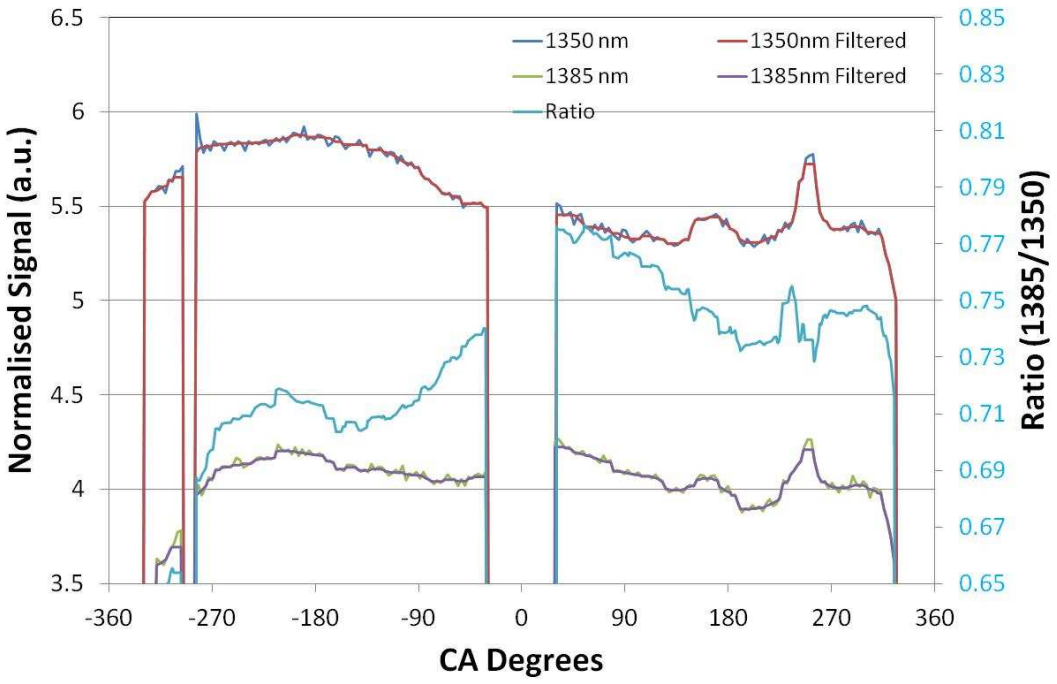

(c)

Figure 6.17 Normalised separated –wavelength signals and transmission ratio for a) Channel 1, b) Channel 2 and c) Channel 3

As it can be seen in Figure 6.18 the ratios of the three channels are behaving in a very similar manner throughout the cycle even though there are small differences in their amplitudes. Temperature non-uniformity could be one possible reason for intra-channel transmittance-ratio differences, especially during the intake stroke where the mixture is injected locally into the chamber. Averaging multiple cycles was not possible during fired operation because the inlet throttle position was changing during the experiment and that caused significant pressure variation between cycles. Nevertheless, the signals are in general consistent and repeatable in between cycles. All these observations suggest that a standalone non-absorbing wavelength referencing is not adequate calibration approach and that a more robust method is required in order to obtain a reference intensity of the transmitted signals and infer quantitative absorption measurements.

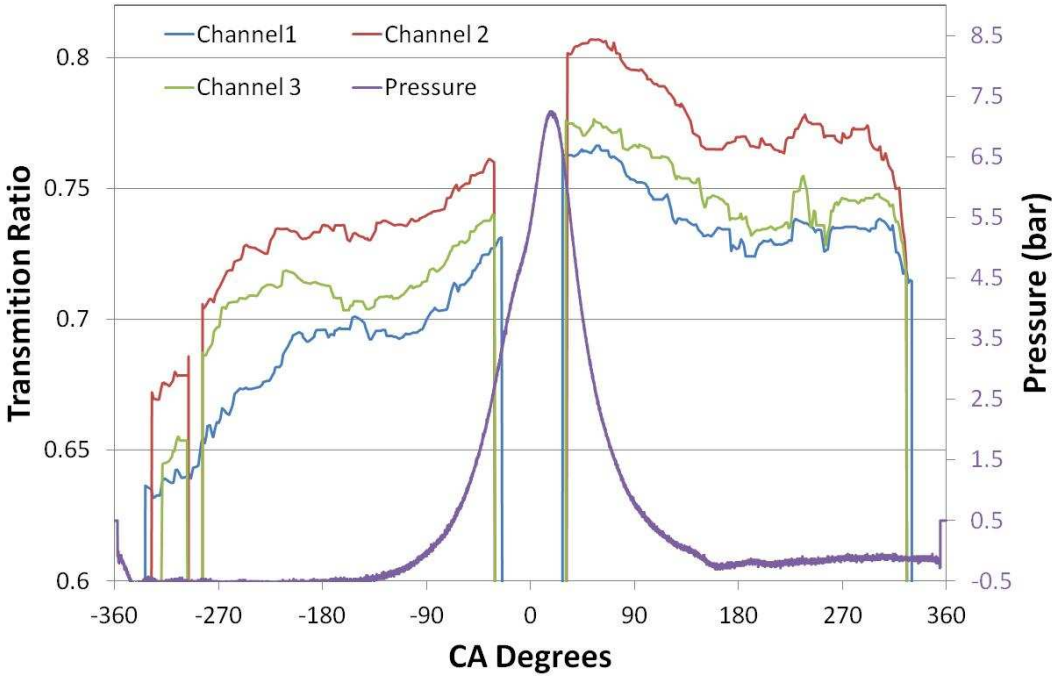

Figure 6.18 De-noised ratio versus in-cylinder pressure for the three beam projections during fired engine operation

6.3 **Summary**

In this chapter a fixed-wavelength, multi-colour, TDM approach tested for water vapour concentration and temperature estimation, both in the laboratory and on an IC engine. The system showed excellent performance in a controlled laboratory environment and very good agreement between simulation and atmospheric humidity mole fraction measurements was achieved. In-cylinder measurements at 1000 rpm were performed with three multiplexed beams transmitted through an operating IC engine and a qualitative analysis of the recorded data showed very encouraging results. Normalised transmission ratio appeared to follow the thermodynamic changes inside the chamber, but the necessity of a robust referencing and calibration scheme in order to obtain accurate quantitative data is evident. The importance of a rigid, carefully-designed opto-electronic setup and optical alignment is also evident.

Chapter 7
In-Cylinder Hydro-Carbon Tomographic Measurements

7.1 Introduction

A set of optical tomography tests and reconstructive imaging of Hydro-Carbon (HC) concentration distribution in an IC engine are presented here. The basic theoretical principles for Near-IR HC species absorption spectroscopy are the same as these of H_2O, as given in Chapter 2. As discussed previously [39,40,41] the 1700 nm overtone of the 3.4 μm fundamental vibration C-H stretch has been selected to be probed, along with the absorption-free wavelength at 1650 nm for referencing non-species related attenuation. Near-IR water vapour features discussed in Chapters 2 and 3 are extremely sensitive to temperature and pressure variations. Conveniently though, the 1700 nm HC absorption unstructured feature is a very broad and relatively temperature-insensitive and it is adequate to infer species concentration along a transmission path [95]. Spectral line investigation of iso-octane absorption, presented in that work, showed that the 1700 nm feature is the combination of many HC overtones which form a very wide (>1 nm), relatively flat absorption feature at that wavelength. That means any wavelength oscillation, induced by the amplitude modulation of the diode laser source, does not affect the measurement accuracy when a fixed-wavelength scheme, similar to that used in section 6.2, scheme is used. The Beer-Lambert law from Eq. (2.1) can be re-written as:

$$I_r(\lambda) = I_O(\lambda)\exp\left(-k(\lambda)\int_L x_{abs}\ .dl\right) \tag{7.1}$$

where $I_o(\lambda)$ is the incident light intensity, $I_r(\lambda)$ is the received intensity on the photodetector, $k(\lambda)$ is the wavelength-dependent absorption coefficient of the target species, and dl is the line element. In order to carry out tomographic reconstruction of the concentration distribution x_{abs} the line integral in Eq. (7.1) must be determined, and it is termed the path-concentration integral (PCI); it is obtained from the ratio of transmission of an absorbed wavelength λ_1 to that of a second nearby reference wavelength λ_2 selected to have minimum absorption by the target species and any other species of the gaseous mixture [42], as shown in eq. (7.2):

$$\int_L x_{abs}\ .dl = \frac{1}{k(\lambda_1)-k(\lambda_2)} \quad \ln\left(\frac{I_r(\lambda_2)}{I_r(\lambda_1)}.\frac{I_O(\lambda_1)}{I_O(\lambda_2)}\right) \tag{7.2}$$

The same dual-frequency lock-in technique used for the water vapour system, detailed in previous chapters, is used again to measure simultaneously the intensity of the transmitted beams. In this case however there are only two wavelengths to modulate and thus TDM is no longer necessary. The 1650 and 1700 nm DFB lasers are directly modulated by high frequency DDS outputs at 300 and 500 kHz. The optical mounting requirements around the engine cylinder dictate that only a few tens of distinct PCI measurements can be obtained, although the related optical design issue has recently been subject to systematic analysis by Kranendonk and Sanders [96,97]. The optimisation of image reconstruction of such data has been extensively studied [43,98,99], but inevitably the spatial resolution obtained is much poorer than PLIF.

The measurements reported here have been focused on the reconstructive imaging of both the spray injection and the subsequent fuel/air vapour formation process. For a stoichiometric mixture of air and iso-octane, at about 10 bar pressure in a typical gasoline engine cylinder, a beam of light at 1700 nm passing diametrically through the cylinder will undergo around 5% absorption by HC molecules. All of the optical launch and receive components are in a single plane, eliminating the need for a piston with a large window inserted into it. The CST method above has been demonstrated in a multi-cylinder engine [42]. Using measurements of only the reference wavelength (λ_2), Hindle et al. [100] demonstrated in a laboratory rig the imaging of the distribution of GDI fuel spray droplets. The combined application of these methods to an engine, to image both the fuel spray distribution and the subsequent fuel vapour distribution in the same cycle, is shown here.

7.2 Engine configuration and operating conditions

A Ricardo Hydra, four-stroke, single-cylinder research engine with a cylinder bore of 80 mm, stroke of length 89 mm and a compression ratio of 9:1 was used for the reported work. This direct injection engine was configured to operate in homogeneous, full load operation, stratified part-load operation and controlled auto-ignition (CAI) combustion modes. For the tomographic imaging study in the relatively cold, motored optical engine, an engine operating condition for high levels of internal exhaust gas recirculation (EGR) was implemented to ensure elevated gas temperatures and rapid and complete evaporation of the air-fuel mixture during the latter stages of the compression stroke. As such, high levels of gas residual trapping and gas turbulence were achieved by the use of early exhaust valve closure and late intake valve opening as well as low maximum valve lifts that resulted in short valve

opening periods. The valve timing was such that the engine was run in the so-called four-stroke, negative-valve overlap mode; the exhaust valves closed at 80 degrees of crank angle rotation (ºCA) Before Top Dead Centre (Non-Firing BTDC) on the exhaust stroke and the intake valves opened at 90 ºCA After Top Dead Centre (Non-Firing ATDC).

In this work, the cylinder head was a single-cylinder direct injection type, supplied by the Orbital Engine Corporation. It featured a pent-roof combustion chamber with four valves and a centrally located, air-assisted injector; absolute air pressure 6.5 bar and fuel pressure 8 bar. The valves were actuated via double overhead camshafts with maximum valve lifts of 4 mm. The steady state injector flow rate was measured to be approximately 3.6 mg/ms. To facilitate the development of a homogeneous fuel-air mixture the fuel injection was timed 'early'; nominally at 120 ºCA ATDC (Non-Firing). However, a delay of approximately 1.3 ms occurred between the start of the electrical pulse to the injector and the observation of the start of liquid injection into the chamber, as reported in Leach et al. [101]. The engine was motored on a dynamometer at an engine speed of 1200 rpm. Engine speed, timing of control signals and synchronisation with the tomographic system was achieved using a high resolution rotary encoder coupled to the engine crankshaft and a once per revolution camshaft pickup. In order to increase vaporization of the fuel charge the engine intake air was heated to greater than 70 ºC. The coolant was maintained at a temperature of 90 ºC and the oil lubricant at a temperature of 40 ºC. The testing period typically varied between 1 to 5 minutes.

New engine parts were designed and manufactured to enable the insertion of a so-called optical annulus, sandwiched between the cylinder head and the cylinder block. This section of the cylinder liner was manufactured from fused silica that enables

transmission of near-IR beams through the fuel-air charge. The optical annulus, manufactured to tolerance specification by Gooch and Housego Ltd. (Illminster, Somerset, UK), was 10 mm high and was mounted between the cylinder head and cylinder block as shown in Figure 7.1. To attain satisfactory alignment between the transmission and reception optical elements (discussed in Section 3), it was found necessary to maintain a form tolerance of 50 microns on each of the inner and outer diameters of the optical annulus, and a tolerance of 50 microns on their concentricity. Data from the optical measurement array were recorded for continuous periods of one minute, during which time three evenly spaced bursts of fuel injection were initiated manually by the operator.

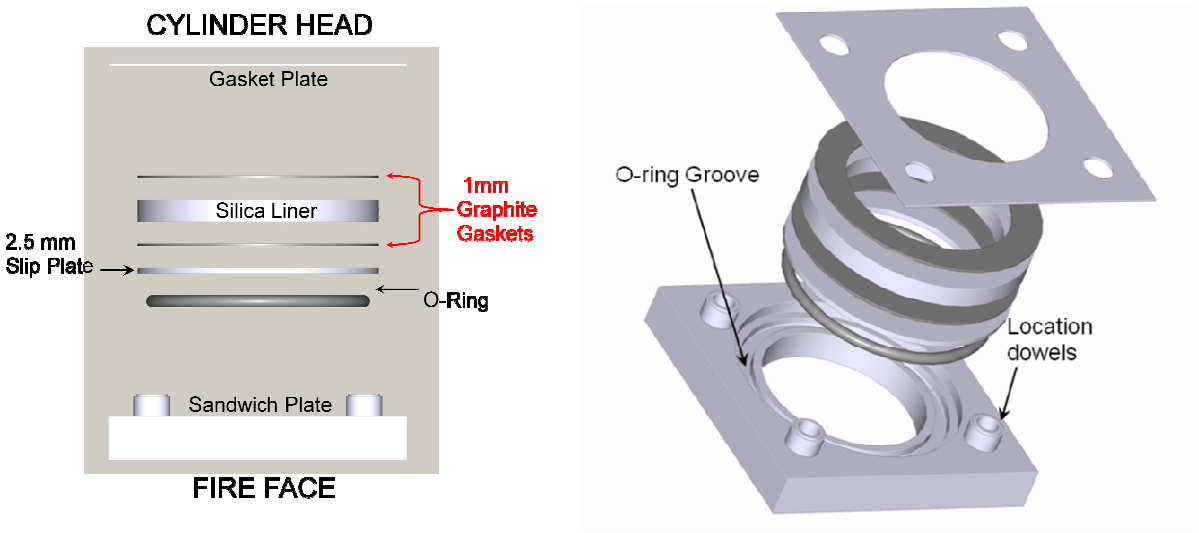

(a) (b)

Figure 7.1 Schematic of the optical liner installation, (a) section view, and (b) perspective view.

7.3 Optical configuration of tomographic system on the engine

The array of 32 Near-IR beams was mounted in a horizontal plane 6 mm below and parallel to the fire-face of the cylinder head, to ensure that the optical path could not be blocked by the low-lift valves that were used. The optical transmission (launch) and receive optics are gradient-index (GRIN) lenses mated up with optical fibres that are connectorised at the opto-electronic interface end and supplied as robust bespoke assemblies (Grintech GmbH, Jena, Germany). Each ferrule containing the lens and fibre end is laid into an accurately machined V-groove in a flat optical plate mounted outside the optical liner and accurately positioned with respect to the liner by the location ring dowels shown in Figure 7.2. To determine the positions of the array of V-grooves, sequential ray tracing was used to calculate the necessary ray paths outside of the cylinder liner such that, following refraction by the liner, a regular array of four projections, each with eight beams, was formed within the cylinder. The V-grooves were CNC-milled into a single plate of aluminium machined to fit around the optical liner during assembly of the cylinder head, as shown in Figure 7.2.

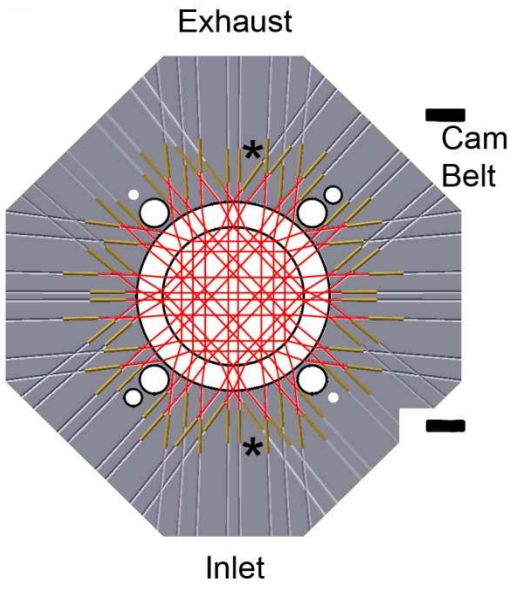

Location of camshaft pulleys and camshaft belt as viewed from engine front

(a)

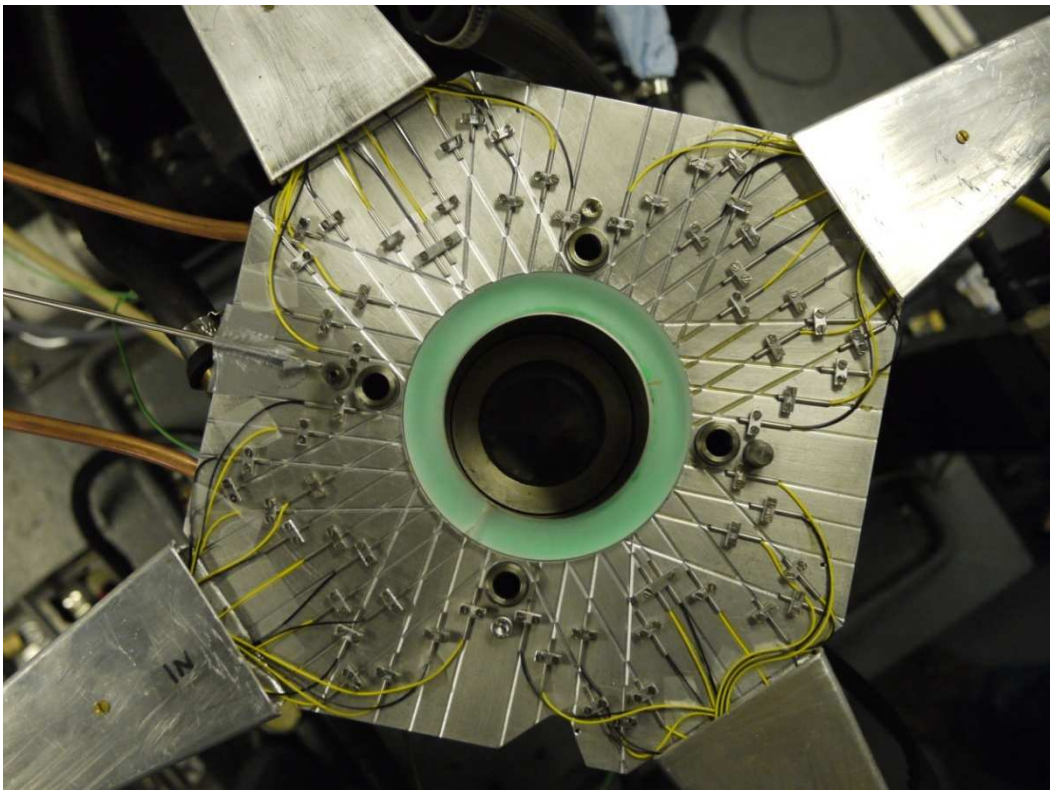

(b)

Figure 7.2 (a) Plan view of 32-beam array mounted on the engine showing grooved plate and beam paths with respect to engine intake and exhaust ports and camshaft layout, (b) actual array used for these experiments with the 64 mounted collimated fibres (yellow SM and Black MMD).

The IMAGER opto-electronic system [42] was used to conduct the experiments, providing light at both the HC-absorbed wavelength and the non-specifically absorbed wavelength to each of the 32 optical launch elements. The IMAGER system is designed to cope with the measurement of HC fuel vapour in the presence of high concentrations of scattering particles, by using fast intensity modulation of the two laser diode sources (300 kHz and 500 kHz), followed by dual-frequency demodulation of the signal from each of the 32 photodiodes. Data were streamed

from the electronic system to hard disk storage at a rate of 10^5 frames per second (fps), synchronously with TTL pulses from the once-per-cycle camshaft encoder.

In Figure 7.3, the results from a typical engine cycle are presented for the two simultaneous tomographic measurement techniques employed as described in [102]; namely the reference wavelength extinction method and the dual-wavelength ratio technique. The plot shows the variation in the received optical intensity at the reference wavelength from a near-diametric beam running between the exhaust and inlet ports in the path of the injected fuel (denoted by * in Figure 7.2 (a)). The figure also indicates the TDC locations, the strokes within the 4-stroke cycle, the period of nominal Inlet Valve Opening (IVO) to Inlet Valve Closing (IVC), the timing of the electrical trigger pulse to the fuel injector, and the types of data analysis performed – single wavelength extinction for the spray period, and dual-wavelength intensity ratio (DWR) for the compression period. Similar to the water vapour experiment described in Section 6.2, the beams are blocked for about 20 ºCA either side the TDC when the top of the piston passes through the plane of the array. Attenuation of the beam by the injected fuel spray can clearly be seen in the optical signal shortly after the fuel injection trigger signal at 120 ºCA ATDC. Note that the electrical delay due to the injector driver and the fuel spray transit time to the measurement location, means that the first observed fuel signal occurs at ~130 ºCA ATDC. For the engine conditions tested at 1200 rpm, liquid fuel injection takes place over approximately 4.2 ms. Fuel evaporation can occur for a further 30 ms up to the ignition angle in the compression stroke. Continued signal attenuation can be seen throughout the intake stroke as the air flow distributes the fuel charge around the cylinder. For the heated intake condition tested, it can be seen in Figure 7.3 that the majority of the liquid fuel has evaporated by approximately 220 ºCA ATDC.

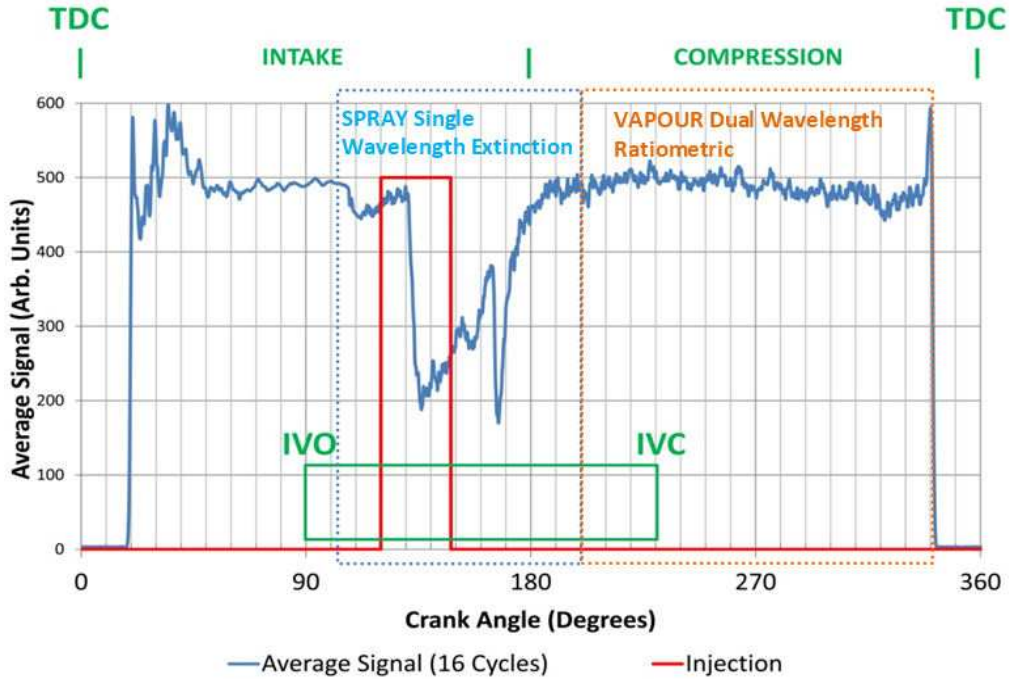

Figure 3:

Figure 7.3 Average recorded signal intensity for 16 fuelled cycles for the selected example beam (reference wavelength) during the intake and compression strokes and engine cycle events.

7.4 Time-series analysis of individual beam data and image reconstruction

In the first step of the analysis, using the crankshaft encoder pulses, similar to the water vapour measurements presented in Chapter 6, the time series data were referenced to crank angle and reshaped from a continuous stream to a series of arrays with each array containing the data from each successive complete 4-stroke engine cycle (720 ºCA). In addition, the data were time-averaged to yield a temporal resolution equivalent to 1 frame per ºCA; at 1200 rpm this corresponds to a sample

rate of 7.2 kHz which is well within the bandwidth limit imposed by the system hardware.

As has been extensively discussed by Wright et al. [41], a number of mechanisms affect the behaviour of the individual beam measurements, in addition to scattering from spray droplets and chemically specific absorption, including malfunction or distortion of the beam optics. In the case of the optical engine however, some of these distorting mechanisms are different. For example, in the multi-cylinder engine the collimated beams are build in the metal engine body and they are subjected in high-pressure variations during the engine cycle. These pressure variations affect both the engine geometry as well as the refractive index of the beam path. In the case of the glass optical liner access though there is hardly any change in the optical path geometry, so the related refractive index distortion in this case should be significantly less. Nevertheless, it is essential to identify and eliminate any beam data that do not behave in a physically sensible manner, but this can be challenging where there is also significant noise or other contributions to rapid data variation. For this purpose, Wavelet Denoising (WD) [103,104] is applied to the 1-D data stream of each individual beam, to enable a robust assessment of the behaviour of the beam data over the whole engine cycle or within one stroke of the engine cycle.

The WD procedure performed by Natasa Terzija is analytically described in [102] and can be described in 3 main steps:

- multi-level decomposition to approximation and detail coefficients using the Discrete Wavelet transform;
- thresholding of the detail coefficients;
- wavelet reconstruction using the Inverse Discrete Wavelet transform.

The complete data pre-processing flow is shown in Figure 7.4. To ensure that any cycle-to-cycle variation in the DC signal level was removed from the optical signals, ($S_{\lambda 1}(t)$, $S_{\lambda 2}(t)$), intra-cycle referencing was carried out by normalising the signal for each cycle to its average value in the period from 200 to 220 ºCA, within each individual cycle. This reference crank angle interval is indicated by θ_{ref}. The choice of θ_{ref} was based on empirical observation of data behaviour, with the above region yielding the most stable signal levels from cycle-to-cycle.

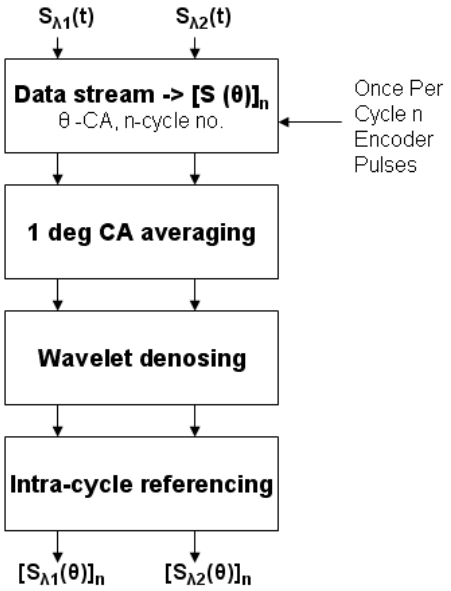

Figure 7.4 Flow diagram for data pre-processing.

Two specific portions of each cycle were analysed using two methods:

- Extinction imaging was used to analyse the fuel spray distribution during injection and throughout the remainder of the intake stroke (100 to 200 ºCA ATDC.) Images were reconstructed using the optical signal received at the reference wavelength ($S_{\lambda 2}$), as in [40].

- To reconstruct images showing the distribution of fuel vapour during the compression stroke (200 to 340 ºCA ATDC) the dual-wavelength ratio (DWR) approach [100] was used to analyse the individual beam data, using the signals at both the measurement ($S_{\lambda 1}$) and reference ($S_{\lambda 2}$) wavelengths, 1700 nm and 1651 nm respectively. An additional cycle-to-cycle referencing scheme was utilised to remove the contribution of non-species specific wavelength-dependent attenuation from the ratiometric signal as is analytically described in [102].

The DWR ratio, R between the fuelled (denoted by R_F) and the unfuelled case (R_{UF}) is dependent upon both non-species-specific and species-specific attenuation of the beam; ideally, the non-species-specific attenuation would be non-wavelength-dependent and non-crank angle-dependent. The crank angle dependence of in-cylinder pressure and temperature is assumed to be identical in both the fuelled and the unfuelled cases. Normalising the signals to a point of low absorption at the intra-cycle referencing stage and assuming zero fuel concentration during unfuelled cycles, ensures that the ratio R_F/R_{UF} is dependent only on the fuel concentration during the fuelled cycles. An example of the ratios R_F and R_{UF} for a near-diametric beam are shown in Figure 7.5 (a). Note the overall trend of both the fuelled and unfuelled ratios due to non-species-specific wavelength-dependent attenuation due to beam steering and deflection as the cylinder pressure increases during compression.

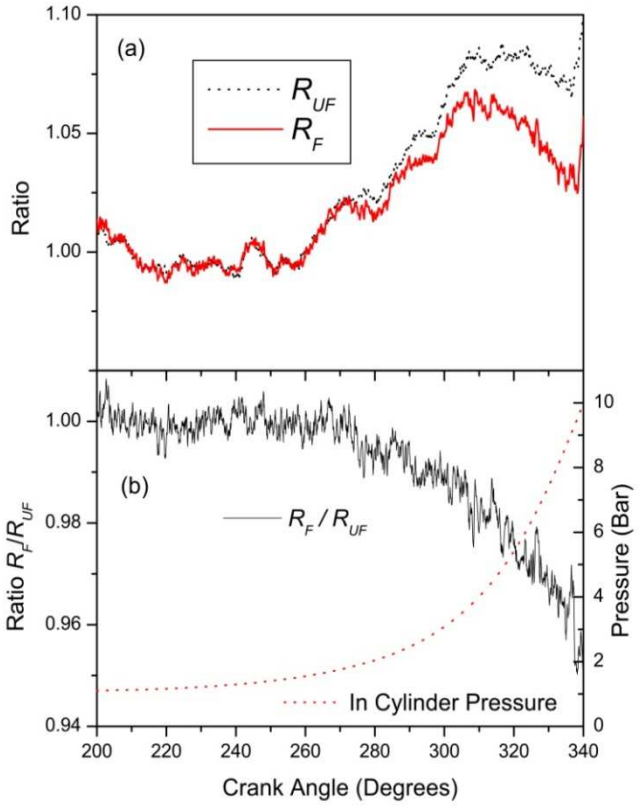

Figure 7.5 DWR signals during the compression stroke, from the beam marked * in Figure 7.2.

Figure 7.5 (b) shows the ratio of the fuelled to the unfuelled data from Figure 7.5 (a). This ratio implies a path-averaged concentration of 0.002 mol.l^{-1} at 320 ºCA. This value is approximately 50% greater than the path-averaged concentration for a beam at the same in-cylinder orientation measured by Wright et al. [42] in a multi-cylinder engine with a stoichiometric mixture of pump grade fuel. This difference is not unexpected, due to the non-firing operation of the engine used in the present work and the negative valve overlap condition that results in increased trapping of residual fuel vapour within the cylinder.

7.5 Image reconstruction

For the data analysis procedure, a qualification test was applied to each of the single-beam data prior to image reconstruction. This qualification test prevents the resulting image being impaired by the inclusion of poor quality data, e.g., those with unacceptably low signal-to-noise ratio (SNR) with more than 5% peak-to-peak noise. For the spray imaging data shown here, 28 out of 32 beams satisfied the qualification test, and for the vapour imaging case 30 beams satisfied it. In order to assess the impact upon the images of the particular missing beams in each case, Figure 7.6 shows the results of simulation with a homogeneous distribution. For all 32 beams, Figure 7.6 (a) shows that the concentration variation within the reconstructed image is only 11%. However, this variation worsens to 22% for the 30-beam case (Figure 7.6 (b)), with the variation running from high concentration on the exhaust side, to low on the intake side. It worsens further to 48% for the 28-beam case (Figure 7.6 (c)), again running in the same direction. However, neither the 30-beam nor the 28-beam case shows any significant distortion in the direction perpendicular to the exhaust-inlet axis, which runs vertically from top to bottom in all the plan view figures in this section. Image reconstruction in such situations is typically reliant upon the availability of some prior knowledge of the form of the subject. The image reconstruction algorithm used here is based on an enhanced iterative Landweber method [99].

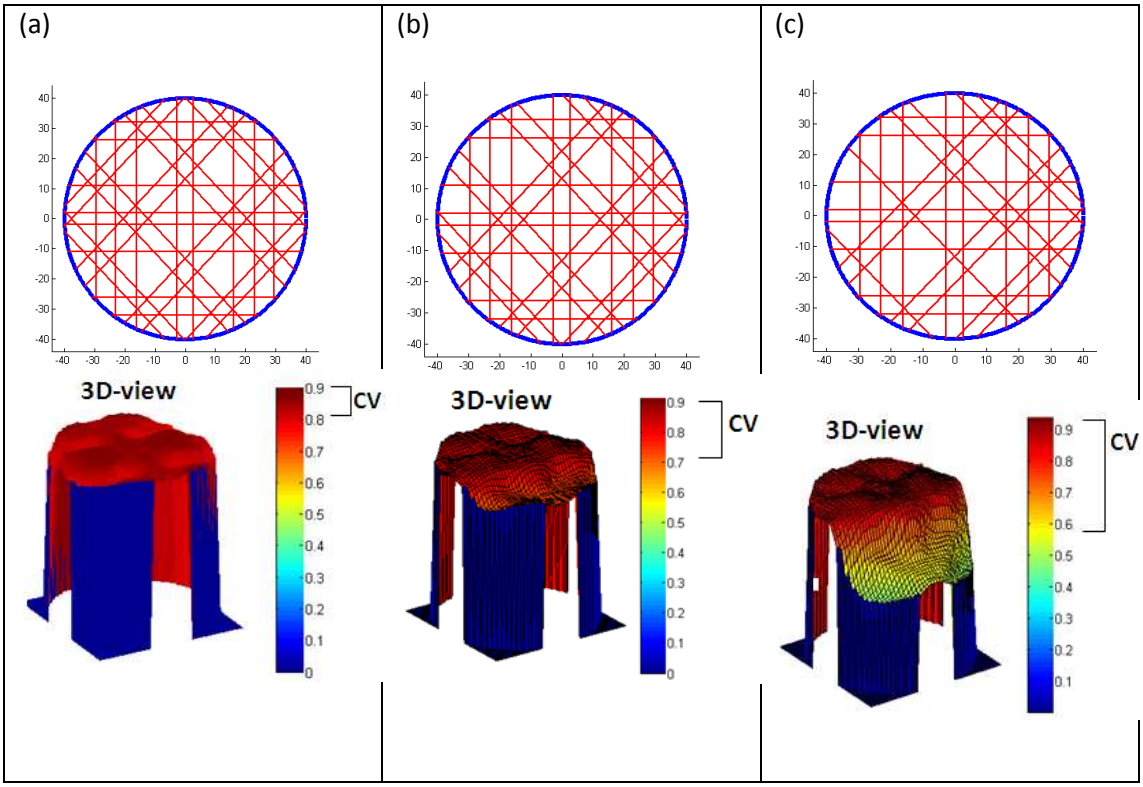

Figure 7.6 Simulation of a homogeneous distribution for: (a) a full 32-beam array where the observed concentration variation (CV) in the reconstructed image was approximately 11%; (b) a 30-beam array where the CV was approximately 22 % and (c) a 28-beam array where CV was approximately 48%.

Figure 7.7 shows reconstructed images from the engine data, both for the injection period (every second cycle, numbered 5, 7, 9 and 11 during a fuelling sequence) and the late compression period (consecutive cycles 9 to 12). The images in Figure 7.7 (a) and (b) show the distribution of the spatial distribution of spray droplets, and then the subsequent distribution of HC fuel vapour. These data are presented here for illustrative purposes and a detailed quantitative analysis of the reconstructed imaging features and dynamics can be found in [102]. This is the first time that the spatial evolution of the fuel charge within a plane of the cylinder has been characterised by tomographic image reconstruction techniques from liquid spray injection in the

intake stroke to vapour behaviour in the late compression stroke during one single cycle and over consecutive cycles of an internal combustion engine.

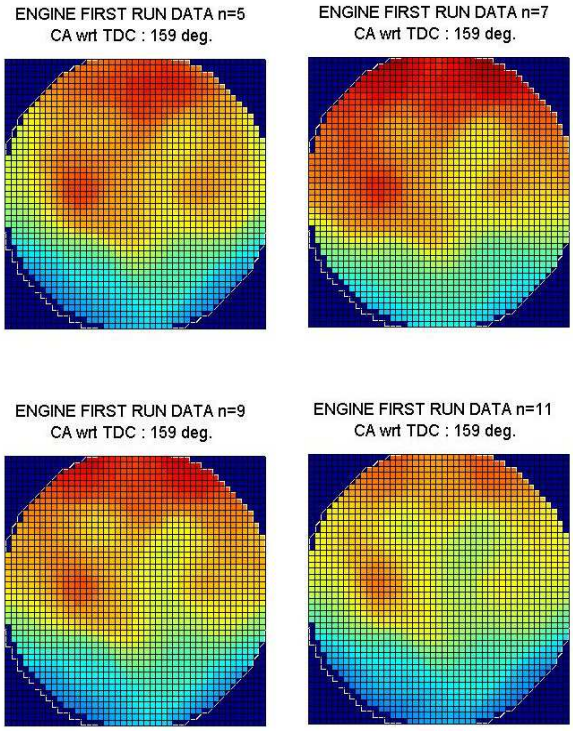

(a) LIQUID FUEL SPRAY IMAGING

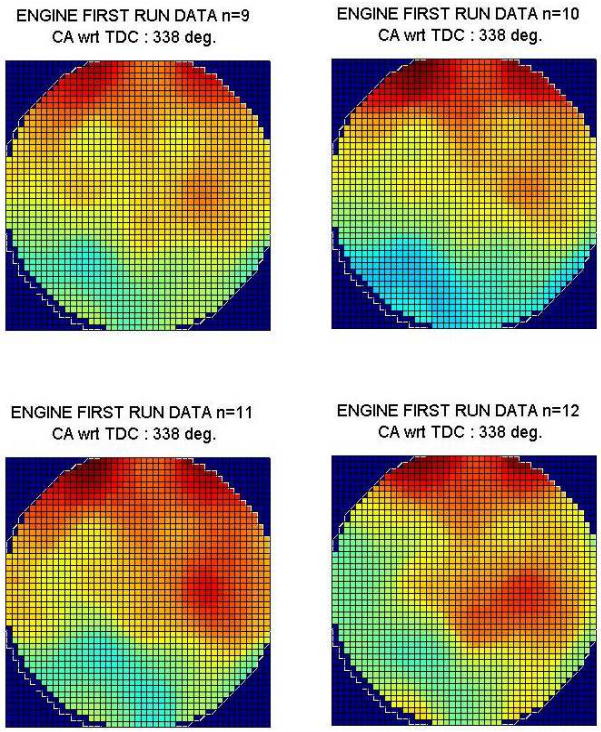

(b) FUEL VAPOUR IMAGING

Figure 7.7 Typical reconstructed distributions in four engine cycles, each cycle numbered (n) within a single fuelling burst sequence, and at given crank angles after exhaust Top Dead Centre (=0 ºCA), (a) liquid fuel spray images at 159 ºCA, from reference wavelength measurements, and (b) fuel vapour images at 338 ºCA, from DWR measurements.

7.6 **Summary**

A series of in-cylinder tomographic HC imaging in an IC, motored-operated engine at 1200 rpm have been presented in this chapter. Optical access and beam alignment facilitated by a novel opto-mechanical scheme with 32 beams mounted on an accurately machined V-grooved array. Sophisticated signal processing algorithms such as Wavelet denoising were used for accurate data analysis and image reconstruction. The spatial distribution of the liquid fuel spray during the intake stroke, was imaged at 6,000 fps by using only the attenuation of the reference wavelength. Dual-Wavelength Ratio data provided fuel vapour images at 2,000 fps in the compression stroke. Various features of these images correspond well with expectation in terms of spray and air flow behaviour, and with PIV and PLIF data in similar engine geometries and operating conditions.

Chapter 8

Conclusions

8.1 Summary and discussion

This thesis has been focused on the design and development of a high-sensitivity absorption spectroscopy scheme for water vapour concentration and temperature measurement. The target application of the new scheme is non-intrusive tomographic imaging of gas distribution in optically accessible IC engines. The sensor has been designed in order to satisfy a number of important requirements such as being non-intrusive to the underline process, to have high temporal and spatial resolution and to be tolerant to non-absorption attenuation and other species interference, especially in extreme thermodynamic conditions and hostile environments. It is also desirable for the sensor to be able to cover a wide dynamic range in terms of species concentration (100-10^5 ppm) and to be applicable in different engine types (i.e. single/multi cylinder). So far, to our knowledge, there is no such a system satisfying all the above criteria. Absorption tomography offers excellent temporal resolution but lacks in terms of spatial resolution compared to other imaging schemes such as PLIF, which in turn is limited to reaction zones and fuel tracers. Thus, we consider a possible combination of these two methods as the ultimate combustion imaging tool.

After the reporting the existing Absorption Spectroscopy schemes in literature, a dual-wavelength ratiometric TDLAS scheme with external intensity-modulation for phase sensitive lock-in detection has been adopted. High-frequency modulation reduces noise susceptibility since the measured signal shifts to higher frequencies where 1/f noise is reduced and subsequent filtering removes thermal and shot noise

with great efficiency. The proposed scheme is taking advantage of recent advances in Near-IR technologies and amongst other components, it utilises commercially available Semiconductor Optical Amplifiers in an innovative way. In this work the SOAs are used for simultaneous amplification, optical switching and intensity modulation, and as it is shown in Chapter 4 in very efficient way. Previously developed optoelectronic and data acquisition instrumentation has been upgraded and modified, and additional components, such as an electronic circuit for regulating the driving signals and a ring-resonator for real time wavelength referencing have also been developed and incorporated into the system. The final system has been extensively tested in the laboratory by measuring atmospheric humidity levels in a controlled environment.

An experimental comparison amongst different signal receiving schemes showed that the frequently used beam capturing method with multimode fibre, suffers from increased etalon effects and modal noise. Collimated multimode fibres are commonly used for signal capturing due to their wide surface area, which facilitates beam alignment, but as it is shown in Chapter 5 they introduce significant signal distortion. Bare singlemode fibres are shown to perform better but due to their small facet area they are inappropriate for alignment-sensitive applications such as engine measurements. Directly capturing the signal with a photo-detector appears to eliminate any etalon effects thus is the best way to improve signal quality and the overall sensitivity of the system. The commercial, general-purpose photo-detectors used for this work are clearly not appropriate for engine tomographic applications mainly due to their size. Nevertheless for future applications, small custom made photodiodes can be designed based on the specific opto-mechanic arrangement.

The system has been also tested in a fixed-wavelength mode where, by using the ratios of two selected features and for known path length and pressure, the temperature can be estimated and then the mole fraction can be inferred. As it has been highlighted during the line selection process, accurate spectroscopic data for the selected transitions are extremely important for reliable measurements. Data extracted from spectral databases such as HITRAN and HITEMP had been found to have inaccuracies especially at extreme thermodynamic conditions. Thus, it is a very critical requirement that the selected absorption lines be validated for the range of temperatures and pressures anticipated for the measurement. The data used for simulating the line-pair selected for this work, at 1350.42 nm and 1385.12 nm, has been validated and corrected by Stanford group.

The calibration approach for finding the baseline signal power before extracting the absolute transmission/absorption signals is also highly critical. The most reliable way to establish this baseline level is by measuring the transmitted power with the absence of the absorber. This is straightforward and can be easily accomplished for several species such Hydrocarbons, but it is more complicated with water vapour since it is always present in the form of atmospheric humidity. Purging with dry gas such as nitrogen is one way of doing this but it has limitations, as there is always a minimum amount of humidity content in dry gases and it can be difficult to implement in certain applications such as engine measurements. In such non-stationary situations where the system resonates due to the engine revolution, additional repetitive noise is introduced into the system and it needs to be accounted for accurate baseline recovery. In the case of fuel measurement this can be achieved either by using data from un-fuelled motored engine operation, or by skipping fuel injection for a few cycles during the same measurement. Another strategy that has

been employed in this work is taking as zero-absorption reference point certain parts of the same cycle where the HC absorber is absent. As previously, this is difficult to achieve for water vapour measurement due to the continuous presence of moisture. One way to get around this would possibly be to pump dry gas into the chamber and supply the injector with dry air as well.

Preliminary tests on an optically accessible IC engine presented here have also shown interesting findings. The multiplexed three-colour signal was split into three beams which projected through the operating engine and were monitored continuously at 150 KS/sec throughout consecutive cycles during motored, fuelled and fired engine operation. A qualitative analysis of the acquired data showed that transmitted beams are susceptible to beamsteering and scattering effects. A non-absorbing reference beam can be used to account for these effects as it is employed in Chapter 6. It is important for this extra wavelength to be as close to the absorbing wavelengths as possible in order to have similar refractive index and to react in these colour–related effects in the same way. Pressure-induced beam steering effects can be also addressed with an appropriate calibration scheme similar to that for the zero line recovery described above.

Fuel concentration-distribution tomography tests in an optical engine for motored and fuelled operation have been also presented. A novel optical access scheme based on a horizontal planar array with 32 collimated beams, mounted on a plate with accurately machined V-grooves, has been implemented. Custom made GRIN rod collimated fibres used for this work proved to be difficult to align and susceptible to vibrations. It appeared the direction of each optical beam was not exactly perpendicular to the lens facet which caused alignment problems within the V-grooves. Also, as it has been shown in Chapter 5 GRIN lens collimated multimode

fibres introduce etalon effects in scanned-wavelength measurements. Data obtained with aspheric lens collimators showed improved quality but are more challenging to implement in tomographic applications due to their bigger size.

Finally, sophisticated post-signal processing techniques such as Wavelet decomposition and thresholding of the detail coefficients proved to be extremely valuable for robust assessment of the recorded data. These algorithms can be used to evaluate the acquired data and reject beams that are not behaving in a physically sensible way. Also, in conjunction with optimised irregular beam arrangements, signal processing algorithms can enhance spatial resolution by maximising the information extracted by limited number of beam projections. The Inverse Discrete Wavelet transform was used for image reconstruction of liquid fuel spray distribution during injection, and fuel vapour during the compression stroke.

8.2 **Future Work**

Clearly, the in-cylinder water vapour distribution measurement system can be further optimised. Firstly a robust optical access setup should be designed for more reliable beam alignment. Minimisation of etalon effects is a critical issue and it should take a lot of consideration. Experimental evaluation showed that anti-reflection coated aspheric lenses, with adjustable focus if possible, perform much better than GRIN rod collimated fibres, and they are the best way to go as they optimise beam collimation and they are less susceptible to vibrations and mechanical noise. Also, more laboratory work in terms of absorption line validation for the predicted in-cylinder thermodynamic conditions (high pressures and temperatures) will facilitate data analysis for engine measurements.

The proposed intensity-modulation, water vapour measurement scheme could be further enhanced with additional colours for more accurate results. It can be also adapted for other chemical species by appropriate selection of wavelengths. Similar high frequency modulation schemes such as WMS are taking advantage of higher order harmonic signals to extract useful information of the absorbed signal and facilitate the calibration process. Thus, investigation of the 2^{nd} harmonic signal behaviour when modulating the optical beams with the SOAs could proved also useful in terms of increasing the measured SNR. Finally, as mentioned earlier a simultaneous implementation of absorption tomography and PLIF measurements could be proved as a great tool for combustion diagnostics.

Appendices

Appendix A Script to Calculate H2O Absorption Spectrum using HITRAN data

```
%  This is performed over a given range in wavelength for a set
temperature and
%  pressure.

%% Constants
h=6.6260755e-34*2.99792458e10/1.38066e-23;  %constant hc/k

%% Input environmental factors

lkj=cputime;

T = 400;         % temperature (K)

P = 2.1325;           % pressure (atm)

xj = 0.03;        % mole fraction H2O

p = xj*P;        % calculate the partial pressure for H20

path = 8;        % path length (cm)

%% Input frequency range and increment over which to evaluate
spectrum

xmin=7218;         % min wavenumber (cm-1)

xmax=7222;         % max wavenumber (cm-1)

ov=2;               % width of region (in wavenumbers) outside above
range over which to evaluate lines

inc=0.01;            % calculation increment

%% Input frequency range and increment over which to calculate each
individual line

k=-10:(inc/2):10;    % range in wavenumbers over which to evaluate
individual lines

%% Look in parsum table to find partition sum Q at temperature T

Par=xlsread('parsum_H2O_161.xls');          %load a truncated HITRAN
database from the file H2O.xls into a Matlab matrix H

g=Par(:,1);

[q0]=find(g==296);
```

```
[qt]=find(g==T);
Q0=Par(q0,:);
QT=Par(qt,:);

Q=((Q0(2))/(QT(2)))*(296/T);                %calculate ratio
Q0/Q(T)*T0/T

%% Load HITRAN data for H2O lines in the range 1-2.2 microns into
the matrix HIT

H=xlsread('H2O_161_2004_StanfordJQRST2007_edit.xls');
%load a truncated HITRAN database from the file H2O.xls into a
Matlab matrix H

x=H(:,1);
[r]=find((x>(xmin-ov))&(x<(xmax+ov)));    %this code reduces the
matrix H to the specified wavelength range by finding all absorption
lines within the given wavelength range
r1=r(1);
r2=r(length(r));

HIT=H(r1:r2,:);                 %The matrix HIT contains HITRAN Data
for the lines in range

%% Print to screen number of lines to be calculated

length(HIT)                     %print no. of lines to be calculated

%% Calculate each individual line store the results in a 3D Matrix

I = zeros(length(k),2,length(HIT));     %initialise the results
matrix

for z=1:length(HIT)

    deltair = HIT(z,8);                 % HITRAN coefficient for air
broadened line pressure shift

    x0 = HIT(z,1)+(P*deltair);          % HITRAN linecenter
frequency

    S = HIT(z,2)*2.4794e19;             % HITRAN linestrength @ 296K
multiplied by factor for conversion from cm-1/(molecule*cm-2) to cm-
2/atm (this conversion factor is only for 296K)

    nair = HIT(z,7);                    % HITRAN coefficient of T
dependence for air broadend half width

    gair = HIT(z,4);                    % HITRAN air broadened HWHM

    gself = HIT(z,5);                   % HITRAN self broadened HWHM
X2 to give the FWHM

    E = HIT(z,6);                       % HITRAN lower state energy

    WG = 2*(sqrt(2*log(2)*1.38066e-
23*6.022e26)/2.99792458e8)*x0*sqrt(T/18.0106);       % calculate
Doppler FWHM
```

```
    glor = 2*((296/T)^nair)*((gair*(P-p))+(gself*p));
% calculate the Lorentzian FWHM

    B=exp(-h*E*((1/T)-(1/296)))*(1-exp(-h*x0/T))/(1-exp((-
h*x0)/296)); %Calculate linestrength ratio exponents for given E, v
and T

    ST=S*Q*B;                                   %Calculate S/So for
given E, T and v

    a=sqrt(log(2))*(glor/WG);                                   %
calculate the Voigt "a" parameter

    amp = path*(2/WG)*(sqrt((log(2))/pi))*(ST*p);               %
calculate the linecentre magnitude

    X =(2*sqrt(log(2))/WG).*k;                                  %
calculate the non-dimensional line positions store them in vector X

    for i=1:length(X)

        L(i) = amp*Voigt(X(i),a);                       % calculate
the lineshape using the function Voigt

    end;

    I(:,:,z) = [(k+x0)',L'];                            % store each
line as a 'sheet' in the 3D matrix I

end


%% Add up contributions I from each line at each wavenumber xcalc

xcalc=(xmin:inc:xmax)'; % define a vector of wavenumbers for which
intensities need to be calculated

for g=1:length(xcalc)   % loop to calculate the total intensity at
each point xcalc by summing contributions from each line at that
point

    for j=1:size(I,3)                               % for each line
(i.e. each 'sheet' j of I) work out the intensity contribution at
xcalc

        Int(j)=Incon(xcalc(g),I(:,:,j),inc);    % calculate
intensity of line j at wavenumber xcalc using the linear
interpolation function Incon place in vector Int

    end

    Absx(g)=[1-(exp(-1*(sum(Int'))))];                          % sum
the intensity contributions from each line at wavenumber xcalc in
the vector Int
```

```
    abs(g,:)=[xcalc(g),Absx(g)];                % store the
absorbance with corresponding wavenumber in the vector abs

end
Absx2= Absx';
%% Plot Calculated Spectrum

plot(xcalc,Absx)
xlabel('Wavenumber (cm-1)')
ylabel('Absorbance')

cputime-lkj,

data = cat(2, xcalc, Absx');
xlswrite('Wavenumber_vs_Absorption.xlsx' , data)
```

Appendix B Script to Simulate the Ring-Resonator Response

```
% Declare simulation wavelength range

v = linspace(1350.41e-9,1350.43e-9,50*100); % (1350.41 - 1350.42 nm)

%Declare variables

neff = 1.45;            % Refractive index
gamma1 = 0.02;          % Excess loss of coupler 1
gamma2 = 0.02;          % Excess loss of coupler 2
a = 0.00005;            % Fibre field loss (0.22 dB/km)
l1 = 0.15;              % Ring length of coupler 1
l2 = 0.15;              % Ring length of coupler 2

for K1 = 0.2:0.2:0.8        % Simulated coupling ratios of coupler 1
    for K2 = 0.2:0.2:0.8    % Simulated coupling ratios of coupler 2
        if K1==K2

% Declare Urquhart equations

E1 = (sqrt(1-K1))*(sqrt(1-gamma1))*exp(-2*a*l1);
E2 = (sqrt(1-K2))*(sqrt(1-gamma2))*exp(-2*a*l2);

E11 = (sqrt(K1))*(sqrt(1 - gamma1))*exp(-2*a*l1);
E22 = (sqrt(K2))*(sqrt(1 - gamma2))*exp(-2*a*l2);

Output = ((E11*E22)^2)/exp(-2*a*(l1 + (2*l2)));

% Calculations

n=1:length(v);
for n = 1:length(v)
    b(n) = (2*pi*neff)/v(n);
    normf(n) = Output/((1-(E1*E2))^2 +
(4*E1*E2*(sin(b(n)*(l1+l2)))^2));
    v2(n) = v(n)*10^9;      % Transformation to nanometers
end
```

```
% Plot and save data

plot(v2,normf)
axis([1350.41,1350.43,0,1])
hold on

        end
    end
end

save 1350nm.txt normf -ascii

xlabel('Wavelength (nm)')
ylabel('Relative Transmission')
plotedit on
grid on
```

Appendix C Wavelength mapping based on Ring-Resonator data

```
% Read Resonator and Measurement Data
Abs_Signal = Matlab_Import_File2(:,1);
Reson_Signal = Matlab_Import_File2(:,2);

% Find and Locate the peaks of the Resonator Signal
[Peaks,Locs] = findpeaks(Reson_Signal);

% Find the index of the Absorption Peak
L = min(Abs_Signal);
L_Index = find(Abs_Signal == L);

% If there are more than 1 minimum points, then calculate the
Average integer
Avg_Index = round(sum(L_Index)/length(L_Index));

% Find the index of the fringe which is nearer to the absorption
peak
d = abs(Avg_Index - Locs(1));
for N=1:length(Peaks);
if ( abs(Avg_Index - Locs(N)) < d )
     d = abs(Avg_Index - Locs(N));
     new_N=N;
end
end

% Set the new Wavelength Scale
Scale_length = length(Peaks);

%Create a new vector with length equal to the wavelength scale
Wave_Scale = zeros(Scale_length,1);

% Centre Wavelength absolute value has been taken from the
theoretical data
% Wavelength step has been calculated by dividing the Wavelength
difference
```

```
% of the two main absorption peaks (1350.42 and 1350.25nm), with the
number
% of fringes between them
Centre_Wave = 13;
Wave_Step = 0.002;
Wave_Scale(new_N) = Centre_Wave;

% Calculate the values of the new wavelength scale
for M = new_N + 1:length(Peaks);
Wave_Scale(M) = Centre_Wave - Wave_Step;
Centre_Wave = Wave_Scale(M);
end
Centre_Wave = 1350.42;

for M = new_N - 1:-1:1;
Wave_Scale(M) = Centre_Wave + Wave_Step;
Centre_Wave = Wave_Scale(M);
end

%Sampling the Absorbed signal to the locations of the resonator
peaks
Sampl_Trans = Abs_Signal(Locs);
Norm_Trans = Sampl_Trans/1;
Norm_Abs_Signal = 1 - Norm_Trans;

plot(Wave_Scale,Norm_Abs_Signal);

% Import data into an array and export them into an excel file
data = cat(2, Wave_Scale , Norm_Abs_Signal);
xlswrite('TestFile.xls', data)
```

Appendix D Separate logged data into single cycles based on the encoder signal

```
function [result] =
funcEnc(Enc,CylPres,MAP,vin,vinref,trigger_value,triggerref_value)
% >> [Ch1result] = funcEnc(Enc,CylPres,MAP,Ch1,Ch1ref,0.250,0.3);

min_frame_length = 17000;
trigger_enc = 0;
searching_windows = 1500;

% looking for start  frame
counter  = 0;
trigger_count = 0;
trigger_lock = 0;
offset = 10;
for i=1:size(Enc,1)
    if Enc(i,1) > trigger_enc
        trigger_count = trigger_count +1;
        if trigger_count == offset && trigger_lock == 0
            counter = counter + 1;
            start_frame(counter,1) = i;
            trigger_lock = 1;
        end
    else
        trigger_count = 0;
        trigger_lock = 0;
```

```
    end
end

% searching by window
for i=1:size(start_frame,1)-1
    temp =start_frame(i,1)-searching_windows;
    if temp < 1 ; temp = 1; end
    for j=temp:start_frame(i+1,1)+searching_windows
        found_boundary = 0;
        if vin(j,1) < trigger_value % finding start frame (outer
boundary)
            start_frame(i,2) = j;
            found_boundary = 1;
            break;
        end
    end
    if found_boundary == 1
        for j=start_frame(i,2):start_frame(i+1,1)+searching_windows
            if vin(j,1) > trigger_value % finding start frame (inner
boundary)
                start_frame(i,4) = j;
                break;
            end
        end
    else
        start_frame(i,4) = -1;
    end
    for j=start_frame(i+1,1)+searching_windows:-1:start_frame(i,1)
        found_boundary = 0;
        if vin(j,1) < trigger_value % finding stop frame (outer
boundary)
            start_frame(i,3) = j;
            found_boundary = 1;
            break;
        end
    end
    if found_boundary == 1
        for j=start_frame(i,3):-1:start_frame(i,1)
            if vin(j,1) > trigger_value % finding stop frame (inner
boundary)
                start_frame(i,5) = j;
                break;
            end
        end
    else
        start_frame(i,5) = -1;
    end
end

% finding base line
accumulate = 0 ;
counter = 0;
for i=1:size(vin,1)
    if vin(i,1) < trigger_value
        accumulate = accumulate + vin(i,1);
        counter = counter + 1;
    end
end
avg_base = accumulate/counter;

accumulate = 0 ;
```

```
counter = 0;
for i=1:size(vinref,1)
    if vinref(i,1) < triggerref_value
        accumulate = accumulate + vin(i,1);
        counter = counter + 1;
    end
end
avg_base_ref = accumulate/counter;

% generating result
counter = 0;
data_id=linspace(0,size(vin,1)-1,size(vin,1))';
for i=1:size(start_frame,1)-1
   if start_frame(i,3) - start_frame(i,2) > min_frame_length
       counter = counter + 1;
       if start_frame(i,4) == -1 || start_frame(i,4) == -1
           disp('Found error at certain frame');
       else
           real_start =
floor((start_frame(i,2)+start_frame(i,4))/2);
           real_stop = ceil((start_frame(i,3)+start_frame(i,5))/2);
           result{counter}(:,2) = vin(real_start:real_stop,1) -
avg_base ;
           result{counter}(:,3) = vinref(real_start:real_stop,1) -
avg_base_ref ;
           result{counter}(:,4) = CylPres(real_start:real_stop,1)
;
           result{counter}(:,5) = MAP(real_start:real_stop,1)
;
           result{counter}(:,1) = Enc(real_start:real_stop,1)
;
            result{counter}(:,6) = data_id(real_start:real_stop,1);

       end
   end
end
```

Appendix E Recorded data post-filtering

```
function [filter_result,h,w] =
low_pass_filter(signal,cutoff_frequency,smoothness)
% [filter_result,h,w] = low_pass_filter(result{1}(:,1),10,500);

w = cutoff_frequency/(2*smoothness); % Normalized frequency
%design a low pass fitler with above mentioned specifications
[b,a]=butter(2,w,'low'); %5th order butterworth LPF
[h,w]=freqz(b,a,1024); %Frequency response of the filter

filter_result = filter(b,a,signal); % pass the input signal through
the filter

filter_result = medfilt2(filter_result, [20 1]); % 1st stage -
Median filter

filter_result = medfilt2(filter_result, [20 1]); % 2nd stage -
Median filter

filshift = filter_result(40:end,1); % Shift filtered signal 80
points back to compensate for the low-pass phase shift
```

```
filshift(numel(filter_result))=0; % Appent zeros at the end of the
shifted vector

filter_result = filshift;

fs=smoothness;
```

Appendix F Separates the TDM signal into the two original wavelengths (1350 nm and 1385 nm)

```
function [result_top, result_bottom, result_mid] =
boundary_tracking(signal,frame_marker,initial_top_level,initial_low_
level)

% [Ch1_1350, Ch1_1385, result_mid] =
boundary_tracking(Ch1Centr(:,1:4),frame_marker,5.2,3.5);

tic;
windows_size = 30;
variance_limit = 0.01;
default_floor_value = 0;
level_criterian = 0.4;

result = nan(size(signal));
result_top = nan(size(signal));
result_bottom = nan(size(signal));
for col=1:size(signal,2)
    if mod(col,20)==0
        disp(['Processing frame ' num2str(col) ' of '
num2str(size(signal,2)) ' ...']);
    end
    look_lock = 0;
    counter = 0;
    for row=1:size(signal,1)-windows_size+1
        sample=signal(row:row+windows_size-1,col);
        mid_sample=floor((row+row+windows_size-1)/2);
        var_sample=var(sample);
        if var_sample <= variance_limit
            result(mid_sample,col) = mean(sample);
            if look_lock == 0
                counter = counter + 1;
                fraction_index{col}(counter,1) = mid_sample;
                look_lock = 1;
            end
        else
            if look_lock == 1
                fraction_index{col}(counter,2) = mid_sample;
                look_lock = 0;
            end
        end
    end
end

for col=1:size(signal,2)
    lastavg_top=initial_top_level;
    lastavg_bottom=initial_low_level;
    for f=1:size(fraction_index{col},1)-1
```

```
        midval =
floor((fraction_index{col}(f,1)+fraction_index{col}(f,2))/2);
        avgval =
mean(result(fraction_index{col}(f,1):fraction_index{col}(f,2)-
1,col));
        if abs(lastavg_top- avgval ) < level_criterian
            result_top(midval,col) = avgval;
            lastavg_top = avgval;
        elseif abs(lastavg_bottom- avgval ) < level_criterian
            result_bottom(midval,col) = avgval;
            lastavg_bottom = avgval;
        end
    end
end

for col=1:size(signal,2)
    start_point = frame_marker{col}.zerorange(1,2);
    stop_point =
frame_marker{col}.zerorange(size(frame_marker{col}.zerorange,1),1);
    mid_range =
frame_marker{col}.zerorange(2:size(frame_marker{col}.zerorange,1)-
1,:);
    for i=1:start_point
        result_top(i,col) = default_floor_value;
        result_bottom(i,col) = default_floor_value;
    end
    for i=stop_point:size(signal,1)
        result_top(i,col) = default_floor_value;
        result_bottom(i,col) = default_floor_value;
    end
    for j=1:size(mid_range,1)
        for i=mid_range(j,1):mid_range(j,2)
            result_top(i,col) = default_floor_value;
            result_bottom(i,col) = default_floor_value;
        end
    end
end

for col=1:size(signal,2)
    if mod(col,20)==0
        disp(['Processing top frame ' num2str(col) ' of '
num2str(size(signal,2)) ' ...']);
    end
    for i=1:size(result_top,1)-1
        if isnan(result_top(i,col)) == 0 &&
isnan(result_top(i+1,col)) == 1
            y1=result_top(i,col); x1=i;
        elseif isnan(result_top(i,col)) == 1 &&
isnan(result_top(i+1,col)) == 0
            y2=result_top(i+1,col); x2=i+1;
            for x3=x1:x2-1
                result_top(x3,col)=cal_interpolate(x1,y1,x2,y2,x3);
            end
        end
    end
end
for col=1:size(signal,2)
    for i=1:size(result_top,1)-1
        if isnan(result_top(i,col)) == 1
            disp('Some error found');
            result_top(i,col)=default_floor_value;
```

```
        end
    end
end

for col=1:size(signal,2)
    if mod(col,20)==0
        disp(['Processing bottom frame ' num2str(col) ' of '
num2str(size(signal,2)) ' ...']);
    end
    for i=1:size(result_bottom,1)-1
        if isnan(result_bottom(i,col)) == 0 &&
isnan(result_bottom(i+1,col)) == 1
            y1=result_bottom(i,col); x1=i;
        elseif isnan(result_bottom(i,col)) == 1 &&
isnan(result_bottom(i+1,col)) == 0
            y2=result_bottom(i+1,col); x2=i+1;
            for x3=x1:x2-1

result_bottom(x3,col)=cal_interpolate(x1,y1,x2,y2,x3);
            end
        end
    end
end
for col=1:size(signal,2) %should not happen
    for i=1:size(result_bottom,1)-1
        if isnan(result_bottom(i,col)) == 1
            disp('Some error found');
            result_bottom(i,col)=default_floor_value;
        end
    end
end
result_mid = (result_bottom+result_top)/2;
toc;


function y3= cal_interpolate(x1,y1,x2,y2,x3)
temp=[x1 1;x2 1]\[y1;y2];
y3=temp(1,1)*x3 + temp(2,1);
```

Appendix G Separate logged data into single cycles based on the injector signal

```
function [result] =
funcInjCh3(Inj,CylPres,Enc,MAP,vin,vinref,trigger_value,triggerref_v
alue)
% >> [Ch3result] =
funcInjCh3(Inj,CylPres,Enc,MAP,Ch3,Ch3ref,0.250,0.3);

min_frame_length = 17000;
trigger_inj = 1.5;
searching_windows =3500;

% looking for start frame
counter  = 0;
trigger_count = 0;
trigger_lock = 0;
offset = 10;
for i=1:size(Inj,1)
    if Inj(i,1) < trigger_inj
```

```
        trigger_count = trigger_count +1;
        if trigger_count == offset && trigger_lock == 0
            counter = counter + 1;
            start_frame(counter,1) = i;
            trigger_lock = 1;
        end
    else
        trigger_count = 0;
        trigger_lock = 0;
    end
end

% searching by window
for i=1:size(start_frame,1)-1
    temp =start_frame(i,1)-searching_windows;
    if temp < 1 ; temp = 1; end
    found_boundary = 0;
    for j=temp:start_frame(i+1,1)+searching_windows
        found_boundary = 0;
        if vin(j,1) < trigger_value % finding start frame (outer
boundary)
            start_frame(i,2) = j;
            found_boundary = 1;
            break;
        end
    end
    if found_boundary == 1
        for j=start_frame(i,2):start_frame(i+1,1)+searching_windows
            if vin(j,1) > trigger_value % finding start frame (inner
boundary)
                start_frame(i,4) = j;
                break;
            end
        end
    else
        start_frame(i,4) = -1;
    end
    found_boundary = 0;
%    for j=start_frame(i+1,1)+searching_windows:-1:start_frame(i,1)
    for j=start_frame(i+1,1):-1:start_frame(i,1)
        found_boundary = 0;
        if vin(j,1) < trigger_value % finding stop frame (outer
boundary)
            start_frame(i,3) = j;
            found_boundary = 1;
            break;
        end
    end
    if found_boundary == 1
        for j=start_frame(i,3):-1:start_frame(i,1)
            if vin(j,1) > trigger_value % finding stop frame (inner
boundary)
                start_frame(i,5) = j;
                break;
            end
        end
    else
        start_frame(i,5) = -1;
    end
end
```

```
% finding base line
accumulate = 0 ;
counter = 0;
for i=1:size(vin,1)
    if vin(i,1) < trigger_value
        accumulate = accumulate + vin(i,1);
        counter = counter + 1;
    end
end
avg_base = accumulate/counter;

accumulate = 0 ;
counter = 0;
for i=1:size(vinref,1)
    if vinref(i,1) < triggerref_value
        accumulate = accumulate + vin(i,1);
        counter = counter + 1;
    end
end
avg_base_ref = accumulate/counter;

% generating result
counter = 0;
data_id=linspace(1,size(vin,1),size(vin,1))';
for i=1:size(start_frame,1)-1
   if start_frame(i,3) - start_frame(i,2) > min_frame_length
       counter = counter + 1;
       if start_frame(i,4) == -1 || start_frame(i,4) == -1
           disp('Found error at certain frame');
       else
           real_start =
floor((start_frame(i,2)+start_frame(i,4))/2);
           real_stop = ceil((start_frame(i,3)+start_frame(i,5))/2);

           result{counter}(:,2) = vin(real_start:real_stop,1) -
avg_base - 0.0305;
           result{counter}(:,3) = vinref(real_start:real_stop,1) -
avg_base_ref +0.033+0.147 ;
           result{counter}(:,6) = Inj(real_start:real_stop,1)
/10;
           result{counter}(:,4) = CylPres(real_start:real_stop,1);
           result{counter}(:,5) = MAP(real_start:real_stop,1);

running_no=linspace(0,size(result{counter},1)-
1,size(result{counter},1))/size(result{counter},1);
           running_no = (running_no -0.5)*720;
           result{counter}(:,1) = running_no;
       end

   end

end
```

References

1 World Energy Outlook 2012: Executive Summary, International Energy Agency Publications, Paris 2012

2 Regulation (EC) No. 715/2007 of the European Parliament and of the Council of 20 June 2007 on type approval of motor vehicles with respect to emissions from light passenger and commercial vehicles (Euro 5 and Euro 6) and on access to vehicle repair and maintenance information.

3 H. Zhao, "Homogeneous Charge Compression Ignition (HCCI) and Controlled Autoignition (CAI) Combustion Engines for Automotive Industry," Woodhead, (2007).

4 A. C. Eckbreth, "Laser diagnostics for combustion temperature and species," Vol. 3. CRC Press, (1996).

5 P. Werle, F. Slemr, K. Maurer, R. Kormann, R. Mücke, B. Jänker, "Near- and mid-infrared laser-optical sensors for gas analysis," Opt. and Las. in Eng., Vol. 37, Iss. 2–3, P. 101-114, (2002).

6 J. Kiefer, P. Ewart, "Laser diagnostics and minor species detection in combustion using resonant four-wave mixing," Prog. in En. and Comb. Sci., Vol. 37, Is. 5, 525-564, (2011).

7 P. A. Martin, "Near-infrared diode laser spectroscopy in chemical process and environmental air monitoring," Chem. Soc. Rev. 31, 201-210 (2002)

8 W. Johnstone, A.J. McGettrick, K. Duffin, A. Cheung, G. Stewart, "Tunable Diode Laser Spectroscopy for Industrial Process Applications: System Characterization in Conventional and New Approaches," Sensors Journal, IEEE , vol.8, no.7, pp.1079,1088, (2008)

9 D. R. Bowling, S. D. Sargent, B. D. Tanner, J. R. Ehleringer, "Tunable diode laser absorption spectroscopy for stable isotope studies of ecosystem–atmosphere CO2 exchange," Agricultural and Forest Meteorology, Vol 118, Is 1–2, (2003).

10 H. I. Schiff, G. I. Mackay, J. Bechara, “The use of tunable diode laser absorption spectroscopy for atmospheric measurements,” Res. on Chem. Interm., Vol. 20, Is. 3-5, pp 525-556 (1994)

11 P. Lundin, E. Krite Svanberg, M. Lewander, L. Cocola, S. Andersson-Engels, J. Jahr, V. Fellman, K. Svanberg, and S. Svanberg, “Non-invasive gas monitoring in newborn infants using diode laser absorption spectroscopy—a case study,” Proc. SPIE 8229, 822903 (2012).

12 L.S. Rothman, I.E. Gordon, A. Barbe, D.C. Benner, P.F. Bernath, M. Birk et al., “The HITRAN 2008 molecular spectroscopic database,” Jour. of Quant. Spectr. and Rad. Tran., 110 pp. 533 572 (2009).

13 R. K. Hanson, J. M. Seitzman, and P. H. Paul, "Planar laser-fluorescence imaging of combustion gases," Appl. Phys. B 50, 441–454 (1990).

14 C. Schulz, V. Sick, “Tracer-LIF diagnostics: quantitative measurement of fuel concentration, temperature and fuel/air ratio in practical combustion systems,” Prog. Energy Combust. Sci., 31 (2005).

15 W. G. Bessler, M. Hofmann, F. Zimmermann, G. Suck, J. Jakobs, S. Nicklitzsch, T. Lee, J. Wolfrum, C. Schulz, “Quantitative in-cylinder NO-LIF imaging in a realistic gasoline engine with spray-guided direct injection,” Proc. of the Comb. Inst., Vol 30, Iss 2, 2667-2674, (2005).

16 M. Richter, R. Collin, J. Nygren, M. Aldén, L. Hildingsson, and B. Johansson, "Studies of the combustion process with simultaneous formaldehyde and OH PLIF in a direct-injected HCCI engine," JSME International Journal Series B 48, no. 4 (2005).

17 A.J. Donkerbroek, A. P. van Vliet, L. M. T. Somers, P. J. M. Frijters, R. J. H. Klein-Douwel, N. J. Dam, W. L. Meerts, and J. J. ter Meulen, "Time-and space-resolved quantitative LIF measurements of formaldehyde in a heavy-duty diesel engine," Combustion and Flame 157, no. 1, 155-166, (2010).

18 T. Kim, and J. B. Ghandhi, "Investigation of light load HCCI combustion using formaldehyde planar laser-induced fluorescence," Proc. of the Comb. Inst. 30, no. 2, 2675-2682, (2005).

19 Sick, Volker. "High speed imaging in fundamental and applied combustion research." Proc. of the Comb. Inst. 34, 3509-3530, (2012).

20 F. Hildenbrand, C. Schulz, J. Wolfrum, F. Keller, and E. Wagner, "Laser diagnostic analysis of NO formation in a direct injection diesel engine with pump-line-nozzle and common rail injection systems," Proc. of the Comb. Inst. 28, no. 1, 1137-1143, (2000).

21 V. Nagali and R.K. Hanson, "Design of a Diode-laser Sensor to Monitor Water Vapor in High-Pressure Combustion Gases," Appl. Opt. 36, 9518-9527 (1997).

22 L.C. Philippe and R.K. Hanson, "Laser Diode Wavelength-Modulation Spectroscopy for Simultaneous Measurement of Temperature, Pressure and Velocity in Shock- Heated Oxygen Flows," Appl. Opt. 32, 6090-6103 (1993).

23 A. Griffiths and A. Houwing, "Diode laser absorption spectroscopy of water vapor in a scramjet combustor," Appl. Opt. **44**, 6653-6659 (2005).

24 J.T.C. Liu, G. Rieker, J. Jeffries, M. Gruber, C. Carter, T. Mathur, and R. Hanson, "Near-infrared diode laser absorption diagnostic for temperature and water vapor in a scramjet combustor," Appl. Opt. 44, 6701-6711 (2005).

25 H. Teichert, T. Fernholz, and V. Ebert, "Simultaneous in situ measurement of CO, H2O, and gas temperatures in a full-sized coal-fired power plant by near-infrared diode lasers," Appl. Optics 42, 2043-2051(2003).

26 S.T. Sanders, J.A. Baldwin, T.P. Jenkins, D.S. Baer, and R.K. Hanson, "Diode-Laser Sensor for Monitoring Multiple Combustion Parameters in Pulse Detonation Engines," Proc. Combust. Inst. 28, 587-593, (2000).

27 D.W. Mattison, S.T. Sanders, J.B. Jeffries, and R.K. Hanson, "Diode-Laser Sensors for Pulse Detonation Engine Applications," AIAA 2002-0471 (2002).

28 M.G. Allen, "Diode laser absorption sensors for gas-dynamic and combustion flows" Meas. Sci. Technol. 9:545 (1998).

29 D. W. Mattison, J. B. Jeffries, R. K. Hanson, R. R. Steeper, S. De Zilwa, J. E. Dec, M. Sjoberg, and W. Hwang, "In-cylinder gas temperature and water concentration measurements in HCCI engines using a multiplexed-wavelength

diode-laser system: Sensor development and initial demonstration," Proc. Combust. Inst. 31, 791-798 (2007).

30 L. A. Kranendonk, J. W. Walewski, T. Kim, and S. T. Sanders, "Wavelength agile sensor applied for HCCI engine measurements," Proc. Comb. Inst. 30, 1619-1627 (2005).

31 J. Reid and D. Labrie, "Second-harmonic detection with tunable diode lasers – comparison of experiment and theory," Appl. Phys. B 26, 203-210 (1981).

32 D. T. Cassidy and J. Reid, "Atmospheric pressure monitoring of trace gases using tunable diode lasers," Appl. Opt. 21, 1185-1190 (1982).

33 G.B. Rieker, H.Li, X. Liu, J.T.C. Liu, J.B. Jeffries, R.K. Hanson, M.G. Allen, S.D. Wehe, P.A. Mulhall, H.S. Kindle, K. Sholes, A. Kakuho, T. Matsuura, and S. Takatani, "Rapid measurements of temperature and H2O concentration in IC engines with a spark plug-mounted diode laser sensor," Proc. Combust. Inst. 31, submitted (2006).

34 J. Vanderover, and M. A. Oehlschlaeger, "A mid-infrared scanned-wavelength laser absorption sensor for carbon monoxide and temperature measurements from 900 to 4000 K," Appl. Phys. B 99, no. 1-2, 353-362, (2010).

35 J. Vanderover, W. Wang, and M. A. Oehlschlaeger, "A carbon monoxide and thermometry sensor based on mid-IR quantum-cascade laser wavelength-modulation absorption spectroscopy," Appl. Phys., B 103, no. 4, 959-966, (2011).

36 X. Chao, J. B. Jeffries, and R. K. Hanson, "Wavelength-modulation-spectroscopy for real-time, in situ NO detection in combustion gases with a 5.2 μm quantum-cascade laser," Appl. Phys., B 106, no. 4, 987-997, (2012).

37 W. Ren, A. Farooq, D. F. Davidson, and R. K. Hanson. "CO concentration and temperature sensor for combustion gases using quantum-cascade laser absorption near 4.7 μm." Applied Physics B 107, no. 3, 849-860, (2012).

38 A. K. Das, M. Uddi, and C. Sung, "Two-line thermometry and H2O measurement for reactive mixtures in rapid compression machine near 7.6 μm," Comb. and Flame, Vol. 159., Is. 12, 3493-3501, (2012).

39 S.J. Carey, H. McCann, F.P. Hindle, K.B. Ozanyan, D.E. Winterbone, E. Clough, “Chemical species tomography by near infra-red absorption,” Chem. Eng. J. 77 (1–2), 111–118 (2000).

40 F.P. Hindle, S.J. Carey, K.B. Ozanyan, D.E. Winterbone, E. Clough, H. McCann, “Measurement of gaseous hydrocarbon distribution by a near-infra-red absorption tomography system,” J. Electron. Imag. 10 (3), 593–600, (2001).

41 P. Wright, C.A. Garcia-Stewart, S.J. Carey, F.P. Hindle, S. Pegrum, S. Colbourne, P. Turner, W. Hurr, T. Litt, S.C. Murray, S.D. Crossley, K.B. Ozanyan, H. McCann, “Toward in-cylinder absorption tomography in a production engine,” Appl. Opt. 44 (31), 6578–6592, (2005).

42 P. Wright, N. Terzija, J. L. Davidson, S. Garcia-Castillo, C. Garcia-Stewart, S. Pegrum, S. Colbourne, P. Turner, S. D. Crossley, T. J. Litt, S. C. Murray, K. B. Ozanyan, and H. McCann, “High-speed chemical species tomography in a multi-cylinder automotive engine,” Chem. Eng. J. 158, 2–10 (2010).

43 N. Terzija, J.L. Davidson, C.A. Garcia-Stewart, P.Wright, K.B. Ozanyan, S. Pegrum, T.J. Litt, H. McCann, “Image optimisation for chemical species tomography with an irregular and sparse beam array,” Meas. Sci. Technol. 19 (2008).

44 X. Liu, X. Zhou, J. B. Jeffries, and R. K. Hanson, “Experimental study of H2O spectroscopic parameters in the near-IR (6940–7440 cm−1) for gas sensing applications at elevated temperature,” J. Quant. Spectrosc. Radiat. Transfer 103, 565–577 (2007)

45 M.P. Arroyo, and R.K. Hanson, “Absorption measurements of water-vapor concentration, temperature, and line-shape parameters using a tunable InGaAsP diode laser,” Appl. Opt. 32, 6104-6116, (1993)

46 J.T.C. Liu, J.B. Jeffries and R.K. Hanson, “Large-modulation-depth 2f spectroscopy with diode lasers for rapid temperature and species measurements in gases with blended and broadened spectra,” Appl. Opt. 43, 6500-6509, (2004)

47 N. Kawahara, E. Tomita, A. Ohtsuki, Y. Aoyagi, “Cycle-resolved residual gas concentration measurement inside a heavy-duty diesel engine using infrared laser absorption,” Proc. Comb. Ins., Vol 33, Issue 2, P. 2903-2910, (2011)

48 X. Liu, “Line-of-sight Absorption of H2O vapor: Gas temperature sensing in uniform and non-uniform flows,” Ph.D. dissertation, Dept. Mechanical Engineering, Stanford Univ., Stanford, CA, (2006).

49 D.W. Mattison, “Development and application of laser-based sensors for harsh combustion environments,” Ph.D. dissertation, Dept. Mechanical Engineering, Stanford Univ., Stanford, CA, (2006)

50 Banwell C.N. and McCash E.M., “Fundamentals of Molecular Spectroscopy: Fourth Edition,” McGraw – Hill, 1994

51 J.M. Hollas, “Basic atomic and molecular spectroscopy, Tutorial chemistry texts: 11,” The Royal Society of Chemistry, 2002.

52 K. Duffin, “Wavelength Modulation Spectroscopy with Tunable Diode Lasers: a Calibration-Free approach to the Recovery of absolute gas absorption line-shapes,” Ph.D. dissertation, Dept. of Electronic and Electrical Engineering, University of Strathclyde, Glasgow, (2007).

53 R. Lemus, Vibrational excitations in H2O in the framework of a local model, J. Mol. Spectrosc. (2004)

54 J. K. Messer and F. C. De Lucia, “The pure rotational spectrum of water vapor - a millimeter, submillimeter, and far infrared analysis,” Int. J. Infrared Millimeter Waves **4** 505-539 (1983)

55 H. Li, “Near-Infrared diode laser absorption spectroscopy with applications to reactive systems and combustion control,” Ph.D. dissertation, Dept. Mechanical Engineering, Stanford Univ., Stanford, CA, (2007).

56 P. Kluczynski and O. Axner, “Theoretical description based on Fourier analysis of wavelength-modulation spectrometry in terms of analytical and background signals,” Appl. Opt. 38, 5803-5815, 1999.

57 S. Schilt, L. Thevenaz, and P. Robert, “Wavelength modulation spectroscopy: combined frequency and intensity laser modulation,” Appl. Opt. 42, 6728-6738, 2003.

58 G. Rieker, J. Jeffries, and R. Hanson, "Calibration-free wavelength-modulation spectroscopy for measurements of gas temperature and concentration in harsh environments," Appl. Opt. 48, 5546-5560 (2009)

59 J. T. C. Liu, J. B. Jeffries, and R. K. Hanson, "Wavelength modulation absorption spectroscopy with 2f detection using multiplexed diode lasers for rapid temperature measurements in gaseous flows," Appl. Phys. B 78**,** 503–511 (2004).

60 X. Zhu and D. T. Cassidy, "Modulation spectroscopy with a semiconductor diode laser by injection-current modulation," J. Opt. Soc. Am. B 14**,** 1945–1950, 1997.

61 D. Bomse, A. Stanton, and J. Silver, "Frequency modulation and wavelength modulation spectroscopies: comparison of experimental methods using a lead-salt diode laser," Appl. Opt. 31, 718-731 (1992)

62 H. Li, G.B. Rieker, X. Liu, J.B. Jeffries, and R.K. Hanson, "Extension of wavelength modulation spectroscopy to large modulation depth for diode laser absorption measurements in high pressure gases," Appl. Opt. 45, 1052-1061, 2006

63 X. Ouyang, and P.L. Varghese, "Line-of-sight absorption measurements of high temperature gases with thermal and concentration boundary layers," Appl. Opt. 28, 3979-3984 (1989)

64 A. D. Griffiths and A. F. P. Houwing, "Diode laser absorption spectroscopy of water vapor in a scramjet combustor," Appl. Opt. **44**, 6653-6659 (2005)

65 X. Zhou, X. Liu, J.B. Jeffries, and R.K. Hanson, "Development of a Sensor for Temperature and Water Vapor Concentration in Combustion Gases using a Single Tunable Diode Laser," Meas. Sci. and Technol. 14, 1459-1468, 2003

66 X. Zhou, X. Liu, J.B. Jeffries, and R.K. Hanson, "Selection of NIR H2O absorption transitions for in-cylinder measurement of temperature in IC engines," Meas. Sci. Technol. **16**, 2437-2445 (2005)

67 S.M. Schoenung and R.K. Hanson, "CO and temperature measurements in a flat flame by laser absorption spectroscopy and probe techniques," Combust. Sci. Technol. 24, 227-137, 1981

68 L. Ma, W. Cai, A. Caswell, T. Kraetschmer, S. Sanders, S. Roy, and J. Gord, "Tomographic imaging of temperature and chemical species based on hyperspectral absorption spectroscopy," Opt. Express 17, 8602-8613 (2009)

69 L. S. Rothman, D. Jacquemart, A. Barbe, D. C. Benner, M. Birk, L. R. Brown, M. R. Carleer, C. Chackerian Jr., K. Chance, L. H. Coudert, V. Dana, V. M. Devi, J. M. Flaud, R. R. Gamache, A. Goldman, J. M. Hartmann, K. W. Jucks, A. G. Maki, J. Y. Mandin, S.T. Massie, J. Orphal, A. Perrin, C. P. Rinsland, M. A. H. Smith, J. Tennyson, R. N. Tolchenov, R. A. Toth, J. Vander Auwera, P. Varanasi, and G. Wagner, "The HITRAN 2004 molecular spectroscopic database," J. Quant. Spectrosc. Radiat. Transfer 96, 139-204, 2005.

70 E. Cheadle, S. Karagiannopoulos, P. Wright, N. Terzija, K. Ozanyan, and H. McCann, “Measurement strategies for in-cylinder water imaging in a homogeneous charge compression ignition engine,” in Proceedings of 6th World Congress on Industrial Process Tomography, pp. 1368–1375. (2010)

71 Hagen C.L. and Sanders S., “Investigation of multi-species (H2O2 and H2O) sensing and thermometry in an HCCI engine by wavelength-agile absorption spectroscopy,” Meas. Sci. Technol. 18, 1992 (2007)

72 S. J. Carey, H. McCann, F. P. Hindle, K. B. Ozanyan, D. E. Winterbone, and E. Clough, "Chemical species tomography by near infra-red absorption," Chem. Eng. J. 77(1-2), 111-118 (2000).

73 Moglimi R. “Curing Comparator Instability with Hysteresis” Analog Dialogue 34-7 (2000)

74 M. J. Connelly, “Semiconductor Optical Amplifiers,” London, U.K. Kluwer, (2002)

75 N. K. Dutta & Q. Wang, “Semiconductor Optical Amplifiers,” World Scientific Publishing Co. Pte. Ltd, ISBN 981-256-397-0, (2006)

76 G.P Agrawal, “Fiber-Optic Communication Systems,” Wiley, ISBN 0-471-21571-6, (2002)

77 Connelly, M., “Semiconductor Optical Amplifiers and Their Applications,” Proceedings lASTED international conference on Optical Communications systems and Networks, Banff, Alberta, Canada, July 1-21,2005.

78 P. Urquhart, “Advances in Optical Amplifiers,” InTech, ISBN 978-953-307-186-2, (2011)

79 W. C. Michie, A. Kelly, I. Armstrong, I. Andonovic, and C. Tombling, “An adjustable gain clamped semiconductor optical amplifier (AGC-SOA),” J. Lightwave Technol. 25, 1466-1473 (2007).

80 Hernández G., “Fabry-Perot Interferometers,” Vol. 3. Cambridge University Press, (1988).

81 Betzler, K. "Fabry-perot interferometer." KB20020122, Universitat Osnabruck, Fachbereich Physik (2002).

82 L. C. Philippe and R. K. Hanson, “Laser diode wavelength—Modulation spectroscopy for simultaneous measurement of temperature, pressure and velocity in shock—Heated oxygen flows,” Appl. Opt., vol. 32, no. 30, pp. 6090–6103, Oct. 1993.

83 J. Mørk, A. Mecozzi, and G. Eisenstein, “The modulation response of a semiconductor laser amplifier,” IEEE J. Sel. Top. Quantum Electron. 5, 851–860 (1999).

84 E. Udvary and T. Berceli, “Linearity and chirp investigations on SOA as an external modulator in SCM systems,” EUMA Special Issue on Microwave Photonics 3, 217–222 (2007).

85 J. L. Wei, X. Y. Yang, R. P. Giddings, and J. M. Tang, “Colourless adaptively modulated optical OFDM transmitters using SOAs as intensity modulators,” Opt. Express 17, 9012 (2009).

86 D. C. Kim, B. S. Choi, H. S. Kim, K. S. Kim, K. H. Yoon, O. K. Kwon, and D. K. Oh, “2.5 Gbps direct modulation of reflective semiconductor optical amplifier for wavelength division multiplexing passive optical network colourless sources,” Jpn. J. Appl. Phys. 48, 120209 (2009).

87 P. Wright, K. B. Ozanyan, S. J. Carey, and H. McCann, “Design of high-performance photodiode receivers for optical tomography,” IEEE Sens. J. 5, 281–288 (2005).

88 Li, G.L.; Yu, P.K.L., "Optical intensity modulators for digital and analog applications," Jour. of Lightwave Technology, Vol.21, No.9, pp. 2010- 2030, (2003)

89 J. L. Wei, A. Hamié, R. P. Giddings, and J. M. Tang “Semiconductor Optical Amplifier-Enabled Intensity Modulation of Adaptively Modulated Optical OFDM Signals in SMF-Based IMDD Systems” Jour. Of Lightwave Technology, Vol. 27, No. 16, (2009)

90 W. Johnstone, A.J. McGettrick, K. Duffin, A. Cheung and G. Stewart, “Tunable Diode Laser Spectroscopy for industrial process applications: System characterisation in conventional and new approaches,” IEEE Sensors Journal, 8, 1079-1087 (2008)

91 P. Urquhart, “Transversely coupled fibre Fabry-Perot resonator: Theory,” Applied Optics, 26, 456-463 (1987)

92 G. C Papen, G. M. Murphy, “Modal noise in multimode fibers under restricted launch conditions,” J. Lightwave Technol. 17 5, 817–822 (1999)

93 R. J Bartula, S. T Sanders, “Estimation of signal noise induced by multimode optical fibers,” Opt. Eng. 47, 035002 (2008)

94 D. C. Parmenter, ‘Spark Ignition and Spark Assisted Controlled-Auto Ignition in a Top Entry Direct-Injection Gasoline Engine,’ PhD thesis, University of Brighton, UK, 2008

95 S.J. Carey, ‘Chemical Species Tomography by Near Infrared Absorption,’ PhD thesis, Department of Electrical Engineering and Electronics, University of Manchester, 2001

96 L. Kranendonk and S. Sanders, "Optical design in beam steering environments with emphasis on laser transmission measurements," Appl. Opt. 44, 6762-6772 (2005).

97 Matthew G. Twynstra and Kyle J. Daun, "Laser-absorption tomography beam arrangement optimization using resolution matrices," Appl. Opt. 51, 7059-7068 (2012)

98 K.J. Daun, “Infrared species limited data tomography through Tikhonov reconstruction,” Jou.l of Quant. Spect. and Rad. Trans., Vol. 111, Is. 1, Jan 2010, Pages 105-115, ISSN 0022-4073

99 N. Terzija and H. McCann, “Wavelet-based image reconstruction for hard-field tomography with severely limited data,” IEEE Sens. 11, 1885–1893 (2011)

100 Hindle, F.P.; Carey, S.J.; Ozanyan, K.B.; Winterbone, D.E.; Clough, E.; McCann, H. “Near infra-red chemical species tomography of sprays of volatile hydrocarbons”, Technisches Messen tm, v 69, n 7-8, Aug. 2002, p 352-7

101 B. Leach, H. Zhao, Y. Li, T. Ma,“ Two-phase fuel distribution measurements in a gasoline direct injection engine with an air-assisted injector using advanced optical diagnostics,” Proc. IMechE vol. 221, no. 6, pp. 663-673, (2007).

102 Cheadle E, Karagiannopoulos S, Terzija N, Wright P, Ozanyan KB and McCann H, “Fuel spray and vapour imaging in a single-cylinder research engine,” Proc. 6th International Symposium on Process Tomography, Cape Town, South Africa, March 2012

103 Donoho, David L., “De-noising by soft-thresholding,” IEEE Transactions on Information Theory, 41 (3), pp. 613-627 (1995).

104 D.L. Donoho, I.M. Johnstone, G. Kerkyacharian, D. Picard, J., “Wavelet Shrinkage: Asymptopia,” Royal Statistical Society B. 57 (1995) 301-337